1-19-2022

Materials and Methodologies for Spectroscopic and Optical Analytical Applications in Cultural Heritage Conservation Science

Lyndsay Nichole Kissell
Portland State University

Recommended Citation

Materials and Methodologies for Spectroscopic and Optical

Analytical Applications in Cultural Heritage Conservation Science

by

Lyndsay Nichole Kissell

A dissertation submitted in partial fulfillment of the
requirements for the degree of

Doctor of Philosophy
in
Chemistry

Dissertation Committee:
Tami L. Clare, Chair
Dean Atkinson
James Pankow
Thomas Schumacher

Portland State University
2022

Abstract

The field of conservation science falls in the intersection of science and art. The work of conservation scientists may include any single subdiscipline of chemistry, though it is most commonly a highly interdisciplinary field taking skills from analytical, organic, and inorganic chemistry, as well as surface and materials science. The aims of conservation scientists are to answer questions about the production and aging of material cultural heritage. Knowing the materials used by an artist can lead to insight about the intentions of the object and knowing how those materials degrade will enable the use of preventative measures to ensure the object can be enjoyed for future generations. All conservation science work aims to inform collections care personnel (e.g., conservators and curators) so that they can implement appropriate care, storage, and display conditions for a given object.

Special considerations must be made when analyzing artwork. Such considerations include leaving an object in the same condition it was in before treatment, and when sampling is necessary, minimizing the sample size to the greatest extent possible. Therefore, an important facet of conservation science work is to ensure techniques are as non-destructive and minimally-invasive as possible.

In this work, two applications to conservation science are presented. The first application aimed to identify red colorants on Japanese woodblock prints by novel sampling and analytical methods. The inception of this project was in partnership with the Portland Art Museum (PAM) and the 2018 exhibition entitled *Suzuki Harunobu and the Culture of Color.* The work herein developed a soft mechanical sampling technique for the acquisition of micrometer-sized colorant particles from the surface of 18th century

woodblock prints. In Chapters 3 and 4, the sampling method is introduced and validated, and the collected samples were analyzed by surface-enhanced Raman spectroscopy (SERS). The analysis was aided by the implementation of a genetic algorithm (GA) which matches the spectral contributions of the samples to identify the components present. In Chapter 5, the results of a study of artworks attributed to Suzuki Harunobu in the PAM's permanent collection are presented. Through a multi-analytical approach, the palette of red colorants in the collection was established. This work provides technical information and historical context to the practice of commercial printmaking in late-18th century Japan.

The second application, presented in Chapter 7, aimed to develop a sensor for the detection of active corrosion products on the surface of metal sculpture. This work provides the preliminary synthesis and characterization of a carbon-quantum dot functionalized polymeric hydrogel (bCQD-hydrogel). The bCQD-hydrogels harness the fluorescence properties of carbon quantum dots by incorporating them into a flexible polymer network. This soft material is then demonstrated to be sensitive to soluble metal ions, the first indicators of active metal corrosion. Finally, preliminary data is presented demonstrating the use of these materials on metal surfaces. These two projects, while seemingly unrelated, represent a breadth of research focus and illustrate the expansive applications of conservation science.

Dedication

To Nicholas and Henry.
I love you.

Acknowledgements

First, I would like to thank my advisor, Dr. Tami Lasseter Clare, for years of patience, guidance, and mentorship. I am lucky to have found a lab that fit me and my interests so well and I will always be grateful for the opportunities I've had as a member of your lab. I came to Portland only knowing that I loved chemistry and that I wanted to do something that was conservation, but science. Under your mentorship, I have gained a breadth of knowledge and skills, and the confidence to recognize just how valuable that is.

To my dissertation committee, thank you for always pushing me to think deeply, providing valuable feedback, and offering suggestions of where my projects can go next. I'd like to thank Dr. Schumacher for providing a starting point for the GA analysis in Chapters 3-5. Dr. Pankow always provided keen observations to our conversations, challenging me to think deeply about the complex chemical equilibria at play in the corrosion process. Dr. Atkinson has never failed to be available when I appear in the door and say, "Can I pick your brain?"

I would like to acknowledge our collaborators in the Pacific Northwest Conservation Science Consortium, especially those from the Portland Art Museum. Dr. Jeannie Kenmotsu and Samantha Springer brought forth the proposal that became a years-long collaboration—giving me the opportunity to do work that I love and develop my skills as a conservation scientist.

I must also acknowledge the work of Trine K. Quady, who joined me in the lab after just one semester of undergraduate studies, and worked tirelessly with me on the Harunobu project. You're a superstar and I look forward to seeing what you accomplish

iv

next. Many other members of the Lasseter Clare lab have passed through in the years I've been here, and I thank each of you for sharing a laugh, a groan of frustration, or a bag of donut holes—whichever was needed in the moment.

To my friends—thank you for always being supportive and loving. To my best friends and lab-moms, Drs. Capri Price and Katy Hosbein, thank you for always being there for support and companionship in a sometimes very lonely journey. To ChemTwitter—especially Drs. Dan Kurtz, Craig Fraser, Zeus de los Santos, Dani Arias-Rotondo, Eric Arndt, and Paul Lummis, and to Cole Carter. You all were a tie to sanity during a dark time for everyone. I am very grateful to have stumbled upon such a supportive group of excellent chemists.

To my parents and siblings who were stunned to find out I was going to do *even more school* but supported me anyway. I've never been the easiest member of the family, but was always given the space I needed to grow into the person I am. Even when that space was *like, really far*.

And finally, to my family—Nicholas and Henry. Nicholas, you packed up and moved cross-country to support my dreams and career and for that I will be forever grateful. Henry, you won't read this for many years (or, who knows, ever? Moms are boring after all), but you supported me unknowingly and unwaveringly. Without your love and support, this dissertation would never have been possible.

Table of Contents

List of Tables

List of Figures

Glossary of Terms and Abbreviations

Ag NPs   silver nanoparticles

AMPS   2-amido-2-propane-1methyl-sulfonic acid

AMPS-co-PAA   hydrogel formulation with AMPS and PAA co-monomers

bCQD   branched polyethyleneimine-functionalized carbon quantum dot

bPEI   branched polyethyleneimine

BTA   1-H benzotriazole

colorants   mixture of chromophore (i.e., dye or pigment) with binder (i.e.,

                animal hide glue)

CPE   constant phase element

CQD   carbon quantum dot

DART-MS   Direct Analysis in Real Time- Mass Spectrometry

dōsa   mixture of animal hide glue and alum; used as sizing for paper

                artwork

dyes   organic chromophores, often derived from plants

Edo   city (now Tokyo); period of Japanese history 1603 to 1868

EIS   electrochemical impedance spectroscopy

FORS   Fiber Optic Reflectance Spectroscopy

FTIR   Fourier Transform Infrared spectroscopy

GA   Genetic Algorithm

hōsho   "document" quality paper; see also- *kōzo*

ICP-OES   Inductively-Coupled Plasma Optical Emission Spectroscopy

IRR	Infrared Reflectography
KMBS	potassium metabisulfite
kōzo	mulberry paper
KPS	potassium persulfate
MBA	N,N'-methylenebisacrylamide
nishiki-e	brocade prints
PAA	(poly acrylic) acid
PAM	Portland Art Museum
PCA	principal component analysis
PDMS	polydimethylsiloxane
pigments	inorganic chromophores, typically acquired from mineral deposits
S/N	signal-to-noise ratio
SERS	Surface-Enhanced Raman Spectroscopy
ukiyo-e	pictures of the floating world, style introduced in 17th century Japan
UV	ultraviolet
XRF	X-Ray Fluorescence spectroscopy
$\boldsymbol{\rho}$	resistivity, reported as ohm·centimeter (Ω·cm)
σ	Conductivity, reported as milliSeimens per cm (mS/cm)

Chapter 1: Introduction and Background

1.1 Conservation Science

The work of a conservation scientist falls into a highly collaborative niche joining the hard sciences (e.g., chemistry, materials science, physics, biology, engineering) with humanities and technical art fields (e.g., conservation, art history, curation, archeology) in order to answer questions about material cultural heritage. This relationship is depicted graphically in Figure 1.1.
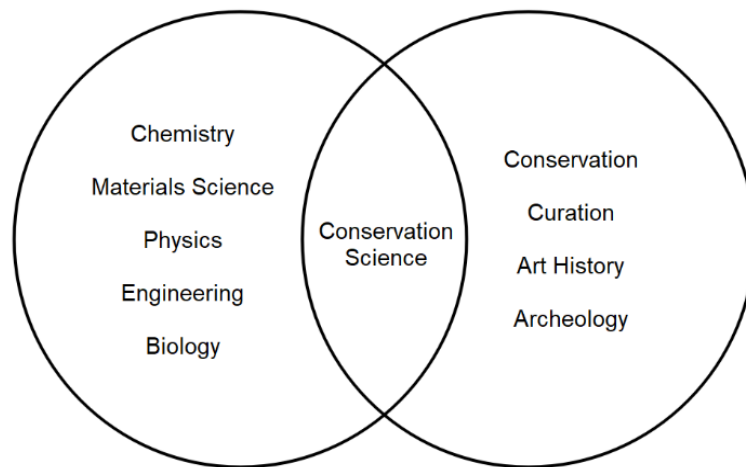
Figure 1.1: Graphical representation of the interdisciplinary nature of conservation science.

The American Institute for Conservation (AIC) has outlined ethical considerations for conservators and conservation scientists.[1] The AIC suggests prioritizing non-destructive and minimally invasive methods and materials for analysis, meaning objects should be left in the same condition in which they were encountered. Therefore, conservation scientists often develop new methods and protocols that allow conservation work and scientific examination to be more informative and less destructive to the object of investigation.

1

1.2 Summary of Presented Work

The work presented in this dissertation shows examples of conservation science work from materials identification and new method development to design of materials for advancing the abilities of the conservation community. Chapter 1 presents the historical context of Japanese woodblock prints. In Chapters 3 through 5, a micro-sampling methodology is introduced which allows for collection of exceptionally small samples from works of art on paper. This sampling methodology was used to collect red colorant samples from the PAM's Harunobu collection. The collected samples were analyzed by SERS, and the data were analyzed by a genetic algorithm spectral fitting method. This work demonstrated a fast, automated method for analysis of spectral data from complex samples that are notoriously difficult to interpret, including mixtures of three or more components.

In Chapter 6, a brief introduction to metal corrosion and sensing is presented. Chapter 7 introduces bCQD-hydrogel materials in which branched polyethyleneimine functionalized CQDs (bCQDs) were incorporated into the polymer matrix of AMPS-co-PAA hydrogels. These materials were developed and characterized for their response to metal ions commonly encountered in the corrosion of metal sculpture. The fluorometric, electrochemical impedance, and colorimetric responses to metal ions were characterized and the materials were tested on solid metal samples.

The work in this dissertation demonstrates the breadth of conservation science as a discipline with examples of method development, materials synthesis, interdisciplinary collaboration, instrumental and computational analyses, and interpretation of results in historical context. The range of analytical and technical methods presented herein also

advance the knowledge and abilities of the conservation community through scientific investigation.

1.3 References

1.   Conservation, A. I. f. Code of Ethics. https://www.culturalheritage.org/about-conservation/code-of-ethics (accessed June 17, 2020).

Chapter 2: Japanese woodblock prints

Figure 2.1: Suzuki Harunobu (Japanese, 1725?-1770), *Hibun (A Secret Missive)*, 1767/1768, color woodblock print with embossing on paper; *chūban nishiki-e*, image/sheet: 10 1/2 in x 7 15/16 in, The Mary Andrews Ladd Collection. Portland Art Museum, Portland, Oregon, 32.78. Image reproduced with permission from the Portland Art Muesum.

Some of the most recognizable Japanese artwork are highly-saturated woodblock prints, such as *The Great Wave off Kanagawa* by Hokusai. However, the tradition of *ukiyo-e ("*pictures of the floating world") predates Hokusai and several of the colorants he used. In fact, *nishiki-e* (brocade) prints in full color were introduced in 1765, around the time of Hokusai's birth. This style of full-color printmaking was ushered in and perfected largely by Suzuki Harunobu—a prolific printmaker and the most well-known early adopter of full-color prints. An example of a print designed by Harunobu is presented in Figure 2.1. Harunobu is best known for producing scenes of everyday life often including excerpts of

poetry or satirizing stories or scenes from common tales[1]. Even today, Edo period prints are immediately recognizable.

2.1 Woodblock Print Production

Though prints are attributed to the artist, woodblock print production was a collaboration coordinated and overseen by a publishing house[2]. The artist (i.e., Harunobu) would conceptualize and design the image, carvers would produce the individual printing woodblocks, and printers would transfer the image from the blocks to paper. These prints were produced on fine *kōzo* (mulberry) paper. The paper was often sized with *dōsa* (a mixture of glue derived from animal hides and alum), a preparative step to prevent spreading of colorants. Dyes (organic) or pigments (inorganic) were mixed with animal hide glue (these mixtures will be referred to herein as colorants) and were applied in thin layers that were adherent to the highly entangled paper fibers.

2.2 The Color Palette

The Edo color palette was extensive, and recent studies have suggested that dyes and pigments from the same color family were often mixed to achieve the desired tone[3]. Red chromophores were reportedly sourced from three inorganic sources (cinnabar, red lead, and ochre) and three organic sources (safflower, sappan, and madder)[4-6]. Despite the commercial nature of print production in the 18th century, the colorants used were not typically recorded. The light sensitivity of organic colorants is well documented[4, 7, 8] and their tendency to fade has influenced the way these pieces are stored and displayed[9]. Accurate identification of the colorants on Japanese prints can inform collections care personnel as to appropriate storage and display practices for these works of art.

2.3 Organic colorant analysis

Common non-invasive and non-destructive colorant analyses, such as imaging, fiber optic reflectance spectroscopy (FORS)[6, 10], and excitation-emission matrix fluorescence analysis (EEM)[11], respond to the interaction of dye molecules with light. Minor changes to the molecular structure of an analyte (i.e., degradation through oxidation or bond cleavage) can result in changes to the color of the compound and light interactions[12-14]. Therefore, these techniques are best carried out with complementary techniques in multi-analytical studies.

Some techniques, such as micro-Fourier transform infrared (FTIR) and micro-Raman spectroscopies and chromatographic techniques (liquid or gas chromatography, usually coupled with mass spectral detection), provide more complete molecular information about the analyte. Chromatographic-mass spectral techniques identify the mass of fragments generated from the analyte, allowing investigators to deduce the mass, and therefore composition, of the complete analyte, but may require a somewhat larger sample. FTIR and Raman micro-spectroscopies use excitation light to probe how individual bonds vibrate in a molecule. The unique combination of bond vibration energies of a given molecule produce a "molecular fingerprint" for that molecule. These methods can be carried out on very small samples, on the order of a few micrometers in diameter.

Raman analysis, however, can be adversely affected by inherent fluorescence of an analyte. To combat fluorescence and increase characteristic Raman signal, surface-enhance Raman spectroscopy (SERS) has been used in the analysis of red organic dyes[15-24]. SERS studies have developed robust instrumental analysis methods; SERS, however, is heavily affected by the type of enhancement substrate (typically a variant of silver or gold

7

nanoparticles), the physical proximity of the dye to the substrate, and the effects of the surrounding sample matrix. Thus, a truly universal method has not yet been disseminated.

2.4 Micro-sampling technologies

Common micro-sampling methods include collection of a single or few fibers, or using a scalpel to collect small cross sections of painted layers. Such methods are exceedingly difficult for analysis of printed papers because the colorants on Japanese prints are applied in very thin layers and are strongly adhered to the paper. Standard sampling methods would render a sample that is large, but with relatively small amounts of colorant and the sampling techniques would likely disrupt the paper matrix, leaving visible damage. Therefore, novel methods for minimally invasive sampling are necessary to acquire samples for analysis.

2.5 References

1.   Thompson, S., The World of Japanese Prints. *Philadelphia Museum of Art Bulletin* **1986,** *82* (349/350), 1-47.
2.   Mihara, S., Ukiyoe. Some Aspects of Japanese Classical Picture Prints. *Monumenta Nipponica* **1943,** *6* (1/2), 245-261.
3.   Wright, J.; Derrick, M.; Adachi, M., The colors of desire: Beauties of the Yoshiwara observed. *Harunobu from the Museum of Fine Arts, Boston. Tokyo: Nikkei* **2017**, 259-63.
4.   Keyes, R. S.; Feller, R. L., *Japanese woodblock prints: a catalogue of the Mary A. Ainsworth Collection*. Allen Memorial Art Museum: 1984.
5.   Takamatsu, T., *On Japanese pigments*. Department of Science in Tokio Daigaku Tokyo: 1878.
6.   Biron, C.; Mounier, A.; Arantegui, J. P.; Bourdon, G. L.; Servant, L.; Chapoulie, R.; Roldán, C.; Almazán, D.; Díez-de-Pinos, N.; Daniel, F., Colours of the « images of the floating world ». non-invasive analyses of Japanese ukiyo-e woodblock prints (18th and 19th centuries) and new contributions to the insight of oriental materials. *Microchem. J.* **2020,** *152*, 104374.
7.   Whitmore, P. M.; Cass, G. R., The ozone fading of traditional Japanese colorants. *Studies in Conservation* **1988,** *33* (1), 29-40.
8.   Whitmore, P. M.; Pan, X.; Bailie, C., Predicting The Fading of Objects: Identification of Fugitive Colorants Through Direct Nondestructive Lightfastness Measurements. *J. Am. Inst. Conserv.* **1999,** *38* (3), 395-409.
9.   Fiske, B. J., Conservation of Japanese Woodblock Prints: Display, Storage and Treatment. *Impressions* **2006,** (28), 60-75.
10.   Fonseca, B.; Schmidt Patterson, C.; Ganio, M.; Maclennan, D.; Trentelman, K., Seeing red: towards an improved protocol for the identification of madder- and cochineal-based pigments by fiber optics reflectance spectroscopy (FORS). *Heritage Sci.* **2019,** *7* (1).
11.   Derrick, M.; Newman, R.; Wright, J., Characterization of Yellow and Red Natural Organic Colorants on Japanese Woodblock Prints by EEM Fluorescence Spectroscopy. *J. Am. Inst. Conserv.* **2017,** *56* (3-4), 171-193.
12.   Ngamwonglumlert, L.; Devahastin, S.; Chiewchan, N.; Raghavan, G. S. V., Color and molecular structure alterations of brazilein extracted from Caesalpinia sappan L. under different pH and heating conditions. *Sci Rep* **2020,** *10* (1), 12386.
13.   Clementi, C.; Nowik, W.; Romani, A.; Cibin, F.; Favaro, G., A spectrometric and chromatographic approach to the study of ageing of madder (Rubia tinctorum L.) dyestuff on wool. *Anal. Chim. Acta* **2007,** *596* (1), 46-54.
14.   Kanehira, T.; Naruse, A.; Fukushima, A.; Saito, K., Decomposition of carthamin in aqueous solutions: influence of temperature, pH, light, buffer systems, external gas phases, metal ions, and certain chemicals. *Zeitschrift f�r Lebensmittel-Untersuchung und -Forschung* **1990,** *190* (4), 299-305.
15.   Amato, F.; Micciche', C.; Cannas, M.; Gelardi, F. M.; Pignataro, B.; Li Vigni, M.; Agnello, S., Ag nanoparticles agargel nanocomposites for SERS detection of cultural heritage interest pigments. *The European Physical Journal Plus* **2018,** *133* (2), 74.

16.   Bruni, S.; Guglielmi, V.; Pozzi, F., Historical organic dyes: a surface-enhanced Raman scattering (SERS) spectral database on Ag Lee–Meisel colloids aggregated by NaClO4. *J. Raman Spectrosc.* **2011,** *42* (6), 1267-1281.

17.   Bruni, S.; Guglielmi, V.; Pozzi, F., Surface-enhanced Raman spectroscopy (SERS) on silver colloids for the identification of ancient textile dyes: Tyrian purple and madder. *J. Raman Spectrosc.* **2009,** *41* (2), 175-180.

18.   Cañamares, M. V.; Garcia-Ramos, J. V.; Domingo, C.; Sanchez-Cortes, S., Surface-enhanced Raman scattering study of the anthraquinone red pigment carminic acid. *Vib. Spectrosc.* **2006,** *40* (2), 161-167.

19.   Cañamares, M. V.; Mieites-Alonso, M. G.; Leona, M., Fourier transform-Raman and surface-enhanced Raman spectroscopy analysis of safflower red-dyed washi paper: pH study and bands assignment. *J. Raman Spectrosc.* **2020,** *51* (6), 903-909.

20.   Greeneltch, N. G.; Davis, A. S.; Valley, N. A.; Casadio, F.; Schatz, G. C.; Van Duyne, R. P.; Shah, N. C., Near-infrared surface-enhanced Raman spectroscopy (NIR-SERS) for the identification of eosin Y: theoretical calculations and evaluation of two different nanoplasmonic substrates. *J Phys Chem A* **2012,** *116* (48), 11863-9.

21.   Kissell, L. N.; Quady, T. K.; Clare, T. L., Optimized micro-sampling and computational analysis for SERS identification of red organic colorants. *Spectrochim. Acta Part A* (Submitted).

22.   Leona, M.; Stenger, J.; Ferloni, E., Application of surface-enhanced Raman scattering techniques to the ultrasensitive identification of natural dyes in works of art. *J. Raman Spectrosc.* **2006,** *37* (10), 981-992.

23.   Lofrumento, C.; Ricci, M.; Platania, E.; Becucci, M.; Castellucci, E., SERS detection of red organic dyes in Ag-agar gel. *J. Raman Spectrosc.* **2013,** *44* (1), 47-54.

24.   Whitney, A. V.; Van Duyne, R. P.; Casadio, F., An innovative surface-enhanced Raman spectroscopy (SERS) method for the identification of six historical red lakes and dyestuffs. *J. Raman Spectrosc.* **2006,** *37* (10), 993-1002.

Chapter 3: Optimized micro-sampling and computational analysis for SERS identification of red organic colorants

This chapter represents a manuscript in preparation with the following authors:

Lyndsay N. Kissell, Trine K. Quady, and Tami L. Clare

Abstract

It is difficult to identify red organic dyes that have similar optical and fluorescence profiles and that may be partially degraded from environmental exposure. Binders, such as hide glue, are used to incorporate dye(s) to make a printable liquid, but their presence adds matrix effects, further complicating identification of the chromophore(s). With Surface-Enhanced Raman Spectroscopy (SERS) it is possible to obtain molecular information from even degraded dyes, though technical hurdles remain for it to be used as a minimally-invasive analytical method for works on printed papers. In this work, a new soft-mechanical sampling method for identifying dyes in thinly printed colorants on paper is described. The method uses an exposure area of about 1 mm^2 to gently contact printed paper and collect micrometer-diameter colorant particles onto a customized polymeric hydrogel surface. Subsequent SERS analysis of red dyes from safflower, sappan, and madder and hide glue mixtures were used to generate a robust spectral reference library. An iterative genetic algorithm (GA) was built and its ability to correctly identify red dyes in a hide glue matrix was tested. Fifty iterative GA runs returned results that matched at least one dye component 96-100% of the time, and matched both dyes in a mixture 58%-100% of the time. Sappan proved to be the most challenging dye to definitively identify by

GA, given that the GA results showed mixtures with another dye and sappan 100% of the time, even when sappan was the sole dye component. Validation that the sampling methodology did not visibly alter test papers was performed by photo documentation under UV and white light and analysis of the paper surface by DART-MS. After validation, the described sampling and analysis methodologies were demonstrated on an 18th century Japanese woodblock print in the collection of the Portland Art Museum, on which, both safflower and madder chromophores were identified. The goals of this study were to develop a robust methodology, sample workup and data analysis procedure useful to analysis of artwork; conclusions and extensions from this work are expected to contribute to the body of knowledge about 18th c. Japanese woodblock prints.

3.1 Introduction

Throughout history, a wide spectrum of organic dyes have been derived from natural sources for painting, printmaking, and textile dyeing. However, many natural organic chromophores fade or color shift with exposure to environmental factors such as heat, light, and moisture and the exact identity of the dye source has not been recorded, leaving collections care personnel uncertain as to the storage, care, and display conditions that are best suited to a given work. For both technical historical reasons and to enable proper collections care, determining the identity of dyes in works of art is important.

An area of interest to the art conservation community is Edo period woodblock prints, specifically those produced as the style transitioned to full color (*nikishi-e*, or, brocade prints).[1-9] These works were produced on *kōzo* (mulberry) paper (known for its fine, long fiber strands) sized with *dōsa* (a mixture of animal hide glue and alum) and printed with colorants that were bound in either rice starch glue or animal hide glue.[10] Of

the possible organic red colorants, it is known that safflower, sappan, and less commonly, madder, were used during Edo period printmaking in Japan[11]. The color-contributing molecules from these colorants are shown in Figure 3.1.
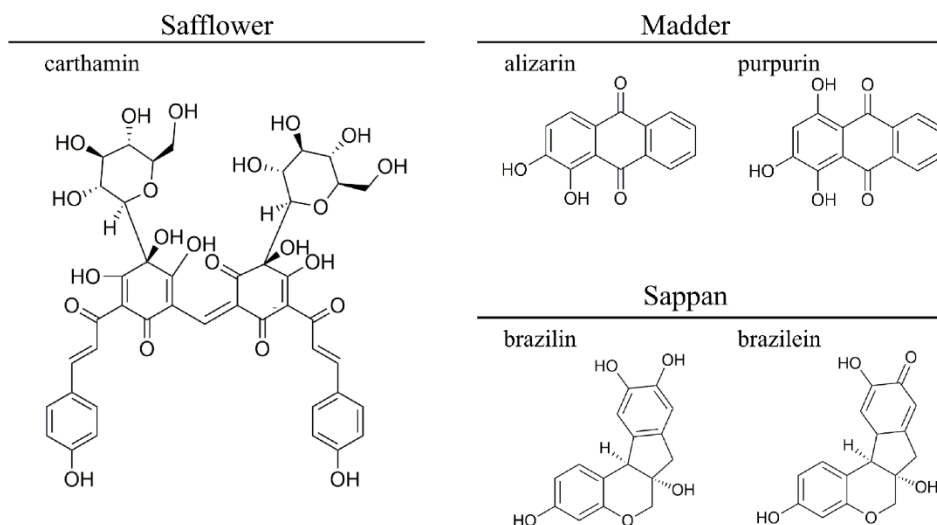
Figure 3.1: Chemical structures of relevant compounds for colorants derived from safflower (carthamin), madder (alizarin, purpurin), and sappan (brazilin, brazilein).

Important ethical considerations for material cultural heritage are that analyses should minimally interact with the work and that sample sizes are minimized, which prioritizes the use of micro-scaled and non- or minimally-invasive analyses[12]. Often, two or more established non-invasive techniques are required for colorant identification. These techniques include ambient x-ray fluorescence spectroscopy (XRF) for identification of some elements[4, 13, 14], excitation-emission matrix (EEM) fluorescence spectroscopy for emission and Stokes shift analysis of fluorescent dyes[2, 4], fiber optic reflectance spectroscopy (FORS)[1, 4, 6, 8], and multiple imaging techniques[5, 8, 15]. XRF is most sensitive to elements heavier than aluminum, and therefore not informative to the identity of organic dyes. EEM, FORS, and imaging methods are more useful when the analyte molecule is

13

intact—once degradation has occurred, the molecule's color-absorbing properties are likely to have changed and these analyses may become less meaningful. Minimally-invasive techniques such as Raman and FTIR micro-spectroscopies provide molecular information on both intact and degraded products by detecting molecular vibrational signatures. Because of these advantages, vibrational spectroscopies have been employed in the analysis of many red dyes from several chemical classes, including chalcones (safflower)[16, 17], neoflavoids (sappan/Brazilwood, Dragon's Blood)[16, 18-21], and anthraquinones (madder, Cochineal, Lac dye)[16, 21-31], as well as collagen[32, 33], the primary protein component of hide glue binders.

Surface-Enhanced Raman Spectroscopy (SERS) offers an advantage over regular Raman through both chemical complexation and electromagnetic means. Metallic nanoparticles (the SERS substrate), suppress the spectrally interfering fluorescent state of dyes by forming a charge-transfer coordination complex between the SERS substrate and the adsorbed dye molecule. With complexation, the origin of Raman scattering occurs from physical proximity of the dye to the surface plasmon (electromagnetic component) [34, 35]. The exact nature of the charge-transfer complex between dye and SERS substrate leads to a difference in the relative spectral contributions of each dye. The reliance on proximity to the metallic surface and the variety of analyte orientations and adsorptions to the SER substrate make it conceivable that replicate SERS measurements of a single sample may result in varying spectra. Adding further spectral complexity are mixtures of dye molecules and other components, such as binder.

SERS studies of artworks typically require the removal of small samples for analysis, such as paint fragments or loose fibers[21, 24, 26, 28, 36]. The samples are usually also

treated with an acid, such as hydrofluoric acid, before analysis, to release the free dye from the matrix. Previous studies have used agar[22, 37, 38] or polymer gels[9] to solubilize colorants. Drawbacks from those studies include their use of a non-aqueous solvent, the direct incorporation of the SERS substrate into the sample, and relatively large contact areas, adding risk of large inadvertent damage to the artwork.

Chemometrics, such as neural networks, principal component analysis (PCA) and genetic algorithms (GA), have been used in the analysis of Raman spectroscopic data[39-45]. Use of chemometric methods have allowed investigators to conduct objective analysis of analytes in complex mixtures and draw conclusions from mixtures that present complex, low signal, or noisy spectra. Such methods have grown in efficiency and popularity with many applications, which include food science[39, 40], forensics[41, 42], and diagnostics[43, 44]. Use of chemometrics to identify dyes via SERS has been established[39, 40, 45], though usage in cultural heritage applications is sparse.[46] Genetic algorithms present two key advantages over other chemometric methods: 1) the programming of a GA is relatively simple and approachable for those not familiar with computational methods and 2) in contrast with clustering methods, genetic algorithms can be designed to provide a tangible output, such as building a complete "solution" (i.e., a spectrum) to compare to the unknown sample.

In this work, a novel minimally-invasive micro-sampling method is described with analysis by SERS. The sample collection method is the first to use a *mechanical micro-sampling* apparatus composed of a customized polymeric hydrogel that gently removes micrometer-diameter samples of colorants from printed papers within its 1 mm^2 collection area. The short-term effects of the sampling process are optically evaluated, and a mass spectral investigation of possible long-term effects is presented. Finally, SERS spectra are

interpreted by fitting micro-sample spectra using a GA loaded with a robust library of SERS spectra from relevant reference materials that were collected in-house. The presented work describes the sampling and GA methodologies, along with a validation of the algorithm's solutions by sampling from mock-up prints made using known dyes. Additionally, we provide a demonstration of its use on three color fields of an 18th c. Japanese woodblock print attributed to Suzuki Harunobu from the collection of the Portland Art Museum, as well as a comparison to data collected from traditional fiber-sampling methods.

3.2 Materials and Methods

3.2.1 Materials

Glycerol, polyacrylic acid (PAA), 2-acrylamido-2-methyl-1-propanesulfonic acid (AMPS, sodium salt, 50% w/v), and N,N'-methylenebis(acrylamide) (MBA) were purchased from Millipore-Sigma (St. Louis, MO). Potassium persulfate (KPS) and potassium metabisulfite (KMBS) were purchased from Thermo-Fisher (Waltham, MA). Potassium carbonate was purchased from Merck (Darmstadt, Germany). Dow SYLGARD™ 184 Silicone Encapsulant (PDMS) was purchased from Ellsworth Adhesives (Germantown, WI). All chemicals were ACS grade and used as received. *Kōzo* paper was purchased from Hiromi Paper Company (Culver City, CA); the selected paper was prepared in the traditional manner, without chemical bleaching agents. All aqueous solutions were prepared using water filtered through an ion-exchange column (measured resistance greater than 18 MΩ).

3.2.2 Methods

3.2.2.1 Silver Nanoparticles, Colorants and Glue Preparations

Silver nanoparticle (AgNPs) synthesis was optimized and characterized, with the complete data reported elsewhere[3]. Briefly, silver nitrate solution was prepared to a concentration of 1.00×10^{-4} M. A solution of hydroxylamine hydrochloride was prepared to a concentration of 1.497×10^{-4} M in 3.33×10^{-4} M sodium hydroxide. All solutions were prepared immediately before synthesis. To synthesize nanoparticles, 90 mL of the hydroxylamine solution and 10 mL of sparged with N_2 separately in sealed flasks. The two solutions were then mixed under N_2 sparging, with the $AgNO_3$ being added to the hydroxylamine solution *via* syringe. After mixing, the solutions were allowed to react for 5 minutes. Aliquots of 1 mL were then centrifuged at 5000 rpm for 5 minutes at 4 °C in an Eppendorf 5430R centrifuge with FA-45-30-11 rotor. After centrifugation, 950 µL of supernatant were removed and 50 µL of fresh deionized water was added to the remaining pellet. Concentrated AgNP solutions were stored in the dark at 4 °C.

Hide glue and colorant standards were prepared according to methods published elsewhere[3]. The solid colorants were stored at RT in foil-covered vials, and the hide glue was stored at 4 °C in a foil-covered vial.

3.2.2.2 Hydrogel synthesis

AMPS-co-PAA hydrogels were synthesized according to previously published methods.[47] To enhance the strength of the gel network, the proportion of crosslinker, MBA, was increased. The final ratio (% w/v) of components was: 18.3% AMPS, 11.2% PAA, 8.1% glycerol, 0.3 % MBA, and 0.02% each KPS and KMBS. After polymerization in molds,

hydrogels were removed and were equilibrated in deionized water to remove excess unpolymerized reagents. Gels were then equilibrated in fresh deionized water before use.

3.2.2.3 Reference print preparation

To produce colorants, the hide glue standard and solid dye(s) were combined via mulling on a glass plate. Deionized water was added dropwise to produce the desired viscosity. The colorants were then painted onto *kōzo* paper.

3.2.2.4 Sampling Methods

Figure 3.2 shows the schematic of the sampling apparatus and workflow. The micro-sampling apparatus was designed to be easily handled while minimizing exposure
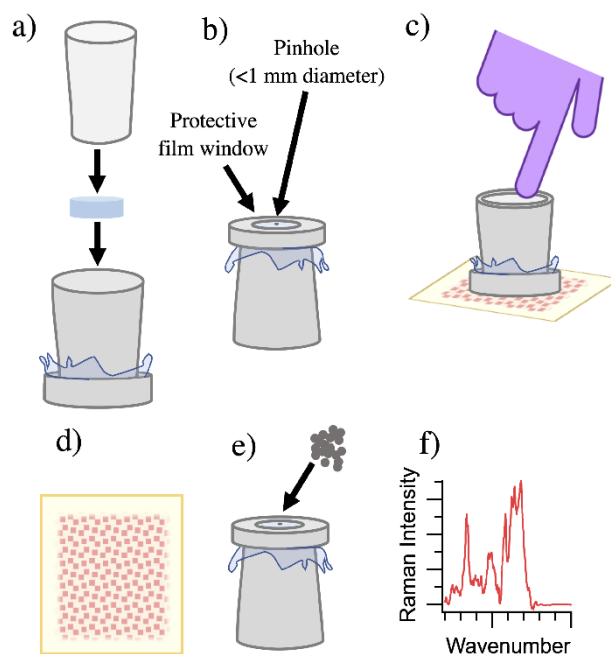
Figure 3.2: Schematic of micro-sampling procedure. *(a)* A 1 cm diameter hydrogel is equilibrated in the environment for 60 minutes, placed in the sample cup and sealed with a PDMS stopper. *(b)* Fully assembled micro-sampler (displayed with bottom up) has a 1 cm diameter protective film window with a <1 mm^2 pinhole for exposure. *(c)* The assembly is placed for 60 seconds with finger pressure to ensure contact of the pinhole-exposed area and the print. *(d)* The print shows no visible changes after 60 second dwell time. *(e)* Ag NP colloid is dropcast over the pinhole to induce SERS effect. *(f)* SER spectra are collected directly from the micro-sampler.

of the objects being sampled. To achieve this, a plastic sample cup, comprised of three pieces was used for the body. A 3 × 3 cm piece of plastic film was placed over the narrow end of the cup and the ring placed to hold the film firmly. A small hole (area ~1 mm^2) was made in the film using a flame-heated needle. Finally, a circular piece of hydrogel (1 cm diameter) was cut and allowed to equilibrate in the environment. After equilibration, excess moisture was wicked away using a KimWipe and the gel was placed inside the cup, against the film. The system was enclosed using a stopper made of PDMS that was cast to the shape of the cup to ensure a sealed system. The final sampling area was limited to the region of hydrogel exposed by the small hole in the film.

Microscopic amounts of pigment were removed from the sample papers using the micro-sampling apparatus. The 1 mm^2 hole was centered over the area to be sampled and light pressure was applied by hand during exposure to sample papers. After the allotted sampling time, as described in section 3.2.1, the apparatus was carefully removed by lifting vertically and placed inverted in a covered container with ample headspace to ensure no contact to the gel surface.

3.2.3 Historical Woodblock Prints

Ono no Komachi, from the series Fūryū rokkasen (The Fashionable Six Poetic Immortals is a woodblock print attributed to Suzuki Harunobu, belonging to the Mary Andrews Ladd Collection at the Portland Art Museum (Accession number 32.75; dating to *ca.* 1768). Hereafter, this work will be referenced as PAM.32.75.

Ishiyama no shūgetsu (Autumn Moon at Ishiyama), from an untitled series of Ōmi hakkei (Eight Views of Ōmi) is a woodblock print attributed to Suzuki Harunobu, belonging

to the Mary Andrews Ladd Collection at the Portland Art Museum (Object 32.83; dating to ca. 1768/1769). Hereafter, this work will be referenced as PAM.32.83.

3.2.4 Instrumental and Processing Methods

3.2.4.1 Imaging

Images of the reference *kōzo* sample papers were collected with a Canon 7dmkII modified for IR Imaging, an EF 50mm F/2.5 lens, MaxMax XNiteCC1 and Kodak Wratten 2E filters, VioStorm WildFire VS-60 lights, and GoldenThread OLT 0.50x and UV Innovations Target UV and UV Gray cards for color balancing. RAW Images were processed using CaptueOne software (v10.2.1).

3.2.4.2 Raman and SERS

Raman spectroscopy was performed on a Horiba LabRam HR Evolution (Kyoto, Japan) equipped with 100×100 cm motorized stage and motorized z-axis control, 633 nm Laser Melles Griot (CVI, Albuquerque, New Mexico), and 600 lines/mm grating. A 50× objective and 300 µm confocal hole were used. Laser power did not exceed 10 mW at the objective. Spectra were collected using LabSpec6 software. Other instrumental parameters were optimized on a case-by-case basis. Spectra were collected from 400-2000 cm^{-1} with an acquisition of 5 to 15 seconds and 10-60 accumulations. The ND filter was varied from 0.1 to 100% power depending on the live-feed Raman intensity. Multiple spectra were collected for each sample area (3-5 spectra per sample). For traditional SERS application to a single fiber, AgNPs were drop cast directly onto the fiber.

3.2.4.3 Direct Analysis in Real Time- Mass Spectrometry

Direct Analysis in Real Time- Mass Spectrometry (DART-MS) was conducted using a Q Exactive LCMS (Thermo Scientific, Waltham, MA) with Orbitrap detector and an IonSense DART module, with the full methodology and raw data described and provided elsewhere[3]. KMD plots were generated using glucose as the base unit from the substrate cellulose; after calculating the Kendrick mass defects, peaks that were present in the background spectrum were removed from the sample KMD plots as well as those peaks that were less than 1% relative abundance.

3.2.5 Computational

Computational methods were executed using IGOR Pro Software v8.04 (Wavemetrics, Lake Oswego, OR).

3.2.5.1 AutoAdaptive baseline algorithm

Recently, a published AutoAdaptive BLS (AABLS) method was reported to sufficiently remove baseline in spectra with poorly resolved peaks.[48] This method was used instead of the native LabSpec software (which uses linear or polynomial baseline correction only) for correcting the SERS spectra. The baseline correction method was adapted for use in IGOR Pro software and, for the data presented, Savistsky-Golay filter spans were set to $L_n = 21$ and $L_b = 5$. The baseline estimation was optimized over 50 iterations to produce a final baseline for subtraction. Evaluation of the baseline correction was performed by analyzing the accuracy on a simulated spectrum (Equation 3.5, Appendix A). The quality of the generated baseline was evaluated by the RMSE and compared to literature methods.

3.2.5.2 Genetic Algorithm

The theory and parameters of genetic algorithms have been described in the literature.[49] In this application to spectroscopic data, the gene is an intensity scaling factor for a single reference spectrum, a chromosome is a complete series of scale factors to apply to the entire reference set, and the individual is the fit spectrum generated by linear combination of the scaled reference spectra. The population size is 500 individuals, with a steady-state replacement style (i.e., n chromosomes of the previous population are deleted and replaced with n new chromosomes) and 10% ranked selection rate. The individuals were varied through random crossover and mutations, each occurring in 50% of new chromosomes. The termination parameters were set to terminate when the top two members of the generation have a fitness difference of less than 0.001, or when 250 generations have been executed.

Standard spectra were collected for cow hide glue and lab-extracted colorants (safflower, sappan, and madder); the colorants were measured as solids, in aqueous solution, and in colorant preparations with hide glue. In this work, the GA used the reference set of 54 standard spectra to build a fit spectrum for a given sample. In a population of 500 solutions, the fitness of a single member was calculated as

Equation 3.1 $$Fig. of\ Merit = \sum_{n=0}^{N}(s(n) - f(n))^2$$

where N is the number of data points in the spectrum, $s(n)$ is the intensity of the sample at point n, and $f(n)$ is the intensity of the fit at point n. Once the fitness threshold was reached, the top member of the population was evaluated and the correlation (R) between it and the sample was calculated (where -1 is exact opposite correlation, 0 is no correlation, and +1 is perfect correlation).

From the best fit, a total contribution of each component was estimated from the contribution of each standard spectrum compared to the maximum possible contribution of that standard. The individual correlation between a standard, y, and the sample, x, (R_y^x) and a measure of the hide glue contribution to the individual standard (GF_y) were determined. From these values, a spectral contribution of standard spectrum y to the fit of spectrum x (SC_y^x) was calculated.

Equation 3.2 $$SC_y^x = R_y^x \times SF_y \times GF_y$$

The total spectral contribution (SC_{total}) was determined by

Equation 3.3 $$SC_{total} = \sum SC_{y1} + SC_{y2} + \cdots SC_{yn}$$

where $SC_{y1\ldots n}$ are the calculated spectral contributions from each standard of a single component (e.g., safflower); if the correlation of a standard to the sample was negative, the standard was automatically excluded from the generated fits.

Finally, the percent spectral contribution of each colorant component is calculated as a percentage of the total contributions.

Equation 3.4 $$\% \, contribution = \frac{SC_{total}^{component}}{\sum SC_{total}^{hide \, glue} + SC_{total}^{safflower} + SC_{total}^{sappan} + SC_{total}^{madder}}$$

where the numerator is the total contribution of the single component of interest. This percentage was used as the final metric of colorant contribution; it was determined that a minimum threshold of 15% must be met for a colorant to be identified definitively. It is important to note that the percent contribution produced by the GA does not correlate with actual mass percentages of the different colorant components (e.g. glue and dyes) due to the variability of SERS enhancement and other matrix effects, though qualitative correlations may be possible.

23

3.3 Results and Discussion

3.3.1 Sample collection and effects on paper

Careful evaluation to ensure that the micro-sampling technique did not alter the prints was an essential step in establishing the viability of this technique for use on artwork.

3.3.1.1 Sampling optimization and particle measurements

The micro-sampling device was tested under museum conditions (21°C, 50% RH) on-site at the Portland Art Museum. Collection parameters were optimized to determine the least invasive conditions under which samples could be consistently collected. The *equilibration time* (tested at 45, 60 and 110 min) is the duration that hydrogels were allowed to dehydrate in the environment after removal from solution, affecting the tackiness of the hydrogel surface; the *dwell time* (tested at 30, 60 and 90 s) is the time the gel was in contact with the print, affecting the amount of sample collected. Subsequently, optimized conditions of an equilibrium time of 60 min and dwell time of 60 s were determined. High-resolution photographs of the sampled areas on the reference prints are shown in **Figure 3.9**, Appendix A.

Microscopic examination (**Figure 3.10**, Appendix A) revealed each of the micro-sampling devices collected several particles of colorant from the print. The average particle diameters were 4.71± 2.81, 3.07 ± 2.22, and 11.69 ± 9.66 µm for the safflower, sappan, and madder reference papers, respectively. These samples are sufficiently large for SERS analysis, demonstrating that the micro-sampling device can gently collect samples of colorant smaller than could be collected by typical (needle or scalpel) sampling methods and does so without permanent visible changes to the prints.

3.3.1.2 Investigation of possible hydrogel residues on prints post micro-sampling

A natural concern with new sampling methodologies are the potential long-term effects on the print that may arise by its interaction with the apparatus. **Figure 3.3**a shows representative positive ion mode DART mass spectra of animal glue-painted *kōzo* before and after sampling with an AMPS-co-PAA hydrogel, as well as mass spectra of reference materials. Analysis by DART-MS was selected because of the instrument's sensitivity, because of the pulsed, ablative, and depth-profiling nature of the ionizing gaseous flow, and because the method requires no alteration of the sample itself.

Because of the polymeric nature of the known components, i.e., polysaccharides from cellulosic paper, proteins in hide glue, and acrylate polymers of hydrogel, Kendrick Mass Defect (KMD) analysis[50-52] was used to resolve related peaks for each component. Representative DART mass spectra of four samples: 1. Blank *kōzo* , 2. *kōzo* painted with animal hide glue, 3. Hydrogel and 4. A sampled area of the same glue-painted *kōzo* were used to produce KMD scatter plots. Although the sample mixtures are complex, applying the same KMD analysis to all samples facilitates a direct comparison regarding the relative composition of each sample.

For this analysis, the same base unit (glucose) was applied, as cellulose from the *kōzo* paper was expected to be the most abundant component in the mixed samples. Two characteristic profiles were identified from sequential pulses and shared between samples 1, 2, and 4; one profile was observed early in the collection sequence, with the other arising later in sequence. This may be the result of the ionization process working through the surface layers on each sample. If gel residues were left behind on the paper, they would be observed in the earlier acquisition pulses. Overlaid KMD plots of these earlier acquisitions,

with peaks common to the background removed, can be seen in Figure 3.3b. The plots in Figure 3.3c-e show sample 4 compared to samples 1-3, respectively. For polymer mixtures it is common to observe oblique alignment of related peaks in the KMD analysis[53]. These are representative of peaks that are related, though not by the mass unit used for the KMD analysis. The strong correlation (particularly in the characteristic oblique alignment) between samples 1, 2, and 4 indicate that even the earliest measurements of the sampled area are comprised of only *kōzo* and glue. Close examination of sample 4 against sample 3 shows that there is minimal correlation to the most abundant peaks from the AMPS-co-PAA hydrogel network, indicating that no detectable residues were present on the paper.
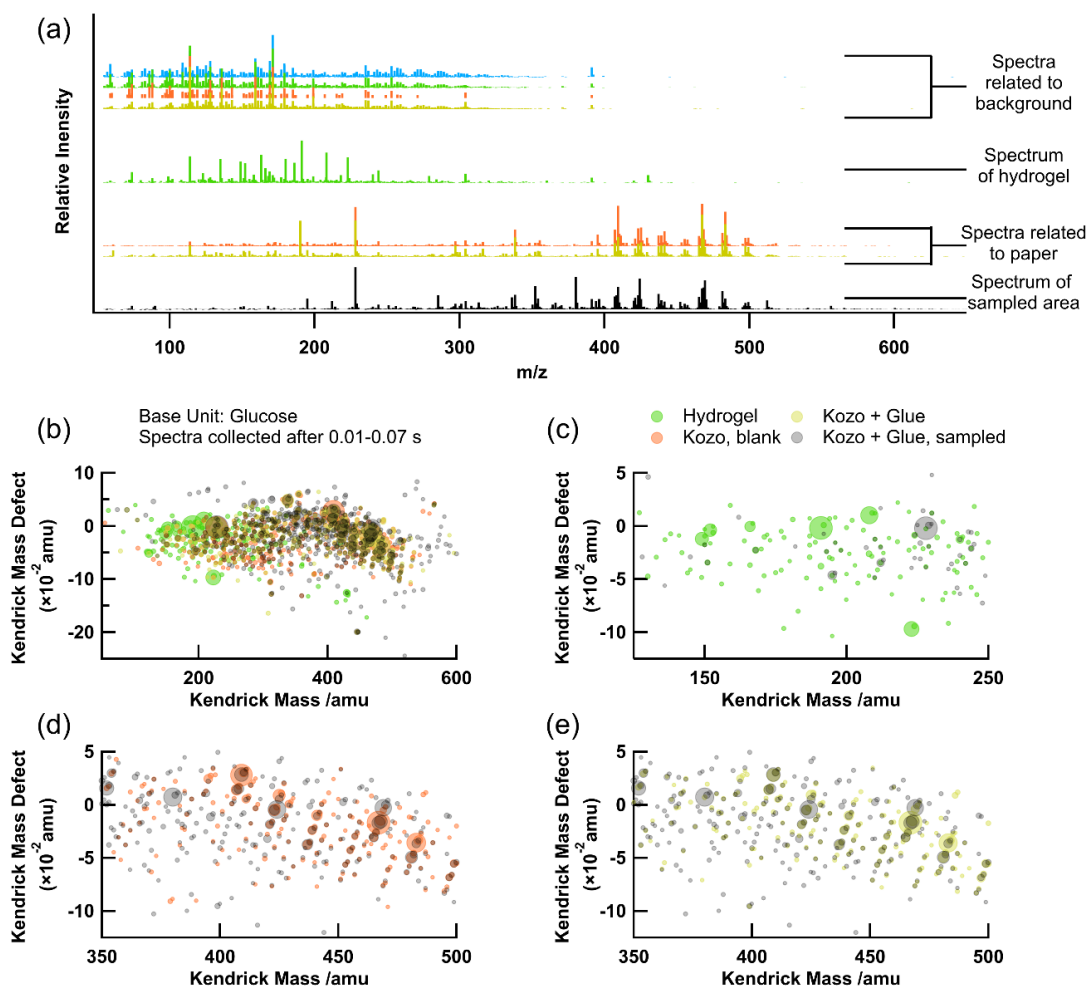
Figure 3.3*: (a)* Representative DART-MS spectra of the background, hydrogel, *kōzo* paper, *kōzo* painted with animal hide glue, and the glue-painted *kōzo* after sampling. *(b)* full-scale KMD plot (base unit: glucose, MW=180.156 g/mol) of representative spectra, and magnifications comparing the sampled area to *(c)* *kōzo*, (*d*) glue-painted *kōzo*, and *(e)* hydrogel. The size of the bubbles in the KMD plots correlate to the relative abundance of each peak in the mass spectrum.

3.3.2 Genetic Algorithm

3.3.2.1 Summary of spectral characterization of reference materials

Reference dyes were characterized via SERS in three relevant matrices— 1. solid lab-extracted dye standards, 2. as colorants (dyes mixed in hide glue binder) painted on reference prints, and 3. as 2. after UV-B aging. Images of the mock-up prints are provided

in Figure 3.9, Appendix A, and average SERS spectra of reference materials provided and described in a complementary publication[3].

3.3.2.2 Baseline Correction

The auto-adaptive baseline subtraction (AABLS) was applied to simulated Raman spectra and root-mean-squared-errors (RMSEs) were compared to the literature to assess the quality of correction. The parameters of the AABLS (number of iterations) were optimized by minimizing the RMSE as a function of iterations and the results are shown in Figure 3.11 (Appendix A). As the RMSE approaches zero, the baseline is improving. For this work the RMSE reached a minimum of 0.5152 after 200 iterations, which is comparable to literature precedent[48, 54, 55], as shown in Table 3.1. In real spectra, two large, unresolved peaks often remained, which likely arise from fluorescence that was not fully suppressed in the SERS measurements. The AABLS procedure was modified to only 50 iterations to remove more of these broad signals, as they are not indicative of SERS signal from colorant molecules. A 200-iteration and 50-iteration baseline correction were applied to a spectrum from a madder and sappan colorant mixture and are compared in Figure 3.4. The improved spectral resolution of shoulders in the broad, intense peaks indicate 50 iterations was optimal for molecular identification.

Table 3.1: Baseline correction method results previously published compared to this work. Citations in the Method column refer to the original report of the method; values in the RMSE column, with the exception of "This Work" were reported in [48]. All RMSE values were derived from the baseline correction of Equation 3.5.

Method	Parameters	RMSE[48]
Baek[54]	Fixed	8.969
airPLS[55]	$\lambda=10^4$	11.33
	$\lambda=10^5$	0.3119
	$\lambda=10^6$	0.5711
polynomial	Degree=1	16.17
	Degree=2	1.369
	Degree=3	4.495
AABLS [48]	Fixed	0.3606
This Work	Fixed	0.5152

2.3.2.3 Validation Tests

The GA was built through a circular sequential process of evaluating the GA solutions obtained from SERS spectra from test prints against an evolving library of reference spectra constructed from known reference materials. Test prints consisted of a single or mixture of red dyes bound in hide glue painted on *kōzo* and micro-sampled by hydrogel. An initial GA reference set consisted of 110 standard spectra, and was refined by analyzing the test prints and removing standard spectra that resulted in false positives or did not contribute to the GA fits. The final reference set consisted of 54 spectra—8 of hide glue, 10 of safflower, 16 of sappan, and 20 of madder.
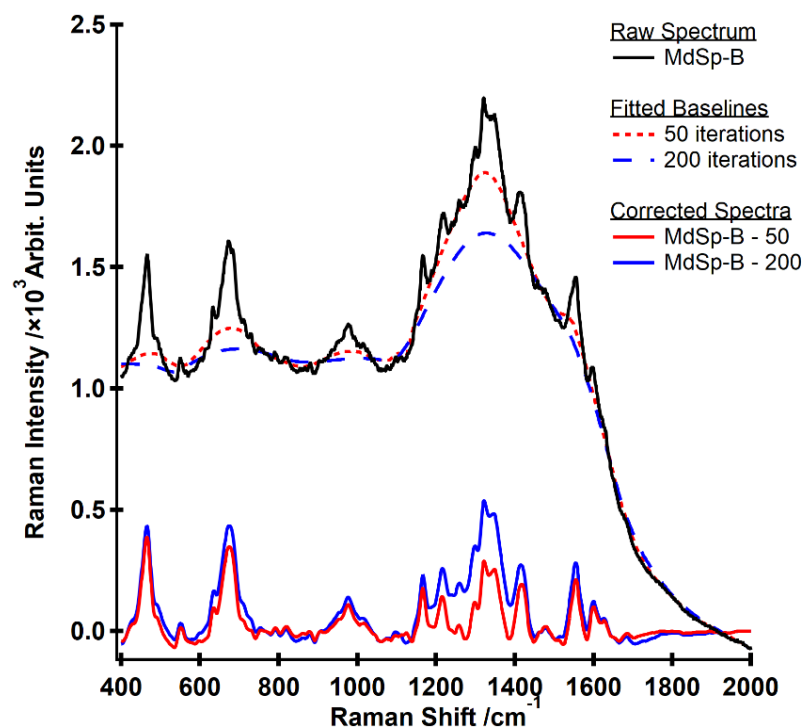
Figure 3.4: Example of AABLS application to a spectrum of mixed madder + sappan colorant. The red traces show the results of a 50 iteration AABLS and the blue traces show the results of a 200 iteration AABLS. While spectral intensities are lessened, the spectral definition of shoulders in the broad peaks from 1200-1700 cm^{-1} are improved with only 50 iterations.

The solutions of the GA or the "GA true match" was determined by the percent (out of 50 iterations) that the GA correctly identified all colorant components, which can be seen in Table 3.2. The GA identified at least one dye correctly ≥96% of the time and for 14 of 17 samples. For the remaining three samples, which were sappan mixed with hide glue, the GA solutions correctly identified one dye (sappan), 100% of the time, but also incorrectly identified the presence of another dye (either madder or safflower) between 60-100% of the time. The GA true match value was dependent on whether or not defining peaks in the SERS spectrum belonging to a dye were visible within the background matrix of hide glue. An example of a highly successful match from the GA is the synthetic dye

purpurin (one of the two chromophores in madder). The results in Table 3.2show that four colorants with purpurin dye-to-binder ratios ranging from 0.1:99.9 to 50:50 wt% were successfully matched by the GA 100% of the time. These colorants were, however, less complex than the remaining test samples, as the purpurin was commercially produced and 95% pure.

Aside from the set of commercially purified purpurin dye, the remaining test prints were made using dyes extracted from plant material according to the procedures published elsewhere [3] and not otherwise purified before mixing with hide glue and painting onto *kōzo*. All the dyes in this study likely interact with the SERS substrate through metal coordination to phenol groups. Larger molecules like carthamin, the colorant in safflower, which are highly fluorescent and have a relatively small number of interacting sites, do not participate as readily in the metal coordination interaction. Other factors, such as pH and light, may affect the structure[56-58] and in turn the appearance and chemical behavior of brazilein in sappan. In addition to complex matrices of the colorants themselves, the heterogeneity of dye-containing particles suspended in the hide glue binder make it likely that contributions from all components would vary sample-to-sample. To account for that variability multiple spectra were measured from each sample collected by micro-sampling. An example of the average GA best fit for a test colorant is shown in Figure 3.5.

Table 3.2: Results of GA Validation Tests. Actual compositions reflect the colorants as prepared in the lab, not the individual micro-samples analyzed by SERS. Values below the 15% contribution threshold are presented in gray, italicized text. R is the correlation coefficient.

| Sample | wt% composition of heterogeneous mixture (% of time dye identified in GA solution) | | | | Average % Contribution from GA (Standard Deviation) | | | | Average R | GA % match to dye(s) ID |
	hide glue	safflower	sappan	madder	hide glue	safflower	sappan	madder		
P-A	99.9	(0)	(0)	0.1* (100)	0.4 (1.1)	0.0 (0.1)	0.0 (0.1)	99.5 (1.3)	0.9311	100
P-B	75.0	(0)	(0)	25.0* (100)	2.4 (2.0)	0.1 (0.2)	0.0 (0.2)	97.5 (2.3)	0.9444	100
P-C	66.9	(0)	(0)	33.1* (100)	14.8 (5.7)	0.4 (0.7)	0.3 (0.8)	84.4 (5.8)	0.7353	100
P-D	49.8	(0)	(0)	50.2* (100)	1.6 (2.0)	0.1 (0.2)	0.0 (0.1)	98.4 (1.0)	0.9564	100
Sf-H	83.0	10.2 (100)	(0)	(0)	44.4 (9.8)	47.8 (10.1)	5.3 (2.6)	2.4 (2.6)	0.7852	100
Sf-C	84.4	15.6 (100)	(0)	(0)	6.3 (3.3)	89.3 (5.6)	1.5 (2.3)	2.9 (3.6)	0.8305	100
Sf-A	83.0	10.2 (100)	(0)	(30)	12.8 (5.1)	74.5 (6.6)	0.2 (0.5)	12.5 (5.9)	0.8962	70
Md-F	50.1	(0)	(0)	49.9 (100)	2.4 (1.5)	0.0 (0.1)	0.8 (0.4)	96.7 (1.3)	0.8756	100
Md-C	90.9	(0)	(4)	9.1 (100)	30.8 (9.0)	0.4 (1.0)	2.1 (4.7)	66.7 (10.8)	0.6859	96
Md-E	63.9	(0)	(18)	36.1 (100)	41.7 (20.5)	0.1 (0.3)	9.0 (5.0)	54.1 (20.0)	0.6155	82
Md-G	89.1	(16)	(10)	10.9 (96)	48.1 (17.4)	8.3 (7.3)	5.9 (6.2)	37.7 (16.0)	0.7596	76
Sp-D	87.8	(60)	12.2 (100)	(0)	10.1 (5.7)	20.8 (10.2)	67.0 (12.2)	2.1 (1.3)	0.6229	40
Sp-H	66.4	(0)	33.6 (100)	(86)	12.9 (5.2)	5.4 (2.7)	57.5 (11.4)	24.2 (11.3)	0.8777	14
Sp-G	81.0	(0)	19.0 (100)	(100)	2.5 (3.0)	3.2 (3.2)	55.2 (4.6)	39.1 (6.4)	0.8131	0

Sample										
Md Sp-B	83.0	(0)	6.8 (100)	10.2 (100)	3.2 (2.7)	4.2 (2.6)	64.1 (3.4)	28.4 (4.3)	0.9159	100
SfSp-B	80.2	8.2 (100)	11.5 (62)	(0)	12.3 (5.5)	69.7 (6.5)	15.7 (2.0)	2.2 (1.8)	0.8249	62
Sf Md-A	83.0	10.2 (100)	(0)	6.8 (58)	28.7 (8.4)	54.6 (10.7)	1.3 (1.6)	15.5 (7.6)	0.9116	58

Sample labels are as follows: P=purpurin, Sf=safflower, Sp=sappan, and Md=madder; subsequent letter designations are used to differentiate samples with the same components.

*wt% of synthetic pupurin, a color contributing compound of madder.

In cases of mixed colorants, such as SfSp-Band MdSp-B, both colorants were identified by the GA, and the standard deviations for both were less than 6.5%, indicating that the GA was able to reliably identify the present components in separate iterations. However, the spectral best fit included other dyes from the reference set (thus the ~10% variance in the second-highest contributor, in single-colorant samples). The need for spectra that act as correlation "fillers" is likely due to the complexity of the sample matrix that comes with naturally extracted colorants.
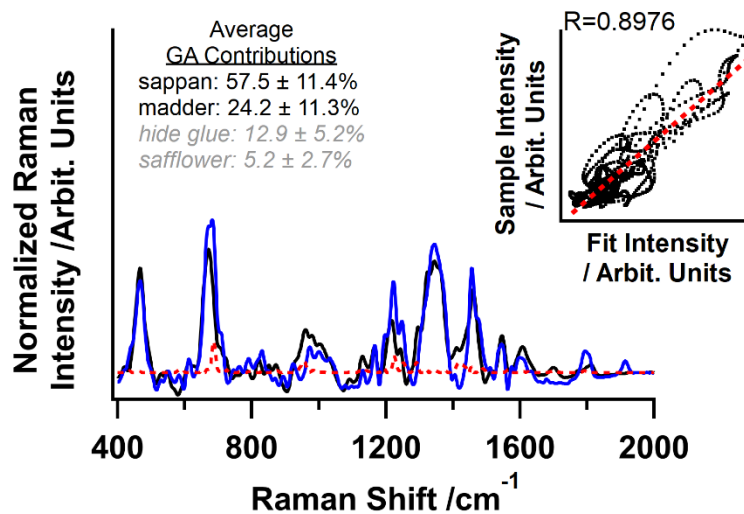
Figure 3.5: Example GA fit result for an ink composed of sappan and hide glue only. Sample spectrum (blue), Generated fit spectrum (black), Squared difference between the sample and fit (red), which was used to calculate the Figure of Merit during the GA analysis. The inset shows the correlation between the sample spectrum and the generated fit spectrum.

GA solutions can be reached from local, rather than global, best fits. Therefore, 50 iterations of GA solutions were averaged and reported as a mean % and standard deviation of each dye's contribution to the GA fit. Spectra having the most incorrect results, such as in the sappan-only colorants, demonstrate the challenges to interpreting the GA. In those

34

samples, Sp-D, Sp-G, and Sp-H, sappan was identified as the highest contributor to the resulting spectrum, with values ranging from 55-67% of the total spectral contribution. The second highest contributor in all three cases were other colorants. For Sp-D, safflower contributed 20.8% to the spectral fit. For Sp-G and Sp-H, madder was the second highest contributor with 39.1% and 24.2%, respectively. Because we have defined "GA true match" as a binary parameter, when other incorrect dyes are included in the result, the defined true match rate decreases. While those incorrect secondary dyes contributed more than the negligible cutoff of 15% to the final result, the relative standard deviation in the incorrect dye's spectral contribution was more than twice that of sappan's spectral contribution.

The definitions and cutoffs (i.e. "GA true match" and ≥15% threshold) were terms defined for this data set and are somewhat arbitrary. Alternatively, we could use standard deviation in our "GA true match" calculation and affect the results. Ultimately, because GA solutions are a weighted average of spectra determined by the algorithm, the GA result can be easily interpreted just as any SER spectrum. The ability to interpret the solution(s) is an advantage to the technique, compared to cluster methods. GA analysis is a more rapid spectral evaluation method than traditional, peak-by-peak analysis of mixtures.
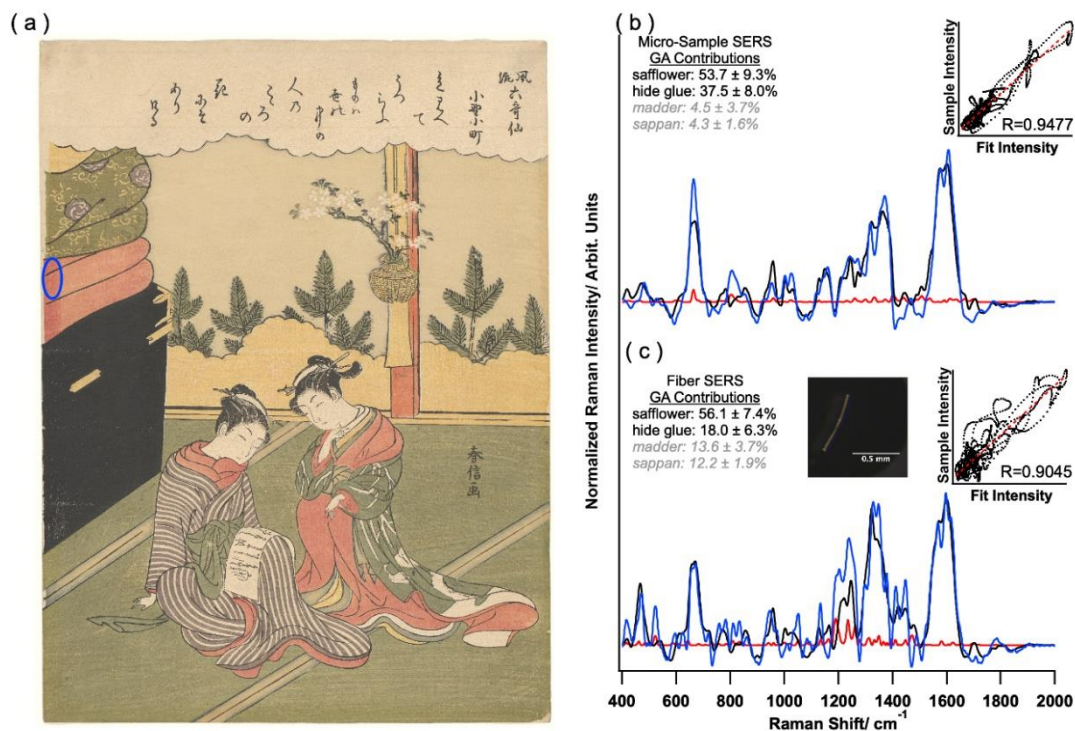
Figure 3.6: (a) Suzuki Harunobu, *Ono no Komachi, from the series Fūryū rokkasen (The Fashionable Six Poetic Immortals)*, 1768, color woodblock print on paper, The Mary Andrews Ladd Collection, Portland Art Museum, Portland, Oregon, 32.75. (b) Micrograph of single fiber collected from the print (from the region circled in (a)). (c) SERS spectra and GA fitting results for analysis of the single fiber and a micro-sample collected from the same region. Image reproduced with permission from the Portland Art Museum.

3.3.3 Application of method to historical woodblock prints

Figure 3.6 shows an image of PAM.32.75, a micrograph of a single fiber collected from the left edge of the print, and SERS spectra from both the fiber and a micro-sample collected from the same area. This fiber was able to be collected because it was near the edge and already lifted from the paper.

The historical woodblock print, PAM.32.83, attributed to Suzuki Harunobu, was selected because it includes three unique red color fields of interest. Each of these color fields—the light pink wall, the medium pink-peach baseboard, and the central figure's red
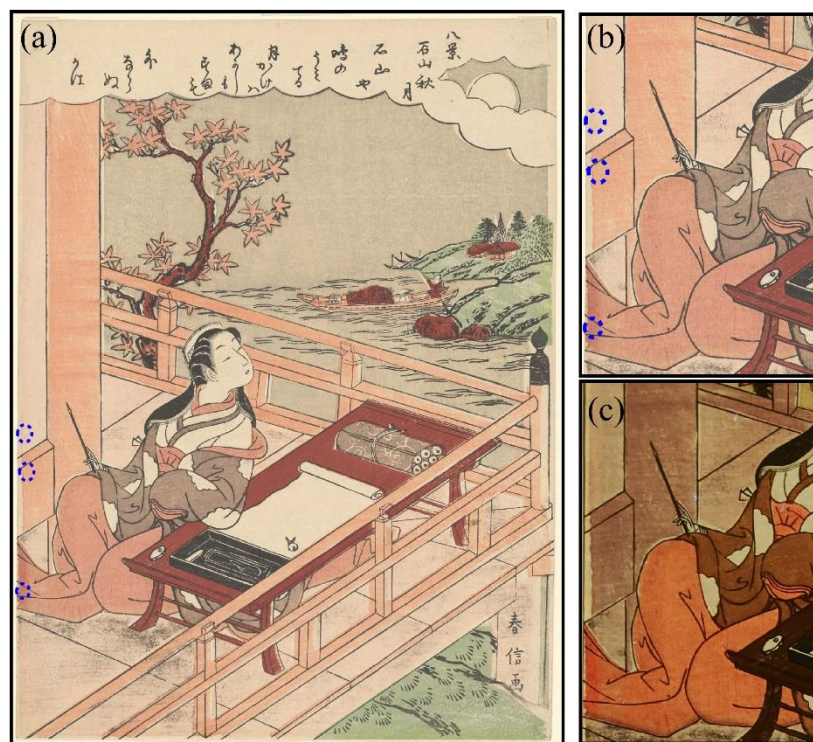
Figure 3.7: *(a)* Suzuki Harunobu*, Ishiyama no shūgetsu (Autumn Moon at Ishiyama), from an untitled series of Ōmi hakkei (Eight Views of Ōmi)*1768/1769, color woodblock print on paper, The Mary Andrews Ladd Collection, Portland Art Museum, Portland, Oregon, 32.83. Magnified images of left edge under *(b)* white light and *(c)* UV light illumination. Blue circles in *(b)* indicate general areas that were micro-sampled. Images reproduced with permission from the Portland Art Museum.

inner kimono—were printed to the edge of the paper, providing discrete access to three different red colorants. Images of the print are shown in Figure 3.7.

3.3.3.1 Description of preliminary analyses

Before sampling with the micro-sampling device for analysis by SERS, PAM.32.83 and PAM.32.75 were imaged under white and UV light illumination and surveyed by non-destructive XRF analysis. In the UV-illuminated image of PAM.32.83 (Figure 3.7c), it is evident that the kimono area was fluorescent, whereas the other two areas were not.

3.3.3.2 Micro-sampling

Micro-sampling of PAM.32.75 was carried out under the optimized sampling parameters as described in section 3.3. Images of the gel surface were collected under 50× magnification before application of the AgNPs. The micro-sample from PAM.32.75 collected particles with average diameter of 4.62 ± 2.27 μm.

Micro-samples were collected from PAM.32.83 in a similar fashion. For the light wall, 55 particles were identified in the image with average diameter of 3.10 ± 3.17 μm. Twenty-two particles were identified on the gel from the medium baseboard and the average diameter was 3.32 ± 0.89 μm. The gel from the kimono area revealed only five particles with average diameter of 9.29 ± 2.54 μm. Images collected after sampling showed no evidence of permanent visible changes to the print.

3.3.3.3 SERS Results

The spectra from PAM.32.75 are shown in Figure 3.6b and c. Extractionless analysis on textile fibers has previously been reported[59], however the HF hydrolysis method is more common. Spectra collected from the fiber were similar to those collected

from micro-samples and the GA returned similar spectral contributions (56.1% and 53.7% safflower, respectively). From these data it was determined that the red futon along the left edge was printed with a safflower colorant. These data show that analysis of micro-samples presented herein returns data comparable to extractionless, non-hydrolysis SERS on a collected single fiber.

Multiple spectra were collected for each micro-sample, to account for previously described variability from matrix effects and heterogeneity of colorants. Indeed, not all parts of the same sample were identical. One sample spectrum (Figure 3.8a) from the light wall best correlated to only hide glue, with 92.3% of the total spectral contribution. Another sample spectrum (Figure 3.8b) was identified by the GA as hide glue ($67.5 \pm 25.9\%$) and madder ($31.1 \pm 25.4\%$). But, in the second spectrum, the relative variance associated with madder is large (2.1 times larger than the relative variance of the glue contribution), suggesting the colorant component was too dilute in the collected sample to be accurately detected by GA. This determination is supported by the very pale pink coloration of the light wall region. Due to the high variance in the GA results, colorant determination in this area was inconclusive.

For the kimono, three similar spectra were collected, an example of which can be seen in Figure 3.8c, with GA contributions ranging from 42.4-59.3% hide glue and 40.5-57.3% madder. The relative variances for both the hide glue and madder contributions were higher than demonstrated in the test prints (28.5-42.1% variance). Given the larger variances and that the GA consistently identified the same two components, we conclude that the spectral contributions of the components were similar. A fourth spectrum (Figure 3.8d) showed differences in the spectral profile, and resulted in $90.9 \pm 6.0\%$ contribution

from madder. These combined results indicate the kimono was printed with an colorant colored with madder.

Five spectra were collected and analyzed by GA from the medium baseboard sample. In one spectrum, colorant was not detectable. Evaluation of three other spectra indicated contributions from hide glue and madder (Figure 3.8e). A fifth spectrum indicated spectral contributions from hide glue, madder, and safflower, all with similar relative variances (Figure 3.8f). Close inspection of the sample spectrum shown in Figure 3.8f shows similarities to madder, specifically with peaks at 944, 1159, and 1211 cm^{-1}. Peaks attributed to safflower are 464, 779, 1116, 1345, and 1605 cm^{-1}. Several peaks are present in both safflower and madder spectra at (e.g., 616, 857, 1025, 1364, 1455, 1605 and 1615 cm^{-1}), though the 1455 and 1605 cm^{-1} peaks, in particular, are more prevalent in safflower than in madder. Considering all of the data, it is likely that both safflower and madder colorants were used in the printing of the medium baseboard.
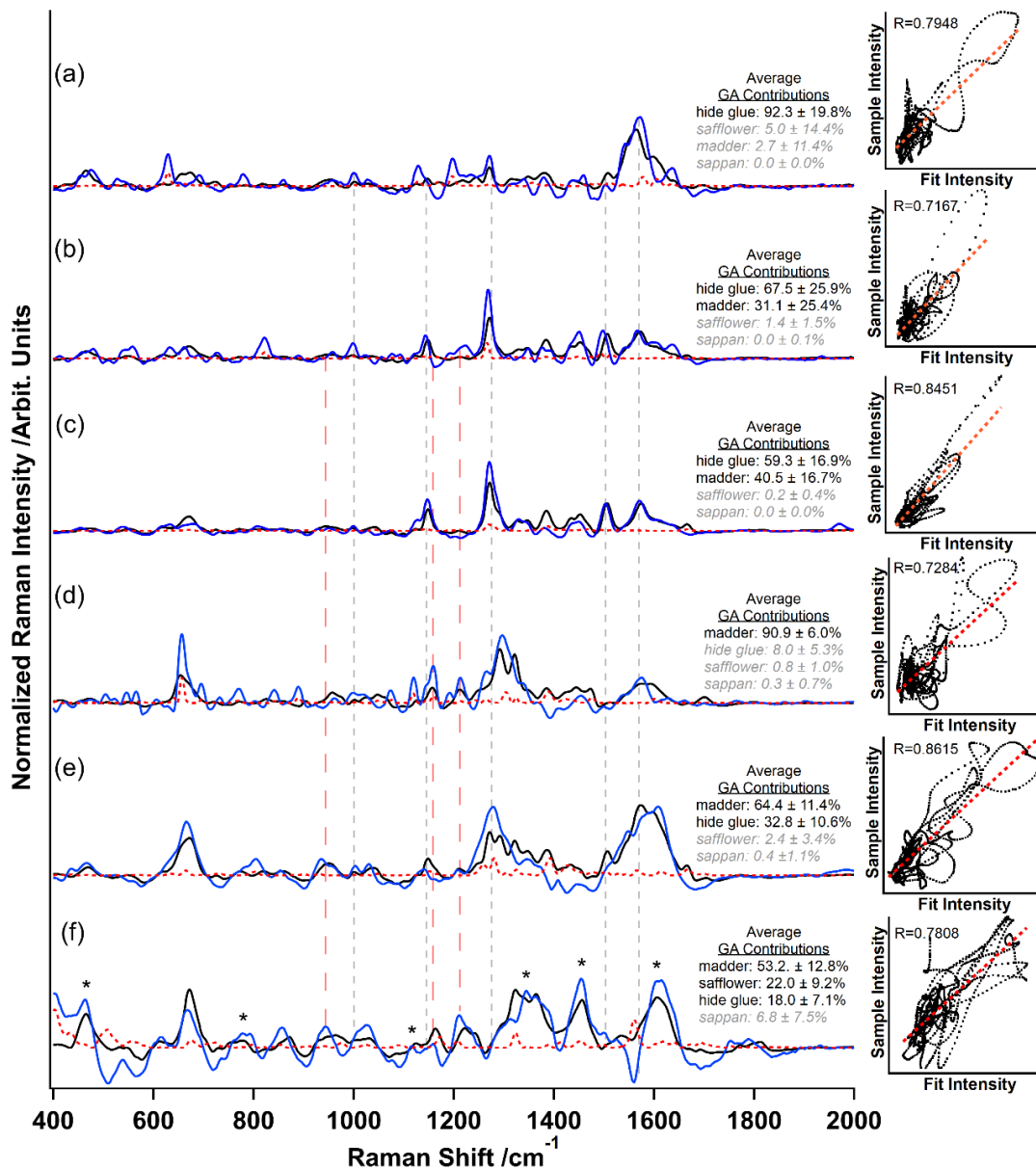
Figure 3.8: Results of GA fitting on spectra collected from *Ishiyama no shūgetsu (Autumn Moon at Ishiyama)*. Blue traces are the sample spectra, black traces are the fit spectrum, and the dashed red traces are the Figure of Merit, as described in the text. *(a)* and *(b)* spectra are from the light wall area, *(c)* and *(d)* spectra are from the kimono, and *(e)* and *(f)* spectra are from the medium baseboard. Plots to the right show the correlation between the sample spectrum and the resulting fit spectrum. Gray vertical dashed lines indicate peaks attributed to hide glue, pink vertical dashed lines indicate peaks attributed to madder, and asterisks indicate peaks attributed to safflower.

41

3.4 Conclusions

Through this work, the data show that micro-scale samples of colorants can be identified using the SERS methodology and GA analysis described. It is possible to modify the gel composition and its liquid phase to optimize or facilitate the extraction of a wide variety or select target. The general methodology may find other applications, such as in environmental monitoring or forensics.

Spectral interpretation was aided by fitting with a genetic algorithm, allowing for rapid sampling and analysis, without additional sample workup. When applied to a print in the permanent collection at the Portland Art Museum, results from the analysis indicate the presence of madder and a safflower-madder mixture on the same print. A similar conclusion was made in another study of a works attributed to Harunobu[60], though with the known drawbacks of EEM, that conclusion, particularly the presence of madder, had been questionable. The use of madder as a colorant in Harunobu's time is a point of debate in the technical art history field; these data support the conclusion that madder was in use in late 18th century Japan. A more extensive survey of the PAM's Harunobu collection has been performed and the full results of that study are forthcoming.

This work demonstrates the utility of genetic algorithm to expedite spectral interpretation, however given the insular nature of each SERS method, a single genetic algorithm may not be adaptable for all situations and the results require scrutiny by skilled spectroscopists. While this is the first demonstration of the use of GAs to identify organic colorants in art, additional investigations are needed to further optimize and expand the abilities of genetic algorithms as applied to SERS data of organic colorants.

3.5 References

1.   Cesaratto, A.; Luo, Y.-B.; Smith, H. D.; Leona, M., A timeline for the introduction of synthetic dyestuffs in Japan during the late Edo and Meiji periods. *Heritage Sci.* **2018,** *6* (1), 22.

2.   Derrick, M.; Newman, R.; Wright, J., Characterization of Yellow and Red Natural Organic Colorants on Japanese Woodblock Prints by EEM Fluorescence Spectroscopy. *J. Am. Inst. Conserv.* **2017,** *56* (3-4), 171-193.

3.   Kissell, L. N.; Quady, T. K.; Clare, T. L., Reference data set and characterization of Japanese print materials by Surface-Enhanced Raman Spectroscopy and documentation of non-damage. *Data in Brief* (Submitted).

4.   Mounier, A.; Le Bourdon, G.; Aupetit, C.; Lazare, S.; Biron, C.; Pérez-Arantegui, J.; Almazán, D.; Aramendia, J.; Prieto-Taboada, N.; Fdez-Ortiz de Vallejuelo, S.; Daniel, F., Red and blue colours on 18th–19th century Japanese woodblock prints: In situ analyses by spectrofluorimetry and complementary non-invasive spectroscopic methods. *Microchem. J.* **2018,** *140*, 129-141.

5.   Pérez-Arantegui, J.; Rupérez, D.; Almazán, D.; Díez-de-Pinos, N., Colours and pigments in late ukiyo-e art works: A preliminary non-invasive study of Japanese woodblock prints to interpret hyperspectral images using in-situ point-by-point diffuse reflectance spectroscopy. *Microchem. J.* **2018,** *139*, 94-109.

6.   Vermeulen, M.; Leona, M., Evidence of early amorphous arsenic sulfide production and use in Edo period Japanese woodblock prints by Hokusai and Kunisada. *Heritage Sci.* **2019,** *7* (1), 73.

7.   Vermeulen, M.; Tamburini, D.; Müller, E. M. K.; Centeno, S. A.; Basso, E.; Leona, M., Integrating liquid chromatography mass spectrometry into an analytical protocol for the identification of organic colorants in Japanese woodblock prints. *Sci. Rep.* **2020,** *10* (1).

8.   Villafana, T.; Edwards, G., Creation and reference characterization of Edo period Japanese woodblock printing ink colorant samples using multimodal imaging and reflectance spectroscopy. *Heritage Sci.* **2019,** *7* (1).

9.   Leona, M.; Decuzzi, P.; Kubic, T. A.; Gates, G.; Lombardi, J. R., Nondestructive Identification of Natural and Synthetic Organic Colorants in Works of Art by Surface Enhanced Raman Scattering. *Anal. Chem.* **2011,** *83* (11), 3990-3993.

10.   Colbourne, J., Conserving Japanese Wood-block Prints with a Brief Study of the Materials Used in their Conservation. *de arte* **1993,** *28* (48), 44-49.

11.   Keyes, R. S.; Feller, R. L., *Japanese woodblock prints: a catalogue of the Mary A. Ainsworth Collection*. Allen Memorial Art Museum: 1984.

12.   Conservation, A. I. f. Code of Ethics. https://www.culturalheritage.org/about-conservation/code-of-ethics (accessed June 17, 2020).

13.   Castro, K.; Pérez-Alonso, M.; Rodríguez-Laso, M. D.; Etxebarria, N.; Madariaga, J. M., Non-invasive and non-destructive micro-XRF and micro-Raman analysis of a decorative wallpaper from the beginning of the 19th century. *Anal. Bioanal. Chem.* **2007,** *387* (3), 847-860.

14.   Castro, K.; Pessanha, S.; Proietti, N.; Princi, E.; Capitani, D.; Carvalho, M. L.; Madariaga, J. M., Noninvasive and nondestructive NMR, Raman and XRF analysis of a

Blaeu coloured map from the seventeenth century. *Anal. Bioanal. Chem.* **2008,** *391* (1), 433-441.

15.   Vermeulen, M.; Mueller, E. M.; Leona, M., Non-invasive study of the evolution of pigments and colourants use in 19th century ukiyo-e. *Arts of Asia* 2020, p 103.

16.   Bruni, S.; Guglielmi, V.; Pozzi, F., Historical organic dyes: a surface-enhanced Raman scattering (SERS) spectral database on Ag Lee–Meisel colloids aggregated by NaClO4. *J. Raman Spectrosc.* **2011,** *42* (6), 1267-1281.

17.   Cañamares, M. V.; Mieites-Alonso, M. G.; Leona, M., Fourier transform-Raman and surface-enhanced Raman spectroscopy analysis of safflower red-dyed washi paper: pH study and bands assignment. *J. Raman Spectrosc.* **2020,** *51* (6), 903-909.

18.   Whitney, A. V.; Van Duyne, R. P.; Casadio, F., An innovative surface-enhanced Raman spectroscopy (SERS) method for the identification of six historical red lakes and dyestuffs. *J. Raman Spectrosc.* **2006,** *37* (10), 993-1002.

19.   de Oliveira, L. F. C.; Edwards, H. G. M.; Velozo, E. S.; Nesbitt, M., Vibrational spectroscopic study of brazilin and brazilein, the main constituents of brazilwood from Brazil. *Vib. Spectrosc.* **2002,** *28* (2), 243-249.

20.   Edwards, H. G. M.; de Oliveira, L. F. C.; Nesbitt, M., Fourier-transform Raman characterization of brazilwood trees and substitutes. *Analyst* **2003,** *128* (1), 82-87.

21.   Leona, M.; Stenger, J.; Ferloni, E., Application of surface-enhanced Raman scattering techniques to the ultrasensitive identification of natural dyes in works of art. *J. Raman Spectrosc.* **2006,** *37* (10), 981-992.

22.   Amato, F.; Micciche', C.; Cannas, M.; Gelardi, F. M.; Pignataro, B.; Li Vigni, M.; Agnello, S., Ag nanoparticles agargel nanocomposites for SERS detection of cultural heritage interest pigments. *The European Physical Journal Plus* **2018,** *133* (2), 74.

23.   Sessa, C.; Weiss, R.; Niessner, R.; Ivleva, N. P.; Stege, H., Towards a Surface Enhanced Raman Scattering (SERS) spectra database for synthetic organic colourants in cultural heritage. The effect of using different metal substrates on the spectra. *Microchem. J.* **2018,** *138*, 209-225.

24.   Pozzi, F.; Lombardi, J. R.; Bruni, S.; Leona, M., Sample treatment considerations in the analysis of organic colorants by surface-enhanced Raman scattering. *Anal Chem* **2012,** *84* (8), 3751-7.

25.   Baran, A.; Wrzosek, B.; Bukowska, J.; Proniewicz, L.; Baranska, M., Analysis of alizarin by surface-enhanced and FT-Raman spectroscopy. *J. Raman Spectrosc.* **2009,** *40* (4), 436-441.

26.   Van Elslande, E.; Lecomte, S.; Le Hô, A. S., Micro-Raman spectroscopy (MRS) and surface-enhanced Raman scattering (SERS) on organic colourants in archaeological pigments. *J. Raman Spectrosc.* **2008,** *39* (8), 1001-1006.

27.   Chen, K.; Leona, M.; Vo-Dinh, K.-C.; Yan, F.; Wabuyele, M. B.; Vo-Dinh, T., Application of surface-enhanced Raman scattering (SERS) for the identification of anthraquinone dyes used in works of art. *J. Raman Spectrosc.* **2006,** *37* (4), 520-527.

28.   Chen, K.; Vo-Dinh, K.-C.; Yan, F.; Wabuyele, M. B.; Vo-Dinh, T., Direct identification of alizarin and lac dye on painting fragments using surface-enhanced Raman scattering. *Anal. Chim. Acta* **2006,** *569* (1-2), 234-237.

29.   Murcia-Mascarós, S.; Domingo, C.; Sanchez-Cortes, S.; Canamares, M.; Garcia-Ramos, J., Spectroscopic identification of alizarin in a mixture of organic red dyes by incorporation in Zr-Ormosil. *J. Raman Spectrosc.* **2005,** *36* (5), 420-426.

30.   Canamares, M.; Garcia-Ramos, J.; Domingo, C.; Sanchez-Cortes, S., Surface-enhanced Raman scattering study of the adsorption of the anthraquinone pigment alizarin on Ag nanoparticles. *J. Raman Spectrosc.* **2004,** *35* (11), 921-927.

31.   Shadi, I. T.; Chowdhry, B. Z.; Snowden, M. J.; Withnall, R., Semi-quantitative analysis of alizarin and purpurin by surface-enhanced resonance Raman spectroscopy (SERRS) using silver colloids. *J. Raman Spectrosc.* **2004,** *35* (8-9), 800-807.

32.   Gullekson, C.; Lucas, L.; Hewitt, K.; Kreplak, L., Surface-sensitive Raman spectroscopy of collagen I fibrils. *Biophys J* **2011,** *100* (7), 1837-45.

33.   Nevin, A.; Osticioli, I.; Anglos, D.; Burnstock, A.; Cather, S.; Castellucci, E., Raman Spectra of Proteinaceous Materials Used in Paintings: A Multivariate Analytical Approach for Classification and Identification. *Anal. Chem.* **2007,** *79* (16), 6143-6151.

34.   Le Ru, E. C.; Etchegoin, P. G., *Principals of Surface-Enhanced Raman Spectroscopy and related plasmonic effects*. First edition ed.; Elsevier: 2009; p 663.

35.   Lombardi, J. R.; Birke, R. L.; Lu, T.; Xu, J., Charge-transfer theory of surface enhanced Raman spectroscopy: Herzberg–Teller contributions. *The Journal of Chemical Physics* **1986,** *84* (8), 4174-4180.

36.   Bruni, S.; Guglielmi, V.; Pozzi, F., Surface-enhanced Raman spectroscopy (SERS) on silver colloids for the identification of ancient textile dyes: Tyrian purple and madder. *J. Raman Spectrosc.* **2009,** *41* (2), 175-180.

37.   Platania, E.; Lombardi, J. R.; Leona, M.; Shibayama, N.; Lofrumento, C.; Ricci, M.; Becucci, M.; Castellucci, E., Suitability of Ag-agar gel for the micro-extraction of organic dyes on different substrates: the case study of wool, silk, printed cotton and a panel painting mock-up. *J. Raman Spectrosc.* **2014,** *45* (11-12), 1133-1139.

38.   Lofrumento, C.; Ricci, M.; Platania, E.; Becucci, M.; Castellucci, E., SERS detection of red organic dyes in Ag-agar gel. *J. Raman Spectrosc.* **2013,** *44* (1), 47-54.

39.   Cheung, W.; Shadi, I. T.; Xu, Y.; Goodacre, R., Quantitative Analysis of the Banned Food Dye Sudan-1 Using Surface Enhanced Raman Scattering with Multivariate Chemometrics. *J. Phys. Chem. C* **2010,** *114* (16), 7285-7290.

40.   Ai, Y. J.; Liang, P.; Wu, Y. X.; Dong, Q. M.; Li, J. B.; Bai, Y.; Xu, B. J.; Yu, Z.; Ni, D., Rapid qualitative and quantitative determination of food colorants by both Raman spectra and Surface-enhanced Raman Scattering (SERS). *Food Chem* **2018,** *241*, 427-433.

41.   Dies, H.; Raveendran, J.; Escobedo, C.; Docoslis, A., Rapid identification and quantification of illicit drugs on nanodendritic surface-enhanced Raman scattering substrates. *Sens. Actuators B* **2018,** *257*, 382-388.

42.   Wang, K.; Xu, B.; Wu, J.; Zhu, Y.; Guo, L.; Xie, J., Elucidating fentanyls differentiation from morphines in chemical and biological samples with surface-enhanced Raman spectroscopy. *Electrophoresis* **2019,** *40* (16-17), 2193-2203.

43.   Gniadecka, M.; Wulf, H. C.; Mortensen, N. N.; Nielsen, O. F.; Christensen, D. H., Diagnosis of basal cell carcinoma by Raman spectroscopy. *J. Raman Spectrosc.* **1997,** *28* (2-3), 125-129.

44.   Banaei, N.; Moshfegh, J.; Mohseni-Kabir, A.; Houghton, J. M.; Sun, Y.; Kim, B., Machine learning algorithms enhance the specificity of cancer biomarker detection using SERS-based immunoassays in microfluidic chips. *RCS Adv.* **2019,** *9* (4), 1859-1868.
45.   Jeffrey Kuo, C.-F.; Su, T.-L.; Tsai, J.-C.; Pan, S.-S., The optimization of the surface-enhanced Raman scattering for quantitative analysis and detection of molecules. *Textile Research Journal* **2016,** *86* (14), 1474-1486.
46.   Pozzi, F.; Porcinai, S.; Lombardi, J. R.; Leona, M., Statistical methods and library search approaches for fast and reliable identification of dyes using surface-enhanced Raman spectroscopy (SERS). *Analytical Methods* **2013,** *5* (16), 4205-4212.
47.   England, A. H.; Clare, T. L., Synthesis and Characterization of Flexible Hydrogel Electrodes for Electrochemical Impedance Measurements of Protective Coatings on Metal Sculptures. *Electroanalysis* **2014,** *26* (5), 1059-1067.
48.   Xie, Y.; Yang, L.; Sun, X.; Wu, D.; Chen, Q.; Zeng, Y.; Liu, G., An auto-adaptive background subtraction method for Raman spectra. *Spectrochim. Acta Part A* **2016,** *161*, 58-63.
49.   Grefenstette, J. J., Optimization of control parameters for genetic algorithms. *IEEE Transactions on systems, man, and cybernetics* **1986,** *16* (1), 122-128.
50.   Fouquet, T. N. J., The Kendrick analysis for polymer mass spectrometry. *Journal of Mass Spectrometry* **2019,** *54* (12), 933-947.
51.   Fouquet, T. N. J.; Cody, R. B.; Ozeki, Y.; Kitagawa, S.; Ohtani, H.; Sato, H., On the Kendrick Mass Defect Plots of Multiply Charged Polymer Ions: Splits, Misalignments, and How to Correct Them. *J Am Soc Mass Spectrom* **2018,** *29* (8), 1611-1626.
52.   Cody, R. B.; Fouquet, T., Paper spray and Kendrick mass defect analysis of block and random ethylene oxide/propylene oxide copolymers. *Anal. Chim. Acta* **2017,** *989*, 38-44.
53.   Fouquet, T.; Sato, H., Improving the Resolution of Kendrick Mass Defect Analysis for Polymer Ions with Fractional Base Units. *Mass Spectrometry* **2017,** *6* (1), A0055-A0055.
54.   Baek, S.-J.; Park, A.; Kim, J.; Shen, A.; Hu, J., A simple background elimination method for Raman spectra. *Chemometrics and Intelligent Laboratory Systems* **2009,** *98* (1), 24-30.
55.   Zhang, Z.-M.; Chen, S.; Liang, Y.-Z., Baseline correction using adaptive iteratively reweighted penalized least squares. *Analyst* **2010,** *135* (5), 1138-1146.
56.   Rondão, R.; Seixas de Melo, J. S.; Pina, J.; Melo, M. J.; Vitorino, T.; Parola, A. J., Brazilwood Reds: The (Photo)Chemistry of Brazilin and Brazilein. *J. Phys. Chem. A* **2013,** *117* (41), 10650-10660.
57.   Vitorino, T.; Melo, M. J.; Carlyle, L.; Otero, V., New insights into brazilwood lake pigments manufacture through the use of historically accurate reconstructions. *Studies in Conservation* **2016,** *61* (5), 255-273.
58.   Ngamwonglumlert, L.; Devahastin, S.; Chiewchan, N.; Raghavan, G. S. V., Color and molecular structure alterations of brazilein extracted from Caesalpinia sappan L. under different pH and heating conditions. *Sci Rep* **2020,** *10* (1), 12386.
59.   Zaffino, C.; Bruni, S.; Guglielmi, V.; De Luca, E., Fourier-transform surface-enhanced Raman spectroscopy (FT-SERS) applied to the identification of natural dyes in

textile fibers: an extractionless approach to the analysis. *J. Raman Spectrosc.* **2014,** *45* (3), 211-218.

60.   Wright, J.;   Derrick, M.; Adachi, M., The colors of desire: Beauties of the Yoshiwara observed. *Harunobu from the Museum of Fine Arts, Boston. Tokyo: Nikkei* **2017**, 259-63.

61.   Maynez-Rojas, M. A.; Casanova-González, E.; Ruvalcaba-Sil, J. L., Identification of natural red and purple dyes on textiles by Fiber-optics Reflectance Spectroscopy. *Spectrochim. Acta Part A* **2017,** *178*, 239-250.

3.6 Appendix A: Supporting Information for Optimized micro-sampling and computational

analysis for SERS identification of red organic colorants

The simulated spectrum $s(l)$,

Equation 3.5

$$s(l) = (40 \times exp^{\frac{-(l-300)*(l-300)}{100000}}) + \left(100 \times exp^{\frac{-(l-100) \times (l-100)}{50}}\right)$$

$$+ \left(200 \times exp^{\frac{-(l-500) \times (l-500)}{100}}\right)$$

$$+ \left(150 \times exp^{\frac{-(l-470) \times (l-470)}{100}}\right) + \left(130 \times exp^{\frac{-(l-440) \times (l-440)}{100}}\right)$$

where the first term is the baseline, $b(l)$, and the remainder of the equation are simulated

Raman peaks, is the same simulation that was used in the literature to evaluate existing

methods[48].
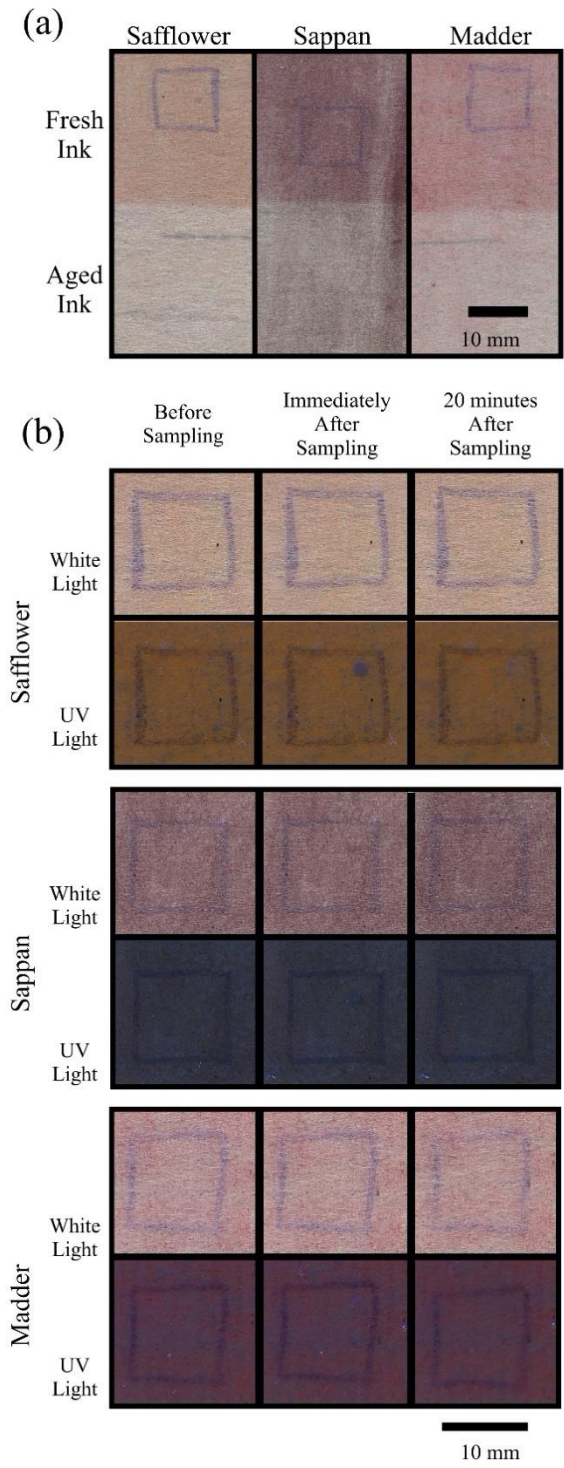
Figure 3.9: (a) White light images of reference prints (top) without and (bottom) with UV-B exposure. The blue squares are drawn on mylar placed beneath the print to note the sampling location during demonstration. (b) White light and UV light illuminated details of reference prints before and after micro-sampling.
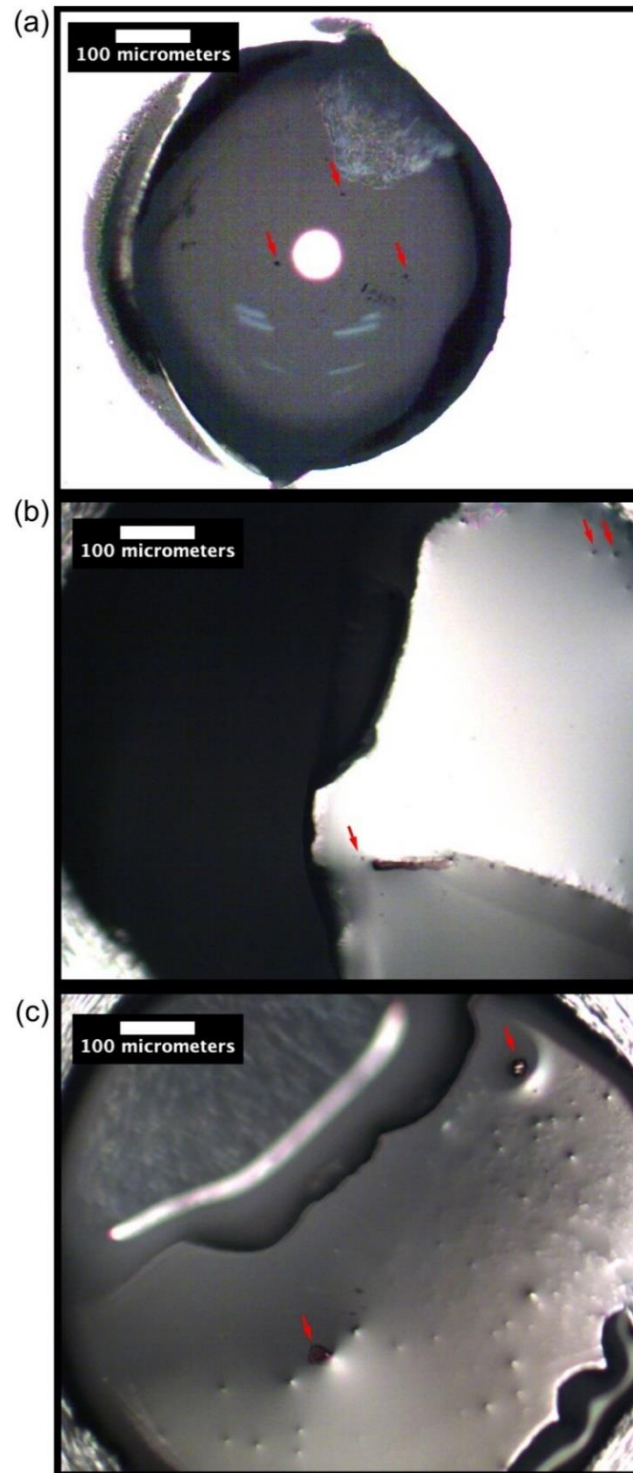
Figure 3.10: Raman microscope images (10× magnification) of hydrogels after sampling and before addition of AgNPs from (a) safflower, (b) sappan, and (c) madder reference prints. Images (a) and (b) have been brightened to better visualize particulate at the gel surface; red arrows indicate examples of colorant particles.
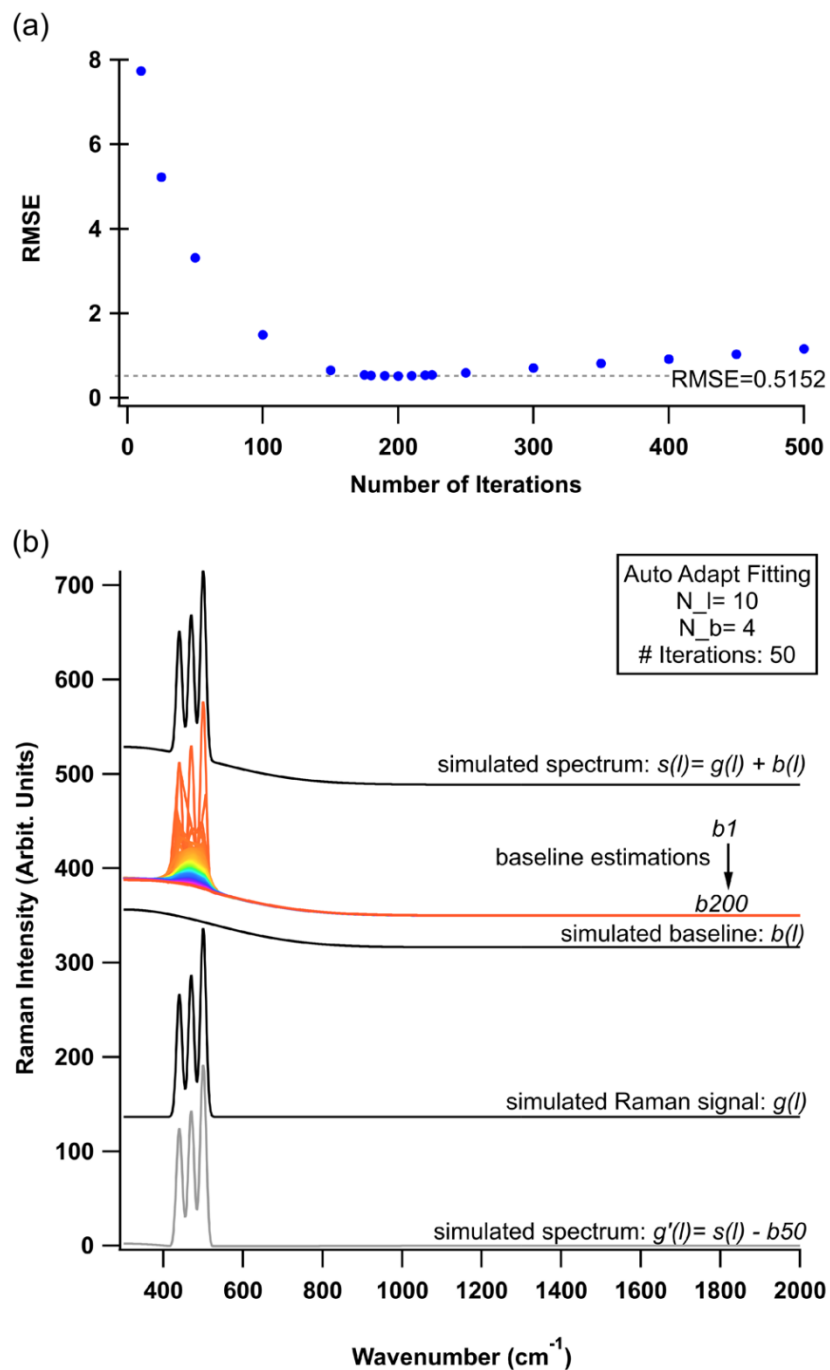
Figure 3.11: (a) Plot of RMSE values of fitted baseline versus number of iterations. The RMSE reached a minimum at 200 iterations, with the RMSE value denoted by the dashed line.(b) Plot showing (top-to-bottom) the simulated spectrum (s(l)) estimated baselines over 200 iterations, the actual baseline (b(l)), the simulated Raman signal (g(l)), and the baseline corrected spectrum (g′(l)).

3.7 Appendix B: Investigation of utility of Fiber Optic Reflectance Spectroscopy for identification of red organic colorants

Fiber optic reflectance spectroscopy (FORS) is a common method in conservation science, as it is fast, simple, non-invasive, and non-destructive. Conservation scientists have used FORS for identification of red organic colorants based on their unique optical properties. As the chromophores fade over time, though, their optical properties change. The difference in aging and fading of each chromophore also means that one colorant may be detectable longer than another. This work was intended to evaluate the capabilities of the Ocean Optics HDX spectrometer to detect unique chromophore signal from colorant mixtures in the best cases, where the colorants were still saturated in color.

Figure 3.12: Image of overprinted colorant areas for FORS analysis. (clockwise from top center) madder, madder + sappan, sappan, sappan + safflower, safflower, madder + safflower.

3.7.1 Methods

3.7.1.1 Samples

Single-colorant colorants were prepared by suspending solid colorant in animal hide glue, with water added dropwise to the desired consistency. These colorants were then painted onto unsized kōzo and allowed to fully dry. For overprinted areas, the second colorant (in a colorant) was printed over the previously dried colorant area. The sample prints are shown in **Figure 3.12**. The safflower colorant was noticeably less saturated than madder and sappan.

3.7.1.2 Instrumentation

Reflectance spectra were collected with an Ocean Optics HDX spectrometer, an HL-2000-HP-FHSA 20W light source, and a three-legged fiber optic cable. Spectra were collected for 25 ms and 500 spectra were averaged; including time between starting the save file and finished collection, total exposure time was approximately 30 s per print. Spectra were smoothed using a Savitsky-Golay smoothing process with span of 51 points.

First derivatives were calculated for each spectrum. Minima were identified from the reflectance spectrum, and inflection points were identified from the derivative plots.

3.7.2 Results

Reflectance spectra of single-colorant colorants and overprinting of two colorants are show in **Figure 3.13**. The reflectance spectra of reference colorants showed moderate correlation to the literature for prints on paper[8]. The observed spectral markers as compared to the literature are shown in **Table 3.3**. The collected madder spectrum showed a
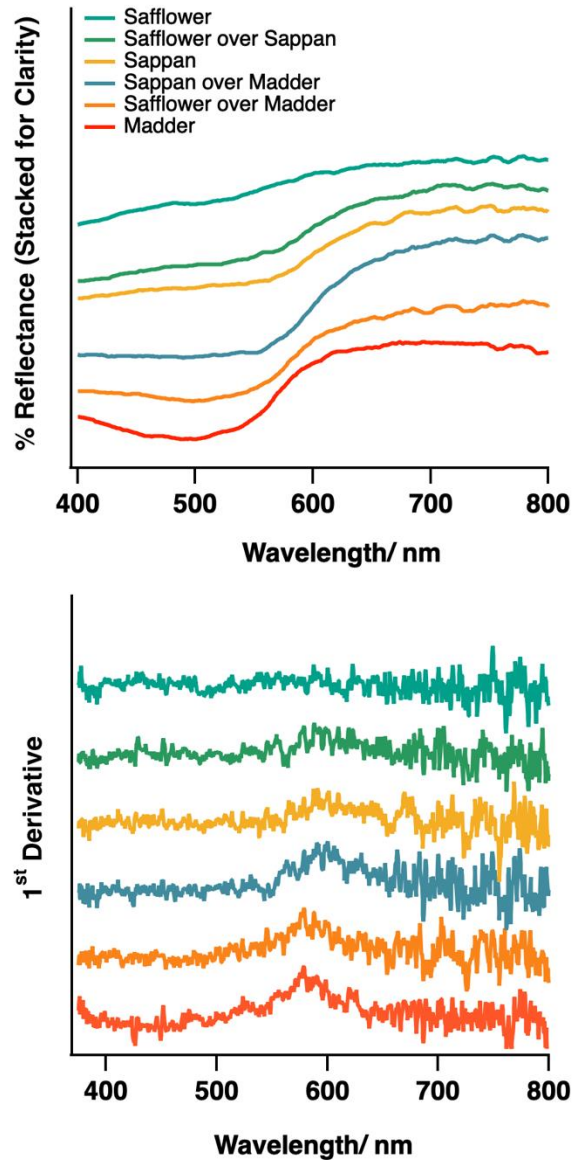
Figure 3.13: (top) FORS spectra of single-colorant inks and overprinting of two colorants. (bottom) First derivative plots for the spectra above.

minimum at 512 nm and an inflection point at 579 nm, whereas the literature reports only minima at 510 and 525 nm. The safflower spectrum had no observed markers. The sappan spectrum had a minimum at 562, a 28 nm red shift from the reported minimum. There was also an observed inflection for sappan at 588 nm, only 4 nm blue shifted from reported inflections for fresh dye.

Table 3.3: Literature versus observed reflectance spectral markers for single-chromophore colorants and overprinting of two colorants. The superscript [a]denotes a minimum (absorption) and [i]denotes an inflection point.

Reference Ink	Literature Markers[8, 61]	Observed Markers
madder only	510[a], 525[a]	512[a], 579[i]
safflower only	530[a]	none
sappan only	530[a], 592[i] (fresh), 601[i] (aged)	562[a], 588[i]
madder + safflower	510[a], 525[a], 530[a]	498[a], 579[i]
madder + sappan	510[a], 525[a], 530[a]	551[a], 600[i]
sappan + safflower	530[a]	568[a]

The spectrum of madder overprinted with safflower had an observed minimum at 498 nm and an inflection point at 579 nm—these are consistent with the madder-only reference. The spectrum showed no markers for safflower.

The spectrum of madder overprinted with sappan had a minimum at 551 nm and an inflection at 600 nm. These are most closely aligned with the results of sappan only, though surprisingly the minimum was blue shifted with respect to both madder and sappan.

Finally, the sappan overprinted with safflower showed only a minimum at 568 nm, consistent with the sappan-only reference and again showing no markers for safflower.

These results indicate that desaturated colorants (i.e., safflower) do not provide sufficient signal for FORS identification. Additionally, it was observed that even with good color saturation, if one colorant dominated the appearance in a mixture (e.g., madder overprinted with sappan), only the dominant color was identified by FORS.

Chapter 4: Reference data set and characterization of Japanese print materials by Surface-Enhanced Raman Spectroscopy and documentation of non-damage

This chapter represents a manuscript in preparation with the following authors:

Lyndsay N. Kissell, Trine K. Quady, and Tami L. Clare.

Keywords

Safflower, madder, sappan, SERS

Abstract

This dataset was collected to provide thorough characterization of red organic colorants (safflower, sappan, and madder) and binding medium (animal hide glue) used in *ukiyo-e* prints. The colorants were extracted from the raw plant materials; binder and *kōzo* paper were acquired from reliable sources. Reference materials were also mixed to form colorant and those colorants were artificially aged by UV-B exposure. All materials were measured by surface-enhanced Raman spectroscopic (SERS) analysis to fully characterize the inherently variable SERS response.

Table 4.1: Specifications table for data contained herein

Subject	Chemistry
Specific subject area	Analytical Chemistry, Surface enhanced Raman spectroscopy, Conservation Science
Type of data	Tables Figures
How the data were acquired	SERS spectra were acquired using a Horiba LabRam HR Evolution (Kyoto, Japan) equipped with 100×100 cm motorized stage and motorized z-axis control, 633 nm Laser Melles Griot (CVI, Albuquerque, New Mexico), and 600 lines/mm grating. Spectra were collected and saved from LabSpec6 software. SERS spectra were collected with 50× objective, 600 lines/mm dispersion grating and 300 µm confocal hole. Laser power, acquistion times, and accumulations were optimized on a case-by-case basis as determined by the live-feed Raman signal.
Data format	Raw Processed Analyzed
Description of data collection	Reference spectra of pure colorants were collected from bulk material mounted onto glass microscope slides. Test colorants printed on *kōzo* paper were collected using hydrogel-assisted micro-sampling and SERS measurements were collected from the gel surface. In all cases silver nanoparticles were drop-cast over the sample and solvent allowed to evaporate/absorb before collecting measurements.
Data source location	• Portland State University • Portland, OR • United States
Data accessibility	All raw data provided in .zip folder as text files
Related research article	L. Kissell, T. Quady, T.L. Clare *Optimized micro-sampling and computational analysis for SERS identification of red organic colorants, Spectrochim. Acta Part A.* Submitted.

4.1 Value of the data

- Optimization of silver nanoparticle synthesis for use as SERS substrates using a

  simple synthetic procedure is widely useful for those utilizing SERS

- These data represent a full SERS characterization of the organic red colorants, safflower, madder, and sappan and binding media, hide glue.

- Conservation scientists and Analytical Chemists studying these dyes can utilize the compilation of data from cited previous studies and this work.

- These data can be used as reference spectra for other studies using similar SERS substrates, and for comparison of SERS response of these materials to other SERS substrates.

- Photo documentation of the SERS sampling methodology by micro-stamping and DART MS characterization of the paper post-sampling (as described in the connected publication), builds confidence that the methodology is non-damaging

4.2 Data description

These data were collected in support of the studies published elsewhere[1].

4.2.1 Silver Nanoparticle Characterization

The published syntheses[2, 3] resulted in significant variation in product. Therefore, methods were modified to be performed in a single flask with either N_2 (Ag^N) or O_2 (Ag^O) sparging; seeding was also performed under sparging ($Ag^{N,seed}$, $Ag^{O,seed}$) to analyze the effect of introducing nucleation sites. The absorbance spectra for these syntheses are presented in **Figure 4.1**a. All λ_{max} and FWHM values are compiled in **Table 4.2**. The observed red shift of λ_{max} in both seeded syntheses confirms that seeding the reaction flask generates larger NPs, as the growth is nucleated at the surface of the existing nanostructures. Seeding also provides better control of the monodispersity, as evidenced

59

by narrower FWHM values. In all cases, Ag NPs synthesized under a controlled atmosphere produced a more uniform product than those synthesized on an open benchtop.
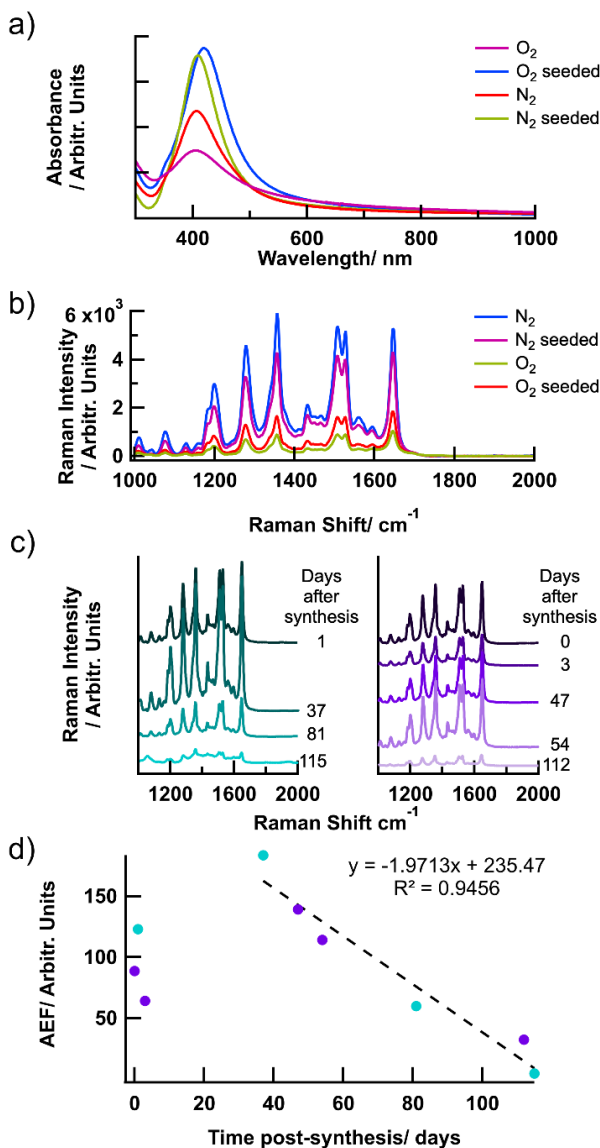
Figure 4.1: (a) Absorbance spectra of Ag NPs. (b) Maximum SERS enhancement of Rhodamine B in the presence of Ag NPs. (c) SER spectra of Rhodamine B in the presence of two different syntheses of Ag NPs with N2 sparging over more than 100 days post-synthesis. (d) Plot of enhancement vs. time post-synthesis, showing Ag NPs have maximum enhancement 40 days post synthesis with decreased enhancement over the subsequent 70 days.

Table 4.2: UV-vis absorbance and SERS enhancement results of Ag NPs according to published methods and under these experimental conditions.

Ag NP Synthesis	λ_{max}	FWHM	AEF (St. Dev)
Test Tube 1	402	125	---
Test Tube 2	407	110	---
Test Tube 3	412	98	---
Test Tube 4	415	92	---
Test Tube 5	400	118	---
Beaker	415	140	---
N_2 sparged	406	100	139.5 (40.7)
O_2 sparged	400	142	35.2 (21.1)
N_2 sparged, seeded	408	82	87.3 (40.4)
O_2 sparged, seeded	417	101	47.4 (7.2)

Figure 4.1b shows the SER spectra for the four types of Ag NPs at their peak analytical enhancement factors (AEFs). The AEF of Ag^N was the highest, followed by $Ag^{N,seed}$ and $Ag^{O,seed}$; the AEF for Ag^O showed poor enhancement. Therefore, Ag^N was the optimal synthetic method for producing AgNPs for SERS.

The stability of the Ag^N was studied over a longer period of analysis, by producing fresh Rhodamine B standards in the presence of the Ag NPs over more than 100 days. The measurements are presented in Figure 4.1c and d. The AEF of the particles increased in the 40 days after synthesis, but then began to decrease. By approximately 100 days post-synthesis, the AEF reached levels that were no longer sufficient for SERS applications. It is hypothesized that aggregation occurred over the first 40 days and once that process stabilized, enhancement effects also stabilized. From these results, it was concluded that optimal SERS enhancement is maintained from 35 to 100 days post synthesis and nanoparticles should not be used more than 120 days post-synthesis as their enhancement is greatly reduced after this timepoint.

4.2.2 Reference Materials Characterization

The spectra in Figure 4.2 were produced by baseline correction (described in [1]), normalization to max intensity, and averaging the relevant spectra.
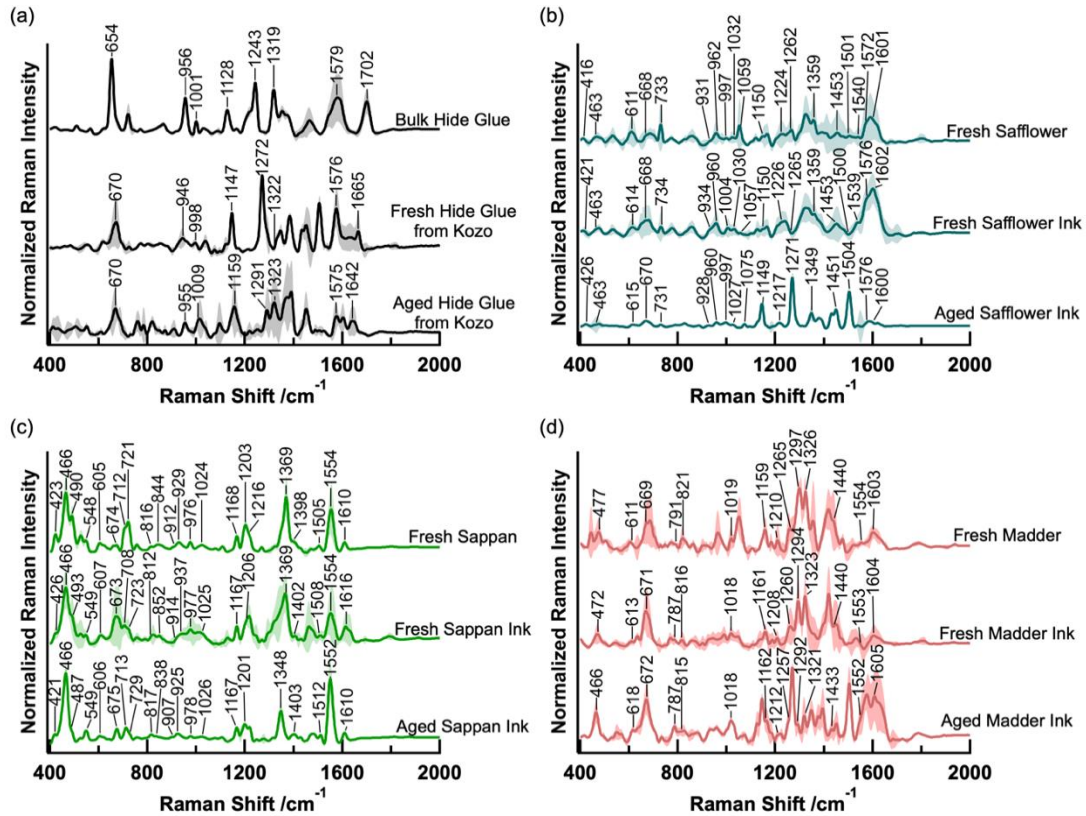
Figure 4.2: SERS spectra of (a) cow hide glue, (b) safflower, (c) sappan, and (d) madder. Shown are the average spectra of the (top) fresh material, (middle) the freshly prepared ink printed on *kōzo*, and (bottom) the ink after UV-B aging. Shaded regions represent the standard deviation of the normalized intensity at each point in the spectra.

4.2.2.1 Hide Glue

Previous spectroscopic analyses of collagen fibrils were executed on thin films[4, 5]. Because the bulk state of collagen affects the secondary and tertiary structures of the

protein, and thus, the spectroscopic properties, analysis in a comparable matrix was essential.

Figure 4.2a shows average SERS spectra of mammalian hide glue as bulk material, as a thin film printed on *kōzo*, and the thin film after artificial aging. Eight SER spectra of the hide glue standard were collected. Three were bulk glue measured on a microscope slide, three were sampled from *kōzo* paper using the hydrogel apparatus. Two spectra were sampled from *kōzo* paper after accelerated aging. One, a "control" area of the printed region, was protected from UV light, but still subjected to the thermal changes within the QUV device; the remaining spectrum was collected after exposure to combined thermal and UV-B aging. The spectra from each category were averaged and the representative average spectra are shown in Figure 4.2a. The spectra of bulk glue and fresh glue sampled from *kōzo* were quite uniform, with most variance arising from 1400-1700 cm^{-1}. The spectra of aged glues, on the other hand, were quite dissimilar, as shown by the variance throughout the spectrum. Peak analysis is compiled in Table 4.3.

The locations of peaks observed in the bulk glue spectrum at 654, 1128, 1243, 1319, and 1519 cm^{-1} shifted to higher energy in the spectra of hide glue sampled from *kōzo*. The spectrum of glue sampled from *kōzo* also shows narrower, more intense peaks.

After UV aging, peaks at 998, 1147, and 1272 cm^{-1} underwent shifts of 11, 12 and 19 cm^{-1} to higher energy, respectively; the peak at 1665 cm^{-1} shifted to lower energy. While these significant changes were observed with accelerated aging, the conditions of exposure were intentionally more extreme (60°C, unmitigated UV irradiation) than would be experienced by prints displayed indoors; such spectral data enabled the observation of the most dramatic changes possible.

Table 4.3: Average experimental Raman shifts for bulk hide glue, glue printed on *kōzo* , and aged glue on *kōzo* compared to average literature values and previously published vibrational assignments.

Raman Shift (cm⁻¹)[a]				Assignments[b,c]
fresh bulk hide glue	fresh hide glue on kōzo	aged hide glue on kōzo	Literature[c,d]	
Avg (St.Dev)	Avg (St.Dev)	Avg (St.Dev)	Avg (St.Dev)	Vibrational Mode
417 w		412 (3) w		
423 (3) vw,sh	427 vw	433 w		
		454 sh		
471 vw	461 (0) vw	474 sh		
	485 (1) w	490 (3) sh		
509 (1) w		507 (9) w		
	543 sh	534 vw		
	555 (1) w	552 (3) w		
566 (2) w		573 vw		
		598 vw	600 (3)	
624 (3) w,sh	618 (1) w	612 w		
		637 sh		
654 (1) vs		645 sh		
676 sh	670 (4) m	670 (4) s	665	δ_w (COO⁻)
	697 sh	690 (3) sh		
		708 w		
721 (2) m	724 w	730 vw	739	v(C-S) cysteine/ trans and gauche
741 vw				
772 w	773 (2) w	760 (4) m		δ_w (N-H)
	803 (7) w	786 m	791 (7)	
		820 (4) m	814 (1)	v(C-C)
	838 vw	831 sh		
851 sh	851 w	848 (2) w	854 (3)	Tyrosine
866 (2) w	861 vw	870 (4) w		
	883 vw			
		910 (2) w	919 (1)	C-C vibration
956 (1) s	946 (1) m,br 7	955 (1) m	934 (9)	
		978 sh		
1001 (1) w	998 (1) w	1009 (7) m	1003 (1)	phenylalanine ring breathing
1032 (2) w	1038 m	1030 sh	1031 (4)	phenylanlanine
1047 vw,sh	1048 sh	1040 sh		
	1076 w			
1093 w		1097 m	1092	v(C-C), v(C-N)
1128 (1) m	1147 (1) s	1153 (10) s	1122	
1167 (3) w			1163 (7)	v_{asym}(CH₃ aliphatic); δ_r (CH₂, aromatic)
		1175 sh		
		1194 vw		

		1210 vw	1208 (5)	phenylalanine/tyrosine
1221 (0) sh		1215 (7) w		
1243 (1) s		1252 (8) w	1243 (6)	amide III
	1272 (1) vs	1268 vw		
	1287 sh	1290 (3) m	1285	
1319 (1) s	1322 (15) sh	1323 (2) m	1316 (3)	CH$_2$ deformation
1354 (1) m,sh	1347 (1) m	1360 sh		
1369 (0) sh		1374 sh	1367 (17)	
1381 sh	1385 (1) s	1391 (3) s	1411 (11)	
	1435 (1) m,sh	1433 sh		
1463 m	1452 (4) m	1454 (3) s	1447 (2)	δ(CH-H)
1468 sh		1484 (9) w		
	1506 (1) s	1509 vw		
1549 (5) sh	1537 vw	1530 (4) w	1554 (5)	
1579 (5) s,br	1576 (1) s	1575 (4) m	1585	tryptophan
1590 sh		1606 (5) m	1603 (1)	phenylalanine/tyrosine
	1637 (6) w,br			
1702 (1) s	1665 (1) w	1642 (4) m	1665 (2)	amide I

[a]vs-very strong, s-strong, m-medium, w-weak, vw-very weak, sh-shoulder, br-broad

[b] ν-stretching, δ - in plane bending, γ-out-of-plane bending, τ-torsion, δ_w-wagging, δ_{tw}-twisting, δ_r-rocking

[c]previously reported assignments from references 4 and 5.

[d]averages and standard deviations calculated from previously published studies; peak intensities not reported

4.2.2.2 Safflower

The average spectra of safflower colorant before and after aging are compared to the standard spectrum of safflower colorant in Figure 4.2b. Exact peak locations for each spectrum are annotated in Figure 4.2b and listed in Table 4.4.

In the standard spectrum, the peaks at 1322 and 1453 cm^{-1} have been attributed to vibrational modes in the chalcone or glucose moieties; signals at 962, 1032, and 1244 cm^{-1} arise from vibrations in the linkage between the two chalcone moieties in carthamin[6]. Some signals indicate the presence of other chalcone impurities—such as degradation products and hydroxysafflor A, the primary colorant in safflower yellow. These are present at 416, 488, 1359, and 1501 cm^{-1} and have all been previously identified in safflower yellow[7].

Mixing safflower with hide glue to produce a colorant resulted in the presence of several prominent peaks attributed to the glue binder, which often overlap with those of carthamin. However, the Amide I band peak from the protein backbone of hide glue at *ca.* 1700 cm^{-1} shows the presence of binder in the measurements.

After UV aging, the spectrum of safflower colorant largely correlates to the average spectrum of fresh hide glue printed on *kōzo* . Most notably, the peaks attributed to the linkage between chalcone moieties (962, 1032, and 1244 cm^{-1}; Fig. 2a) decreased or were not present. Indicating that with UV light exposure, the large carthamin molecule fragments into smaller chalcone or chalcone-like fragments. Fragmentation is also seen by the presence of the peak at 1349 cm^{-1}, as well as the continued presence of a signal at 426 cm^{-1}, both attributed to hydroxysafflor A and other chalcone degradation products.

Table 4.4: Average experimental Raman shifts for fresh safflower, fresh safflower colorant, and aged safflower colorant compared to average literature values and previously published vibrational assignments.

Raman Shift (cm^{-1})[a]				Assignments[b,c]
fresh safflower	fresh safflower colorant	aged safflower colorant	Literature[c,d]	
Avg (St.Dev)	Avg (St.Dev)	Avg (St.Dev)	Avg (St.Dev)	Vibrational Mode
416 (3) w	421 (10) w	426 (5) w	425 vw	
454 (1) vw	447 (5) sh			
463 (2) w	463 (3) sh	463 (2) w		
488 (6) sh	476 (4) w	477 w	473 w	
	505 (6) vw	505 vw	491 vw	
516 (3) sh	523 (8) sh	528 vw		
533 (2) w	534 (3) w			
544 (4) sh	545 (5) sh		546 w	
562 (5) vw	565 (8) sh			
601 sh	606 (2) sh			
611 (1) m	614 (5) w	615 (2) w		
631 (0) sh	632 (4) vw	631 sh		
647 (7) vw	650 (6) sh		640 m	
668 (3) sh	668 (2) m,sh	670 (1) m		
677 w	677 (1) m	678 sh		
	682 (1) sh			
689 (2) w	690 (4) sh	685 sh		
706 (7) sh	703 (5) sh			
733 (5) s	734 (3) w	731 (1) w	732 (2) vw	$\gamma_{I,II}$(ring)/ γ(C7,8H)
			746 vw	$\gamma_{I,II}$(ring)/ γ(CC9C)
	762 (4) sh			
	777 (3) w		775 (1) w, vw	γ_{II}(ring)/ γ(CC9C)/γ(C7,8H)
	786 (1) sh	790 (1) vw		
	804 vw	801 vw	803 vw	
850 (2) w	852 (2) sh	848 vw		
863 (1) sh	862 (4) w		863 (3) vw	δ_I(ring)
879 (3) sh	884 sh	887 (2) w		
913 vw	916 (5) vw		907 w	
931 (2) sh	934 (6) w,sh	928 (2) w	938 w	
948 sh	950 (3) w			
962 (5) m	960 (3) m	960 (1) w	958 w	δ(C=C33--C)/ ν(CC12C)/ δ(O26,27H)/ δ(C=C8--C)
982 (3) vw	979 (0) vw		982 (5) vw	γ(C33H)/ ν(C12-C16)
997 (4) w	1004 (4) w	997 (2) w		
1018 (6) sh	1020 (4) vw			
1032 (5) w	1030 (3) w	1027 (2) w,sh	1041 vw	γ(C33H)/ ν_{III}(C-C)/ δ_{II} (OH)
1059 (1) s 0	1057 (12) vw	1075 (1) w	1071 DFT	ν(C31-O)/ δ_{III}(CH)/ δ_{III}(OH)
1098 sh	1099 (5) w	1094 vw	1096 DFT	ν(C8-C9)/ ν_{II}(C-C)/ ν(C31-O)/ ν(C16-C17)
1119 (5) w	1115 (6) sh			
1130 vw	1128 (1) w	1131 (1) sh		ν_{II}(C-C)/ δ(O27H)
1150 (8) m	1150 (8) w	1149 (7) s	1145 DFT	ν_{II}(C-C)/δ(O27H)

			1162 (4) sh, m	phenyl -OH (C-O stretching?) [2]; δI(CH)/ δ(O22H)
1167 (2) m	1170 (2) w	1167 sh	1169 (0) s	δI(CH)/ δ(C7,8H)
	1183 (3) vw	1189 w	1194 DFT	
1205 (5) sh	1207 (1) sh		1215 (3) Sh	δ(C33H)/ δII(OH)
1224 (4) sh	1226 (6) m,sh	1217 (3) m	1239 Vw	δtw(CH2)/ δIII(OH)/ δIII(CH)
1244 (2) sh	1246 (6) m	1238 sh	1256 vw	δ(C33H)/ ν(CCC15C)/δ(O25H)
1262 (6) m	1265 (7) vw	1271 (1) vs	1278 (1) m	phenyl -OH [2]; δI(CH)/ δ(C7,8H)/ δII(OH)
1281 (2) vw	1282 (5) sh		1295 (1) m)	δI(CH)/ δ(C7,8H)
1304 (8) sh	1305 (4) sh			
1322 (0) s	1320 (3) s,br		1324 (4) vw, s	phenyl -OH; δIII(CH)/ δIII(OH)
1332 (3) sh	1329 (3) sh			
1344 (6) sh	1341 (2) sh	1349 (1) s	1348 vs	
1359 (3) s	1359 (5) s,sh		1363 m	phenyl -OH (stretching)
1390 w	1382 (7) sh	1380 (1) m	1389 sh	ν(C=C14-C)/ δ(C33H)/ δ(O26H)
1399 (3) w	1401 (3) vw		1399 vw	δw (CH2)/ δIII(OH)/ δIII(CH)
1410 (2) sh	1417 (4) vw		1409 (4) m	δIII(OH)/ δw(CH2)
	1435 (5) sh	1433 (2) s,sh	1443 sh	νI(ring)/ ν(C7=C8)/ δ(O22H)
1453 (5) m	1453 (3) m	1451 (1) s	1460 (4) m	ring vibrations; δsc(CH2)/ δ(O30,32H)/ δ(C19,20H)
1481 sh	1484 (3) sh		1482 m	ring vibrations; δsc(CH2)
1501 (3) w	1500 (4) vw	1504 (2) vs	1504 vs	νI(ring)
1513 sh	1514 sh		1510 sh	ν(C14=C33)
1540 (1) w 2	1539 (11) m,sh	1539 (4) w	1548 sh	
			1573 vs	ring vibrations
1572 (2) sh	1576 (6) sh	1576 (1) m 1	1578 (1) sh	νI,II(ring)/ ν(C7=C8)/ ν(C9=O)
1589 s	1590 (2) sh		1583 (0) sh	νI(ring)/ ν(C7=C8)/ ν(C9=O)
1601 (4) sh	1602 (4) vs	1600 sh	1600 (3) s	ν(C=O); conjugated C=C; νI(ring)/ ν(C7=C8)/ ν(C9=O)
1618 (5) sh	1618 (6) sh	1622 w	1619 (4) s, sh	νII(ring)/ ν(C=O)
1650 sh	1642 (7) sh		1658 sh	
1670 (8) w	1667 (4) vw			
	1694 (6) w			

[a]vs-very strong, s-strong, m-medium, w-weak, vw-very weak, sh-shoulder, br-broad, DFT-calculated by DFT

[b] ν-stretching, δ - in plane bending, γ-out-of-plane bending, τ-torsion, $δ_w$-wagging, $δ_{tw}$-twisting, $δ_r$-rocking

[c]previously reported analyses from references 6 and 7.

[d]averages and standard deviations calculated from previously published studies

4.2.2.3 Sappan

Studies of brazilein, the color contributing compound of sappan, have analyzed the strong impacts of pH and heat on the color of the molecule due to deprotonation and/or degradation[8]. While extreme color changes are known (and were, in fact, used to produce varying shades of red colorant commercially[9]), spectroscopic studies of brazilin and brazilein from sappan agree on peak locations in FT-Raman and SER spectra; the intensities of those peaks vary likely due to the previously studied protonation states of brazilein. The average spectra of sappan colorant before and after aging are compared to the average spectrum of sappan colorant in Figure 4.2c. Exact peak locations for each spectrum are annotated in Figure 4.2c and listed in Table 4.5.

In the sappan standard, some wood cellulose, holocellulose and lignin remained in the colorant (due to the extraction process), giving rise to peaks at 548 and 1109 cm^{-1}.[10, 11] Previous spectroscopic studies suggest the peaks at 528, 1216, 1369, and 1554 cm^{-1} arise from brazilein; the peak at 1369 cm^{-1} arises from the C=C(=O)-C=C segment of brazilein, the sole unique functionality in the oxidized molecule. In the presented standards, this peak is very strong, however in the literature, it has been observed primarily as a shoulder to the medium-strong peak between 1320 and 1350 cm^{-1}.[10, 12]

The visible color of the colorant faded greatly during aging, as depicted in Figure 3.9; the spectral response, however, showed similarities to the fresh sappan standards. Of note is the increased relative intensity of the peak at 1348 cm^{-1} with a slight shoulder at 1362 cm^{-1}. In agreement with the literature, this suggests a higher relative ratio of brazilin with some brazilein still present in the aged sample. The presence of brazilein is further supported by a strong peak at 1552 cm^{-1}. On the low energy end of the spectrum, the cluster

69

of five peaks (in the lab-extracted standard, ranging from 425-549 cm^{-1}) degraded to a strong peak at 466 cm^{-1} with shoulders at 421 and 487 cm^{-1}. The prominence of peaks at 421 and 466 cm^{-1} correspond to brazilin and occur at slightly lower energy than the analogous bending vibrations from brazilein. The presence of these peaks, with only a small contribution from brazilein (487, 526 cm^{-1}), suggests that during UV exposure the conjugated system is disrupted—perhaps forming a quinone intermediate, or other degradation product structurally more similar to brazilin, as suggested in recently published work[8].

Table 4.5: Average experimental Raman shifts for fresh sappan, fresh sappan colorant, and aged sappan colorant compared to average literature values and previously published vibrational assignments.

Raman Shift (cm⁻¹)[a]				Assignments[b,c]	
fresh sappan	fresh sappan colorant	aged sappan colorant	Literature[c,d]		
Avg (St.Dev)	Avg (St.Dev)	Avg (St.Dev)	Avg (St.Dev)	Brazilin	Brazilein
423 (2) m,sh	426 (3) m,sh	421 (1) m,sh	419 (4) vw,sh	δ(ring)/ δ(CO)	
	443 sh		443 (1) w		δ(ring)/ δ(CO)
466 (1) vs	466 (2) vs	466 (1) vs	470 (3) vw,s	δ(ring)	
490 (3) s,sh	493 (0) sh	487 (1) sh	490 (3) vw		δ(ring)
			501 vw	δ(ring)	
528 (1) m,sh	526 (2) w	526 sh	530 (1) w		δ(ring)
548 (3) sh	550 (2) w	549 (2) w	549 (2) vw	δ(ring); holocellulose	
605 (3) w	608 (4) w	606 (1) w	599		
622 (1) sh	618 vw	619 (1) vw	616		
	641 (2) vw		642 (1) vw		γ(CH)
660 (1) sh	656 (3) sh				
674 (2) w	673 (2) m	675 (1) m	677 (9) vw	γ(CH)/ δ(CC=O)/ δ(CC-O)	
			705		
712 (6) m,sh	708 (4) sh	713 (1) m	717		
721 (2) s	723 (5) sh	729 (2) sh	730 (2) m,w	γ(CO)/ γ(CH); δ(C−H)	
757 (1) w	759 (3) w		753		
			765 (2) w	γ(CO)/ γ(CH); δ(C−H)	
	792 (1) vw		792 vw	γ(CO)/ γ(CH)	
816 (1) vw	812 (2) w	817 (1) w			
844 (4) w	851 (6) w	838 (2) vw			
912 (2) sh	914 (6) vw	907 (6) vw	900		
929 (3) w	935 (7) w	925 (1) w	929 (1) vw 6	δ ᵣ CH₂)	
976 (1) w	977 (4) w	978 (3) vw	977 (1) w 3		
	1007 (6) w		1002 m	ν(C−C)/ ν(C−O)	
1024 (2) w	1026 (4) sh	1026 (6) w	1031 (3) vw, m		ring stretching
	1052 vw		1045 m		
			1088 (8)	δ(CH) wood cellulose	
1109 (2) w			1115 (3)	δ(CH) wood cellulose	
	1133 (8) w		1134 vs		
			1145	δ(C−H)	
1168 (2) m	1167 (2) m	1167 (1) m	1167 (5) m	δ(CCH)/ ν(C-C) [6]; δ(C−H)/ δ(C−C)	
			1189 s		

71

1203 (2) m	1204 (4) sh	1201 (4) m	1204 (6) vw,s	δ(C−C)	
1216 (3) sh	1218 (4) s	1219 (2) sh	1225 (5) m,sh		ν(C−O)/ ν(C−C)
	1236 (0) sh				
	1247 (2) sh		1255 (5) vw,s h	ν(C−O)/ ν(C−C)/ δ(CH₂)	
1270 (1) w	1275 (5) vw	1278 w	1277 (5) sh		
1308 vw	1305 (10) sh		1307 vs		
1322 (4) sh	1321 (3) sh		1320 (3) m	ν(C-O)/ δ(O-CC)/ δ(CH₂); ν(C–C)/ ν(C = O) composed of syringyl and guaiacylligin modes	
1349 sh	1345 (2) sh	1348 (1) s	1347 (6) m,s	ν(C−O)/ δ(OCC)/ δ(CH2)	
1353 (1) sh	1359 (4) sh	1362 sh			
1369 (2) vs	1371 (5) vs		1369 (4) sh	ν(C=C(=O)-C=C)	
1398 (4) sh	1402 (8) w	1403 (1) m	1395 (2) sh,s, br		
1429	1425 (8) vw	1430 w	1432 (5) m,s	ν(C=C)/ δ(ring)/ δ(COH)	
			1449 (2) m	ν(C=C)/ δ(ring)/ δ(COH)	
	1457 sh		1460 w		
1469 (2) w	1469 (4) m	1474 (1) sh	1479		
	1483 (3) sh	1485 w	1491		
1505 (1) w	1509 (5) w	1512 (0) w	1505 (4) vw, m		
	1530 sh		1525 w	ν(C=C)	
1554 (2) s	1543 (1) s	1552 (1) vs	1551 (4) vs		
			1567 (3) s		ν(C=C)
	1576 sh		1578		
			1600 (2) vs	ν(C-C), lignin aromatic ring	
1610 (1) w	1612 (10) m	1610 (1) w	1611 (2) w,vs	ν(C=C)	ν(C=O)/ ν(C=C)
1639 vw	1632 (2) sh				
			1660		
	1693 w		1697 w		ν(C=O)/ ν(C=C)

[a]vs-very strong, s-strong, m-medium, w-weak, vw-very weak, sh-shoulder, br-broad

[b] ν-stretching, δ - in plane bending, γ-out-of-plane bending, τ-torsion, δ_w-wagging, δ_{tw}-twisting, δ_r-rocking

[c]previously reported analyses from references 7, 10, 11, and 12.

[d]averages and standard deviations calculated from previously published studies

4.3.2.4 Madder

Anthraquinones, specifically alizarin and purpurin, are known to experience large enhancement effects by SERS and have been well characterized in the literature[7, 13-20]. Therefore, the purpose of this analysis was to verify the spectral patterns and investigate the effects of both binding medium and UV-aging on spectral interpretation. Average spectra of madder colorant before and after UV aging are compared to the average spectrum of fresh madder colorant in Figure 4.2d. The reported peak locations can be found in Figure 4.2d and Table 4.6.

For the fresh colorant, the enhancement of the anthraquinone-based colorant was substantial and agreed with published spectra. After UV-aging the madder colorant spectrum closely resembled fresh hide glue—possibly due to the degradation of the anthraquinones. Despite significant changes in the spectrum, some madder peaks remained at 466, 787, 1018, 1321, and 1605 cm^{-1}.

Table 4.6: Average experimental Raman shifts for fresh madder, fresh madder colorant, and aged madder colorant compared to average literature values and previously published vibrational assignments.

Raman Shift (cm^{-1})[a]				Vibrational Modes[b,c]	
fresh madder	fresh madder colorant	aged madder colorant	Literature[c,d]		
Avg (St.Dev)	Avg (St.Dev)	Avg (St.Dev)	Avg (St.Dev)	alizarin	purpurin
			402 (2)	skeletal vibrations	
			422 (5) vw,w,m	skeletal vibrations	
444 m	450 sh		455 (7) sh	skeletal vibrations	
477 (3) m	472 (8) m	466 (1) s	478 (3) m,vs	skeletal vibrations	
505 (7) w	498 (10) sh	496 w,sh	503 (8) w,s	skeletal vibrations	
521 vw	545 (9) w	543 (9) m		skeletal vibrations	
	562 vw	566 (3) sh	554 (6) vw,w	skeletal vibrations	
579 vw	577 (3) vw		581 (3) m	skeletal vibrations	
600 sh	600 (1) sh		606 (3)	skeletal vibrations	
611 (2) w	613 (2) w	618 (3) sh			
636 sh	634 (1) w	632 m,sh	629 (7) m	skeletal vibrations	
			646 (5) w	skeletal vibrations	
669 3) m,sh	671 (6) s	672 (1) s	663 (3) w,m	γ(C=O)/ δ(CCC)	
686 (1) m	684 (3) sh	689 sh	681 (4) m,s	γ(C=O)/ γ(C−O)	
707 sh	700 (4) vw	703 (6) sh			
730 (5) vw	724 vw	733 w	729 (7) vw	δ(CCC)	
748 vw	748 vw				
770 (5) w	772 (4) w	772 vw	765 (9) w,m	γ(C−H)/ γ(C=O)/ τ(CCCC)	
791 (8) sh	787 (4) w	787 (2) w			
821 (3) w	816 (4) w	815 (13) vw	818 (5) vw,w	ν(CC)	
834 (6) sh		828 w	831 (6) vw,w	γ(C−H)/ γ(C−O)	
861 (6) w	858 (5) w	860 w	866 (1) vw	δ(C=O)/ δ(CCC)	
903 w	903 (2) vw		903 (4) vw,m	γ(C−H)	
918 vw	923 (0) vw				
931 sh	932 (0) w	932 (3) w	928 (4) m		
943 sh	945 (4) w	946 sh			
963 m	963 (2) vw	959 (1) w	955 (6) m		

980 (3) sh	979 (4) w	972 sh	973 (4) m	ν(CC)/ δ(CCC)	
1019 (0) m,sh	1018 (1) w	1018 (2) m	1016 (3) vw,m		
	1026 (3) sh	1030 (2) sh	1029 (2) vw,w	ν(CC)/ δ(CH)	
1048 (4) s	1047 (5) w		1046 (4) w,s	δ(CCC)	
	1063 (2) sh	1062 w,sh	1068 (6) m,s		
	1098 vw		1094 (6) m,vs		
	1112 (1) vw				
	1132 (2) w,sh	1127 (1) m,sh	1127 (4)		
1143 sh	1140 sh	1146 (1) s			
1159 (5) m	1161 (7) m	1162 (4) m,sh	1158 (5) m	ν(CC)/ ν(CH)	
1186 (5) m	1189 (3) w	1179 w,sh	1188 (3)	ν(CC)/ δ(CH)/ δ(CCC)	
1210 (2) w	1208 (1) w	1212 (5) w	1213 (4) m	δ(CH)/ δ(CCC)	
	1232 (1) vw	1226 (1) w	1237 (3) sh		
1265 (9) m,sh	1260 (3) sh	1257 (2) sh			
	1275 sh	1270 (1) vs	1271 (4) m,sh	ν(CO)/ ν(CC)	
1297 (1) vs	1294 (3) vs	1292 (8) sh	1292 (6) s,vs	ν(CO)/ ν(CC)/ δ(CCC)	
1306 sh	1308 (1) vw				
1326 (3) vs	1323 (3) vs	1321 (2) m	1322 (4) m,s,vs	ν(CC)	
	1349 (8) sh	1349 (1) m	1337 (7)		
1357 m,sh	1361 (3) sh		1367 (4)	ν(CC)/ δ(COH)	ν(CC)/ δ(COH)
1408 sh	1400 (4) sh	1394 (2) m	1400 (9) w,s	ν(CC)/ δ(CH)	
1421 (6) s,br	1420 (3) vs	1415 vw	1426 (6) w,m,sh		
1440 (2) sh	1440 (5) sh	1433 (2) w			
	1454 (2) m,sh	1451 (2) w	1449 (3) s,vs	ν(CC)/ δ(COH)/ δ(CH)	
			1461 (4) sh		
1475 (4) w,sh	1477 (6) sh	1481 vw	1475 (3) s	ν(CO)/ ν(CC)/ δ(CH)	
1518 w	1512 (4) vs	1504 (0) vs	1504 (7) vw	ν(CC)	
1534 (7) w	1534 (3) w				
1554 (4) w	1553 (6) sh	1552 (10) sh	1553 (4) w,s	ν(CC)	ν(CC)
			1567 (6) sh	ν(CC)	
1575 (2) vs	1587 sh	1575 (4) s,br	1584 (6)		
1603 (6) m	1604 (3) w	1605 (1) s	1603 (5) w	ν(CC)	ν(CC)
1618 sh	1623 (5) sh	1622 (3) sh	1623 (5) w,m	ν(C=O)	ν(C=O)
1642 sh	1634 (1) sh	1636 (2) Sh			
1652 sh	1665 (11) W		1651 (6) Sh	ν(C=O)/ δ(CCC)	

[a]vs-very strong, s-strong, m-medium, w-weak, vw-very weak, sh-shoulder, br-broad
[b] ν-stretching, δ - in plane bending, γ-out-of-plane bending, τ-torsion, δ_w-wagging, δ_{tw}-twisting, δ_r-rocking
[c]previously reported analyses from references 7, 10, 13, 16, 17, and 19
[d]averages and standard deviations calculated from previously published studies

4.3 Experimental design, materials and methods

4.3.1 Materials

Sodium borohydride, silver nitrate, hydroxylamine hydrochloride, and potassium hydroxide were purchased from Millipore-Sigma (St. Louis, MO). Sodium hydroxide was purchased from Thermo-Fisher (Waltham, MA).

Madder root (*Rubia tinctorum)* sourced from Pakistan was purchased from Mountain Rose Herbs (Eugene, OR). Brazilwood (*Caesalpinia echinata)* sourced from Brazil was purchased from Gilmer Wood Company (Portland, OR). sappanwood (*Biancaea sappan)* and safflower petals (*Carthamus tinctorius*), both sourced from China, were purchased from e-Bay (seller: Chineseherbworks, Henrico, VA) and Etsy (seller: Atman Tea Company, Glendale, CA), respectively. A sample of cowhide glue (*Kyojo Nikawa)* was received from Nikawa Labs *via* the Portland Art Museum. *Kōzo* paper was purchased from Hiromi Paper Company (Culver City, CA).

4.3.2 Ag NP synthesis and Raman analysis

Silver nitrate solution was prepared to a concentration of 1.00×10^{-4} M. A solution of hydroxylamine hydrochloride was prepared to a concentration of 1.497×10^{-4} M in 3.33×10^{-4} M sodium hydroxide. All solutions were prepared immediately before synthesis. To synthesize nanoparticles, 90 mL of the hydroxylamine solution and 10 mL of $AgNO_3$ were mixed under appropriate conditions—either in an open top beaker with stirring [2], in test tubes (10 mL hydroxylamine solution: 1 mL $AgNO_3$) [3], or in round bottom flasks with stirring under N_2 or O_2 sparging. After mixing, the solutions were allowed to react for 5 minutes. Aliquots of 1 mL were then centrifuged at 5000 rpm for 5 minutes at 4 °C in an Eppendorf 5430R centrifuge with FA-45-30-11 rotor. After centrifugation, 950 µL of

supernatant were removed and 50 µL of fresh deionized water was added to the remaining

pellet. Concentrated AgNP solutions were stored in the dark at 4 °C. Ultraviolet-visible

absorbance spectra of the AgNP solutions were collected with 1 nm steps on an Agilent

8953 diode array spectrophotometer (Santa Clara, CA).

Rhodamine B solutions (14.5 µM) were prepared in plastic cuvettes with 100 µL of

concentrated Ag NP colloid, capped and sealed for analysis. SER spectra were collected

using 50× objective, 600 lines/mm dispersion grating and 25% ND filter with 300 µm

confocal hole, 15 s acquisition, 30 accumulations, and a range of 1000-2000 cm^{-1}.

Analytical enhancement factors (AEF) for Rhodamine B (14.5 µM) were calculated as a

function of the signal-to-noise ratio,

Equation 4.1
$$AEF = \frac{SNR_{SERS}}{SNR_{Raman}}$$

where SNR is the signal-to-noise ratio of the peak at 1646 cm^{-1} from either the SERS or

regular Raman spectrum. Signal was calculated by subtraction of the baseline intensity

from the peak intensity; the noise was calculated in a region with no signal and is defined

as the difference between the maximum and minimum intensities divided by 5, to reflect a

99.4% confidence interval.

4.3.3 Hide Glue Preparation

Cow hide glue was used in this work, as a representative mammalian analog to deer

hide glue. A small piece of cowhide glue (approximately 2 cm length) was combined with

15 mL of deionized water and warmed on low heat until dissolved. Once dissolved,

evaporated water was replaced to 15 mL and the solution was allowed to cool to room

temperature. The final product was stored in a glass vial covered with aluminum foil at

4ºC. When cooled, the solution solidified to a gel which was used, and will be referred to, as the hide glue standard.

4.3.4 Safflower Extraction

Safflower *(C. tinctorius)* petals (50 g) were wrapped in a cheesecloth pouch and placed in a beaker containing one liter of deionized water. The petals were allowed to soak for thirty minutes to extract Safflower yellow dye. The yellow solution was disposed of and this procedure was repeated until the soaking solution was nearly clear.

Once the yellow dye was removed, the cheesecloth pouch was placed, open, over a large beaker and 5 g K_2CO_3 (dissolved in 25 mL deionized water) was poured over the petals. An additional 975 mL of deionized water was carefully poured over the petals to rinse the red dye out. The resultant solution was pale orange.

After thoroughly rinsing the petals, citric acid solution (1 M) was added to the solution to precipitate the red dye. The precipitate was allowed to settle overnight and was vacuum filtered to collect the solids. The collected solid was dried overnight in an oven set to 70 °C. Dried solids were ground with a mortar and pestle and stored in a glass vial for later analysis.

4.3.5 Sappan Extraction

Heartwood of *C. sappan* was ground into fine sawdust and 10 g was placed in one of three beakers. In one beaker, colorant was extracted using 500 mL of 0.06 M NaOH; in the second beaker wood chips were covered with 500 mL of deionized water; in the third beaker, wood chips were covered with 500 mL of 0.013 M aluminum potassium sulfate solution. Each solution was boiled for three hours, then allowed to cool overnight.

The three extracted solutions were combined (filtered through tightly woven cotton) to produce a deep red-purple cloudy solution. The precipitate was filtered over vacuum. The collected solid was dried on filter paper in a 60ºC oven until the solid was cracked and pulling away from the paper. The solid was then collected and ground with a mortar and pestle to a fine powder. The final product was stored in a glass vial at room temperature, in the dark, for further use.

4.3.6 Madder Extraction

Roots of *R. tinctorum* were soaked overnight in an excess of water. The cloudy red solution was drained and replaced with a similar volume of fresh water. This process was repeated until the water was clear and light pink, at which point the final rinse was drained, and the water replaced. This bath was heated to and maintained at 50 to 65°C for 6-10 hours, then allowed to cool overnight with a loose covering. Heating was monitored carefully, and did not exceed 65°C, to prevent degradation of the alizarin molecules.

On the second day of heating, alum (dissolved in warm water, 3 g per 10 g plant material) was added to the dye bath and heating was resumed. After heating, the roots were separated from the solution by straining through tightly woven cotton. The solution was gravity filtered to remove remaining large particles and the filtered solution was again heated to 50-65°C. Potassium hydroxide (dissolved in water, 0.8 g per 10 g plant material) was slowly added to the hot solution to form the lake—some foaming was observed, and a precipitate was immediately formed. When foaming stopped, the solution was removed from heat and allowed to cool to room temperature.

After cooling, the pale yellow-orange aqueous layer was decanted, replaced with fresh water, and precipitate was again allowed to settle. This process was repeated until the

79

aqueous layer remained colorless. The precipitate was collected via vacuum filtration and the collected solids were dried on weigh paper in a 50°C oven. The dried product was finely ground with a mortar and pestle and stored at room temperature for later use.

4.3.7 Sample Preparation and Collection

For bulk material measurements, a small amount of solid colorant product (as described in sections 3.4.3-3.4.6) was placed on a glass microscope slide. Silver nanoparticles (AgNPs) were dropcast over the solid, and SERS measurements were collected.

For printed colorant samples, the solid dyes were suspended in animal hide glue, adding deionized water drop-wise to produce the desired consistency of colorant. These colorants were mixed using a glass muller to disperse the colorant as evenly as possible, and the produced colorants were printed onto *kōzo* paper. After drying overnight, hydrogel-assisted micro-sampling (as described in the connected publication[1]) was performed to collect micron-scale colorant particles. AgNPs (2 µL) were dropcast directly onto the hydrogel where the samples were collected, and SERS measurements were collected.

For aged colorant samples, the printed *kōzo* papers underwent artificial aging under UV-B irradiation in a Q-Labs QUV chamber. The aged colorants were then sampled as previously described and SERS measurements were collected.

4.4 References

1.   Kissell, L. N.; Quady, T. K.; Clare, T. L., Optimized micro-sampling and computational analysis for SERS identification of red organic colorants. *Spectrochim. Acta Part A* (Submitted).
2.   Leopold, N.; Lendl, B., A New Method for Fast Preparation of Highly Surface-Enhanced Raman Scattering (SERS) Active Silver Colloids at Room Temperature by Reduction of Silver Nitrate with Hydroxylamine Hydrochloride. *J. Phys. Chem. B* **2003,** *107* (24), 5723-5727.
3.   Sessa, C.; Weiss, R.; Niessner, R.; Ivleva, N. P.; Stege, H., Towards a Surface Enhanced Raman Scattering (SERS) spectra database for synthetic organic colourants in cultural heritage. The effect of using different metal substrates on the spectra. *Microchem. J.* **2018,** *138*, 209-225.
4.   Gullekson, C.; Lucas, L.; Hewitt, K.; Kreplak, L., Surface-sensitive Raman spectroscopy of collagen I fibrils. *Biophys J* **2011,** *100* (7), 1837-45.
5.   Nevin, A.; Osticioli, I.; Anglos, D.; Burnstock, A.; Cather, S.; Castellucci, E., Raman Spectra of Proteinaceous Materials Used in Paintings: A Multivariate Analytical Approach for Classification and Identification. *Anal. Chem.* **2007,** *79* (16), 6143-6151.
6.   Cañamares, M. V.; Mieites-Alonso, M. G.; Leona, M., Fourier transform-Raman and surface-enhanced Raman spectroscopy analysis of safflower red-dyed washi paper: pH study and bands assignment. *J. Raman Spectrosc.* **2020**.
7.   Bruni, S.; Guglielmi, V.; Pozzi, F., Historical organic dyes: a surface-enhanced Raman scattering (SERS) spectral database on Ag Lee–Meisel colloids aggregated by NaClO4. *J. Raman Spectrosc.* **2011,** *42* (6), 1267-1281.
8.   Ngamwonglumlert, L.; Devahastin, S.; Chiewchan, N.; Raghavan, G. S. V., Color and molecular structure alterations of brazilein extracted from Caesalpinia sappan L. under different pH and heating conditions. *Sci Rep* **2020,** *10* (1), 12386.
9.   Vitorino, T.; Melo, M. J.; Carlyle, L.; Otero, V., New insights into brazilwood lake pigments manufacture through the use of historically accurate reconstructions. *Studies in Conservation* **2016,** *61* (5), 255-273.
10.   Whitney, A. V.; Van Duyne, R. P.; Casadio, F., An innovative surface-enhanced Raman spectroscopy (SERS) method for the identification of six historical red lakes and dyestuffs. *J. Raman Spectrosc.* **2006,** *37* (10), 993-1002.
11.   Edwards, H. G. M.; de Oliveira, L. F. C.; Nesbitt, M., Fourier-transform Raman characterization of brazilwood trees and substitutes. *Analyst* **2003,** *128* (1), 82-87.
12.   de Oliveira, L. F. C.; Edwards, H. G. M.; Velozo, E. S.; Nesbitt, M., Vibrational spectroscopic study of brazilin and brazilein, the main constituents of brazilwood from Brazil. *Vib. Spectrosc.* **2002,** *28* (2), 243-249.
13.   Van Elslande, E.; Lecomte, S.; Le Hô, A. S., Micro-Raman spectroscopy (MRS) and surface-enhanced Raman scattering (SERS) on organic colourants in archaeological pigments. *J. Raman Spectrosc.* **2008,** *39* (8), 1001-1006.
14.   Leona, M.; Stenger, J.; Ferloni, E., Application of surface-enhanced Raman scattering techniques to the ultrasensitive identification of natural dyes in works of art. *J. Raman Spectrosc.* **2006,** *37* (10), 981-992.

15.   Pozzi, F.; Lombardi, J. R.; Bruni, S.; Leona, M., Sample treatment considerations in the analysis of organic colorants by surface-enhanced Raman scattering. *Anal Chem* **2012,** *84* (8), 3751-7.

16.   Murcia-Mascarós, S.; Domingo, C.; Sanchez-Cortes, S.; Canamares, M.; Garcia-Ramos, J., Spectroscopic identification of alizarin in a mixture of organic red dyes by incorporation in Zr-Ormosil. *J. Raman Spectrosc.* **2005,** *36* (5), 420-426.

17.   Baran, A.; Wrzosek, B.; Bukowska, J.; Proniewicz, L.; Baranska, M., Analysis of alizarin by surface-enhanced and FT-Raman spectroscopy. *J. Raman Spectrosc.* **2009,** *40* (4), 436-441.

18.   Shadi, I. T.; Chowdhry, B. Z.; Snowden, M. J.; Withnall, R., Semi-quantitative analysis of alizarin and purpurin by surface-enhanced resonance Raman spectroscopy (SERRS) using silver colloids. *J. Raman Spectrosc.* **2004,** *35* (8-9), 800-807.

19.   Canamares, M.; Garcia-Ramos, J.; Domingo, C.; Sanchez-Cortes, S., Surface-enhanced Raman scattering study of the adsorption of the anthraquinone pigment alizarin on Ag nanoparticles. *J. Raman Spectrosc.* **2004,** *35* (11), 921-927.

20.   Amato, F.; Micciche', C.; Cannas, M.; Gelardi, F. M.; Pignataro, B.; Li Vigni, M.; Agnello, S., Ag nanoparticles agargel nanocomposites for SERS detection of cultural heritage interest pigments. *The European Physical Journal Plus* **2018,** *133* (2), 74.

Chapter 5: A multi-analytical approach to identify red colorants on woodblock prints attributed to Suzuki Harunobu

This chapter represents a manuscript in preparation with the following authors:

Lyndsay N. Kissell, Trine K. Quady, Samantha Springer, Jeannie Kenmotsu, and Tami L. Clare.

Abstract

Red organic colorant identification is an important topic for conservation of Japanese *ukiyo-e* prints. Of particular interest are the works of Suzuki Harunobu, who was working at the inception of full-color printmaking. These prints were made on delicate *kōzo* paper and colored with thin layers of colorant, which are difficult to sample. This study used imaging analysis, x-ray fluorescence (XRF), Raman, and surface-enhanced Raman (SERS) to identify the red colorants on a collection of Harunobu prints in the collection of the Portland Art Museum. Through image analysis (visible, UV, and IR illuminations), 23 prints were categorized by appearance. XRF results provided identification of vermilion and ochre colorants, and identified color fields that contained lead. Raman analysis lead to the identification of red lead, and SERS analysis identified both safflower and madder colorants. This work is expected to contribute to the body of knowledge regarding the red colorant palette in use in the late eighteenth century, as full-color printmaking took off.

5.1 Introduction

Edo-period Japanese woodblock prints are widely recognized for their richly decorated scenes, evocative color application, and technically skillful production. During

the Edo period (1603-1867) the practice of color woodblock printmaking evolved from two- and three-color images to full-color brocade (*nishiki-e*) prints. These brocade prints were popularized in part by the prolific artist Suzuki Harunobu (c. 1725?-1770). Harunobu drew inspiration from classical literature, poetic conceits, and scenes of everyday life in Edo, now Tokyo, often as a reimagining of well-known stories and/or accompanied by poems.

Woodblock prints were produced through a highly collaborative process utilizing the skills of master artisans, overseen by a publisher[1]. The image was designed by the artist (e.g., Harunobu), woodblocks were produced by carvers, and the final image was produced by printers. These prints were produced on *kōzo* paper often sized with *dōsa*, a mixture of animal hide glue and alum. Colorants mixed with hide glue were applied in thin layers that become tightly incorporated with the fibrous paper network. The color palette was extensive, and studies have suggested that colorants from the same color family were often mixed to achieve the desired tone.[2, 3]

Red colorants were relatively limited, deriving primarily from three inorganic (vermilion-mercuric sulfide, red lead-lead(II,IV) oxide, and ochre-mixed iron oxides) pigments and three organic (safflower, sappan, and madder) dye sources[4-6]. The color contributing compounds for safflower, sappan, and madder are carthamin, brazilin/brazilein, and alizarin/purpurin, respectively. Herein, "colorant" will refer to mixtures of pigment or dye with binder. The light sensitivity of the organic colorants is well-established in preservation literature [4, 7, 8] and their fugitive nature has prompted the modern implementation of strict exhibition lighting regimes to prolong their vibrancy.[9] Definitive identification of the organic colorants used on Japanese prints can inform

lighting recommendations and therefore positively impact their accessibility and long-term care.

Common non-destructive methods of colorant analysis include imaging under various sources of illumination (e.g., visible or ultraviolet light)[10, 11], x-ray fluorescence spectroscopy (XRF)[12, 13], fluorescence spectroscopy[3], and fiber optic reflectance spectroscopy (FORS)[10, 14-17]—these methods, however, provide incomplete information. Therefore, these techniques are best suited to multi-analytical studies. Raman spectroscopy provides more complete molecular information about the analyte by probing bond vibrations in the analyte molecule. Raman analysis, however, can be complicated by inherent fluorescence of an analyte. Therefore, surface-enhance Raman spectroscopy (SERS) has been used in the analysis of red organic dyes, which are often fluorescent.[18-23] One factor that limits analysis of organic colorants on Japanese prints is the difficulty of removing samples. The previously mentioned incorporation of colorants into the paper network makes sampling difficult without adversely affecting the object and its future examination, an important ethical practice in conservation.[24] The removal of material with a scalpel, an often-used sampling method for other object types, would undoubtedly impact the structural integrity of a sheet of paper. Therefore, minimally invasive sampling methodologies have been developed to enable access to analytical tools beyond the non-invasive instrumental techniques better attuned to characterizing inorganic pigments.[25, 26] The collection at the Portland Art Museum includes 32 prints designed by or attributed to the artist Suzuki Harunobu, the majority of those accessioned nearly a century ago[27]. Therefore, these prints have a long history of protective measures and regular condition reporting. The prints in the Portland Art Museum's collection consist of early calendar

prints, poetic collections (e.g., Eight Views), rare impressions, and some examples of the only known impression of an image. Identification of the colorants used on this collection will inform the conservation community on the printing practices employed in the earliest years of "full-color" woodblock printing (1765-1770)—a pivotal moment in the technical and aesthetic development of *nishiki-e*—and the technical use of color in the period prior to the introduction of other red colorant sources (e.g., cochineal, eosin)[12].

The work presented herein summarizes a survey of the Suzuki Harunobu prints at the Portland Art Museum with the objective of identifying the red colorants used and identifying patterns in color selection. These works were analyzed by non-invasive methods—imaging under various lighting conditions, stereomicroscopy, and XRF—and subsequently, seven prints were selected for minimally invasive sampling, wherein microscopic red colorant particulate was collected from the surface of the prints and analyzed by SERS. The SERS data were processed through a custom-built genetic algorithm (GA) equipped with a robust spectral library. The micro-sampling and SERS data analysis techniques have been evaluated and determined to be minimally invasive and do not permanently alter the work sampled; this evaluation is published elsewhere[25, 26]. Through thorough non- and minimally-invasive analysis, the palette of red colorants used on Harunobu's late works were definitively identified.

5.2 Results

The full results of this work are summarized in Table 5.1.
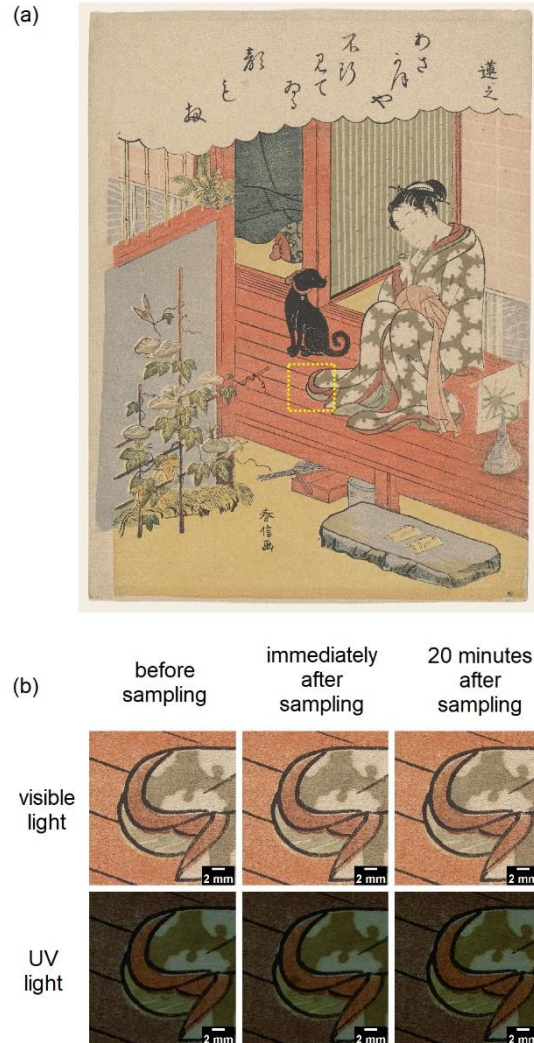
Figure 5.1: (a) *Renshi, from the series Fūryū goshiki-zumi (A Stylish Version of Five Colors of Ink)*, ca. 1768, color woodblock print with embossing on paper; *chūban nishiki-e*, image: 11 5/16 in x 8 5/16 in; sheet 11 3/8 in x 8 9/16 in, The Mary Andrews Ladd Collection. Portland Art Museum, Portland, Oregon, 32.71. (b) (DETAIL) Images of the area indicated by the yellow box in (a). (left-to-right) before, immediately after, and 20 minutes after micro-sampling. In the UV light images, a wet spot is visible in the center of the image, but after 20 minutes had dried, leaving the print visibly unchanged. Full Image citations are provided in the experimental section.

5.2.1 Effects of Micro-sampling on Papers

Photo-documentation was used to assess any visible effects of the hydrogel sampling process on the prints. Preliminary demonstrations on mock-up prints indicated that wetting from the water-equilibrated hydrogel may occur, but that the effect was short-lived.[25] A representative example is shown in Figure 5.1 along with magnified views of an area before and after micro-sampling. In Figure 5.1b a wet spot with an area of 1.7 ± 0.2 μm^2 is barely discernable by eye. After 20 minutes the wet spot was not visible under visible or UV light illumination.

5.2.2 Particle Size Analysis

Raman microscope images were collected of each hydrogel after sampling and the size distribution of collected particles was evaluated. The average particle sizes for each sample area are included in Table 5.1. Figure 5.2 shows an example of a microscope image and the subsequent processing for particle counting. The collected samples from the seven prints ranged from single grains of colorant to larger pieces of glue-bound colorant and
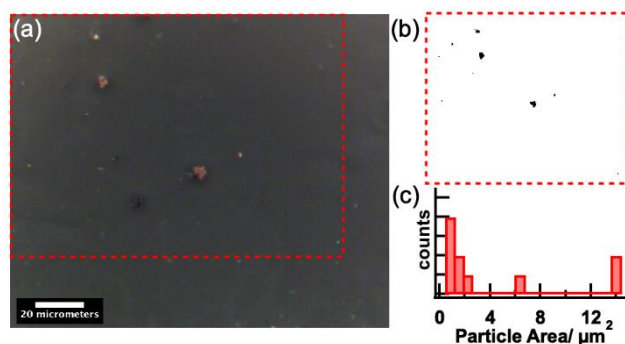
Figure 5.2: (a) 50× magnification image of hydrogel surface after micro-sampling with visible red particulate, (b) image mask showing identified particles, and (c) histogram showing particle size distribution. The red dashed box in (a) corresponds to the area shown in the image mask (b).

average particle sizes ranged from 2.60 to 36.97 µm, much smaller than can be sampled through standard scalpel or needle collection methods.

5.2.3 FTIR Analysis of Substrate

A single fiber that was raised from the surface and near the edge, was collected with a small scissor from *Ono no Komachi (32.75)* without detriment to the rest of the print.

The fiber was analyzed by FTIR to gain insight into the paper substrate and binding medium. The FTIR spectrum of the fiber is shown in Figure 5.3, along with relevant reference spectra[28, 29]. From 800-1500 cm^{-1} the spectrum is nearly identical to a reference spectrum of Ramie, a bast fiber in the same class as *kōzo*.[30] Differences arise in the region from 1500-1700 cm^{-1}, where the sample fiber has a weak peak at 1647 cm^{-1} and a small shoulder at 1540 cm^{-1}. These peaks correlate to the Amide I and Amide II peaks in animal hide glue[31], respectively. The collected fiber had a thin layer of red colorant on the surface, and because of the location on the print, was included in the red colorant analysis in Section 5.2.4.3.
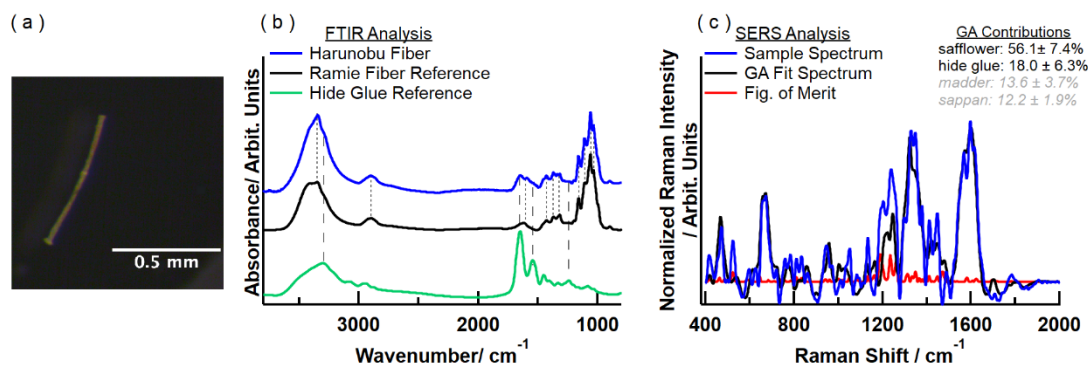
Figure 5.3: FTIR spectrum of a fiber collected from *Ono no Komachi* (32.75) compared to relevant reference spectra. Dashed lines indicate peaks corresponding to animal hide glue reference(shown, bottom spectrum), and the dotted lines indicate peaks likely arising from *kōzo* substrate (shown in comparison to Ramie, middle, another variety of bast fiber). Hide glue and Ramie reference spectra from the IRUG[28,29].

5.2.4 Colorant Identification

Red areas throughout the Harunobu prints in the collection were evaluated by non-invasive and non-destructive means. Based on their visual characterization, those reddish areas are grouped as, "opaque reds", "red-orange", "medium reds" and "pinks". Selected areas from the "red-orange", "medium red", and "pink" areas were micro-sampled for analysis by Raman and SERS using the previously described methods[25].

5.2.4.1 Opaque reds

Visual Analysis

Nine areas presented visually as deep red to red-brown with high opacity. Examples of neutral reds are present in only two prints. Examples of red-brown colors are present in six prints. Examples of these color fields are shown in Figure 5.9. Under UV light, these areas did not fluoresce, and under IRR imaging, only a slight absorption was observed.

XRF

XRF spectra of dark reds are shown in Figure 5.4a and b. The XRF results were complementary to the visual categorizations—deep reds were alike and red-brown areas were alike, but the two categories were elementally unique. Spectra of the deep red areas all showed evidence of mercury, indicating the presence of vermilion-based colorant.
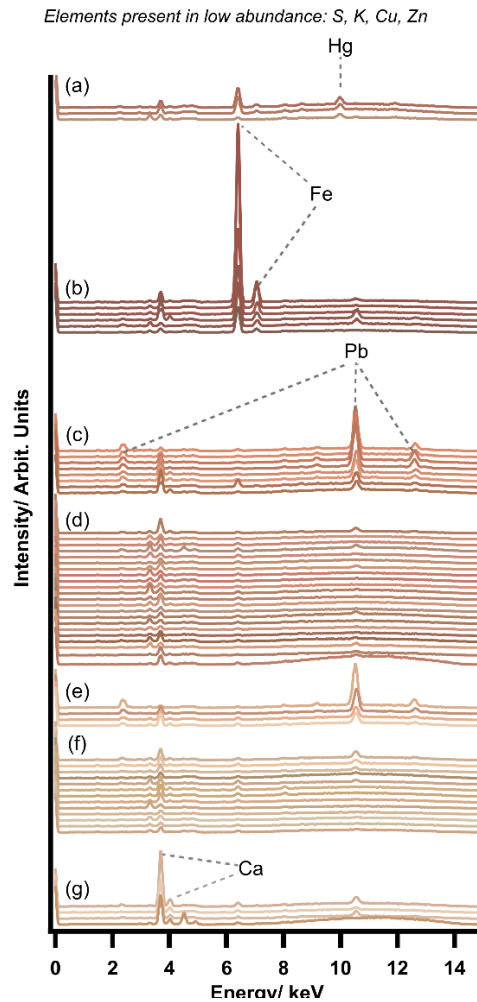
Figure 5.4: XRF spectra of red areas across the Harunobu collection at the Portland Art Museum. Spectra-line colors correspond to the measured RGB value of the area under white light illumination. Spectra are categorized by elements they contain: (a) mercury, (b) large amount of iron, (c) & (e) lead, (d) & (f) no identifying elements, and (g) larger than average intensity of calcium.

Spectra of the red-brown areas showed high intensity iron peaks suggesting that these areas were printed with ochre-based colorants.

5.2.4.2 Red-Orange

Visual Analysis

Eight areas across seven prints were visibly bright orange to orange-red. These areas showed no fluorescence under UV light. IRR images revealed minimal absorption of the pristine colorants, but areas of discoloration (blackening) are absorbing of IR light.

XRF

The XRF spectra for red-orange areas are shown in Figure 5.4c. The XRF analysis indicates that the colorants in these areas contain lead. This is not conclusive, however, due to the limitations of XRF; similar results would be observed in colorants that contain either red lead (Pb_3O_4) or lead white ($PbCO_3 \cdot Pb(OH)_2$). In addition to the presence of lead, above average calcium was present in the measurement of one area; nickel was identified in one area.

Raman and SERS

Of the eight red-orange areas, three were micro-sampled and analyzed by Raman spectroscopy. The resultant Raman spectra (shown in Figure 5.5) revealed that red lead was used in the colorants for these areas. SERS spectra and results of analysis by GA for these three samples are presented in Figure 5.6 The SERS analysis of the samples identified
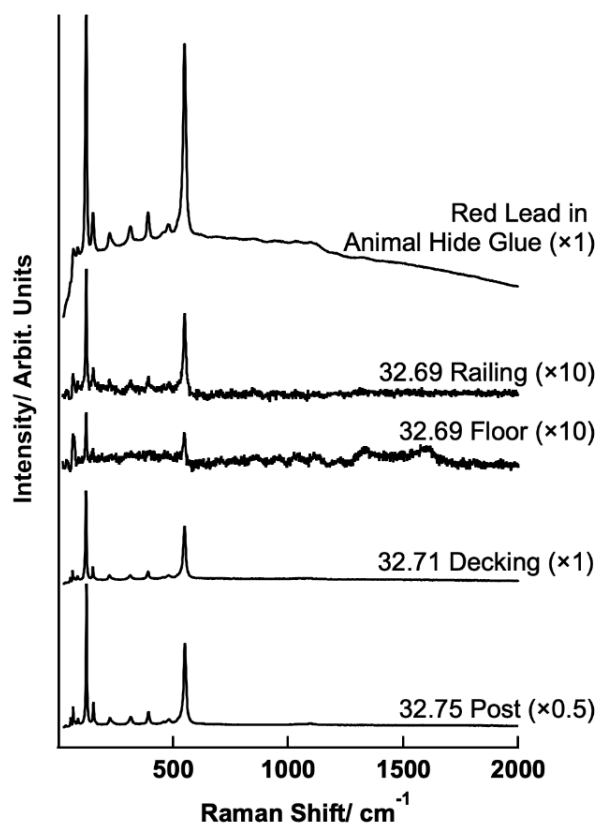
Figure 5.5: Regular Raman spectra of microsamples from red-orange areas that contain lead. All the sampled areas with deep color saturation were confirmed to contain red lead, Pb_3O_4, as compared to a reference spectrum (top).

similar colorant contributions—safflower and madder—in all cases. These data indicate

the red-orange colorants are complex mixtures of red lead with safflower and madder.
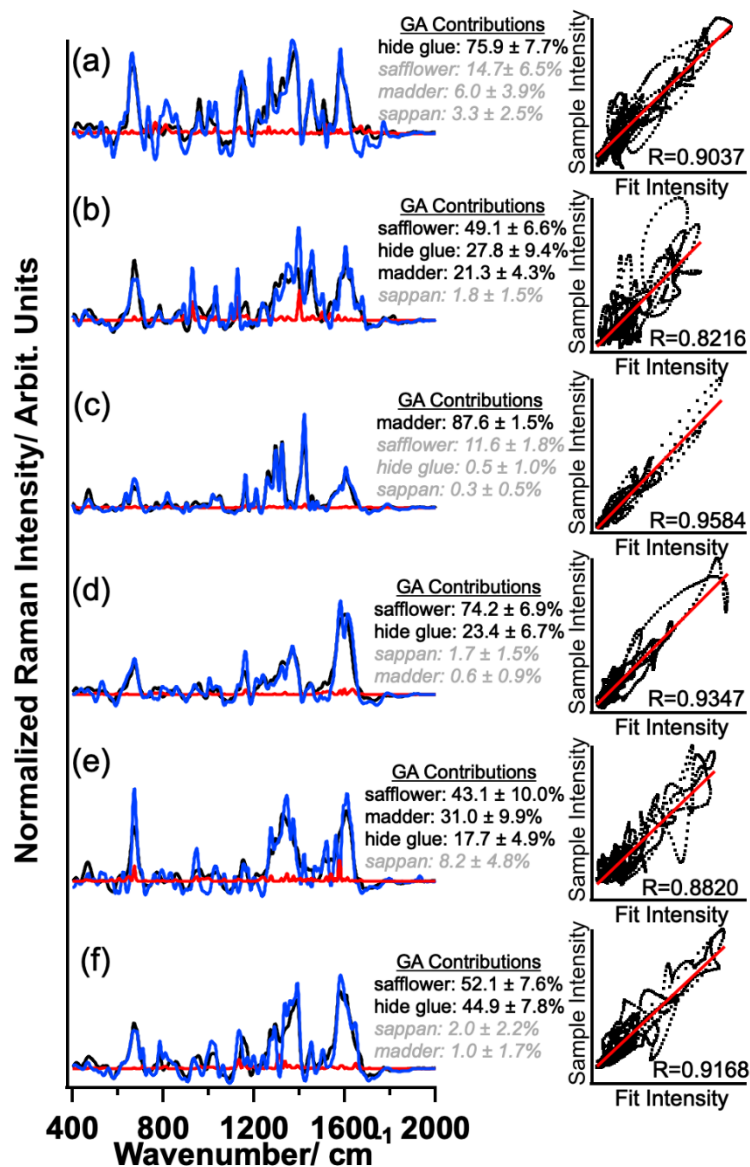
Figure 5.6: SERS spectra and corresponding GA fit results for red-orange colored areas. Spectra (a) and (b) are from red post on *Ono no Komachi* (32.75), spectra (c) and (d) are from the decking on *Renshi* (32.71), and spectra (e) and (f) are from the railings on *Koshikibu no Naishi* (32.69). Blue traces are the sample spectra, black traces are the fit spectra, and red traces are the squared difference. The inset plots to the right show the correlation between the sample and its fit spectrum.

5.2.4.3 Medium Reds

Visual Analysis

On 22 areas across 16 prints, color fields ranging from dark pink to red were identified, which are grouped together here as, "medium-reds". All areas but one were fluorescent under UV illumination. That area, though visually consistent with fluorescent reds under white light, absorbed UV light. An observation about this area is that it was printed with two different red colorants in close proximity. Six areas showed very slight absorption of IR light, making the colorant discernable from its surroundings in IRR images.

XRF

Shown in Figure 5.4d are spectra from medium-red areas. Of these 22 areas, two contained unique elements. One area contained manganese and one contained nickel.

Raman and SERS

Regular Raman analysis was inhibited by fluorescence of the collected micro-samples from these medium-red areas and did not aid in determining the colorant compositions. Representative SERS spectra for these samples are shown in Figure 5.7. The GA analysis identified both safflower and madder colorants, both alone and in mixtures.
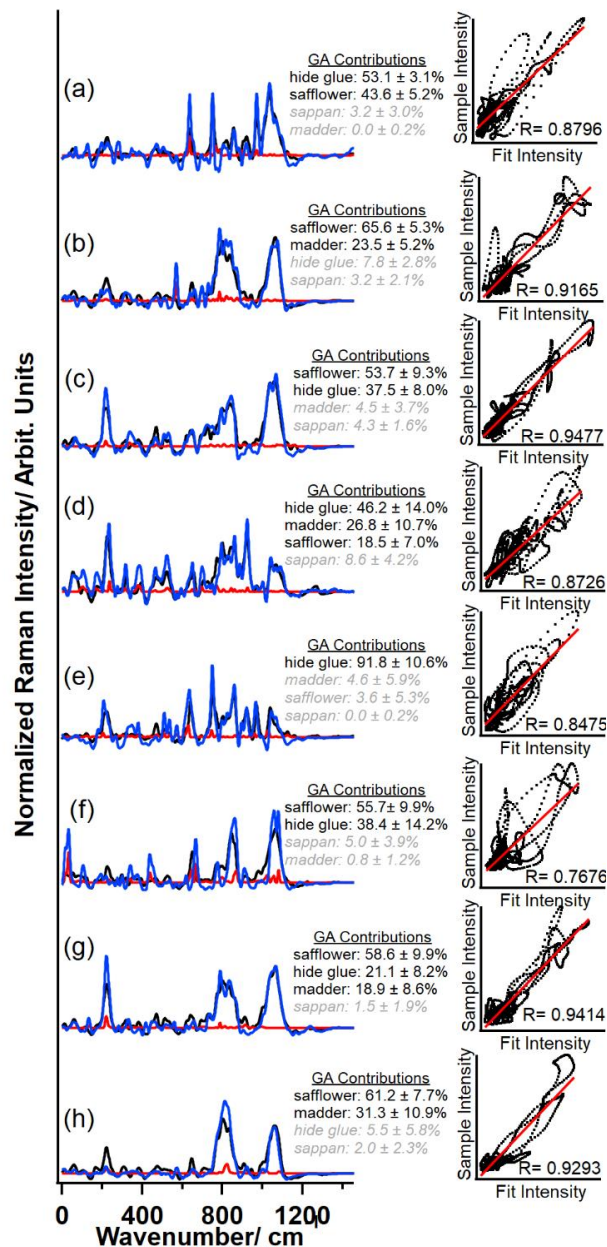
Figure 5.7: SERS spectra and corresponding GA fit results for medium red colored areas. Spectrum (a) is from the frond on *Kyōdai no shūgetsu (Autumn Moon of the Mirror)* (32.84), spectrum (b) is from the futon on *The Departure* (2016.18.1), spectra (c) from the futon on *Ono no Komachi* (32.75), spectrum (d) is from the kimono on *Ono no Komachi* (32.75), spectrum (e) is from the inner kimono on *Renshi* (32.71), spectrum (f) is from the orange *hakama* on *Koshikibu no Naishi* (32.69), and spectra (g) and (h) are from the brazier cup and body, respectively, on *Gi (Righteousness)* (35.39). Blue traces are the sample spectra, black traces are the fit spectra, and red traces are the squared difference. The inset plots to the right show the correlation between the sample and its fit spectrum.

96

5.2.4.4 Pinks

Visual Analysis

Twenty areas on thirteen prints appeared pale pink. Three areas displayed fluorescence. Eight areas were minimally fluorescent (ranging from pink to dusty rose in UV images). Nine areas were not fluorescent under UV illumination. The IRR images reveal one area that is more reflective of IR light than the paper and two areas that show black discoloration that is IR absorbing.

XRF

The XRF spectra for these areas are displayed in Figure 5.4e-g. Because potassium, calcium and sulfur were detected in most cases, they are only indicative of a colorant at very high levels (e.g, elevated calcium indicates a white calcium carbonate colorant). Four areas revealed detectable levels of lead (S/N greater than 10, shown in Figure 5.4e), though they were much less abundant than in the Red-Orange areas mentioned previously (Figure 5.4c). Most of the measured areas revealed no identifying elements (Figure 5.4f). One print had detectable levels of copper. Four light pink areas contained a higher-than-average level of calcium, as shown in Figure 5.4g.

Raman and SERS

The Raman analysis of one pink area identified red lead (shown in Figure 5.5). In other pink areas that showed evidence of lead in the XRF, the lead species were not identified by Raman. SERS results are shown in Figure 5.8. Of the four pink areas sampled, the SERS analysis of one resulted in no colorant identification. Two areas were determined to contain safflower. One area was determined to contain safflower and madder.
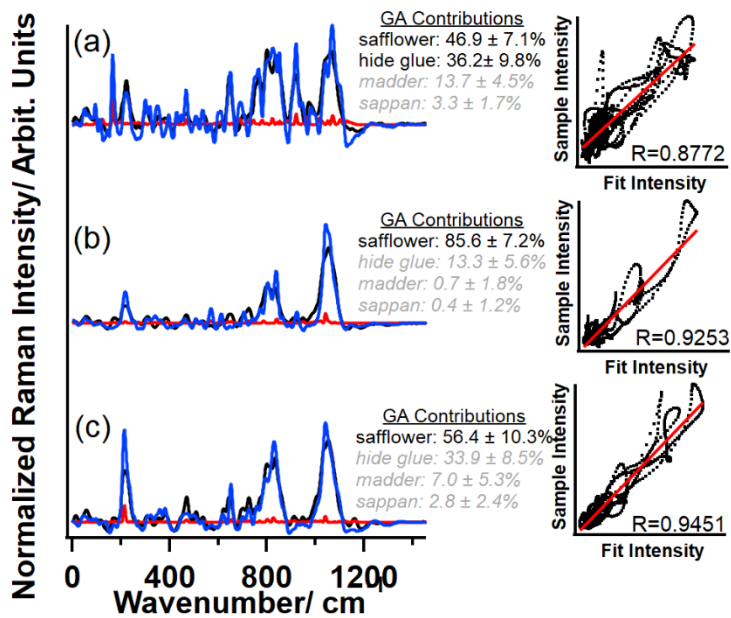
Figure 5.8: SERS spectra and corresponding GA fit results for pink colored areas. Spectra (a) and (b) are from the floor on *Koshikibu no Naishi* (32.69), spectrum (c) is from the screen in *Gi (Righteousness)* (35.39). Blue traces are the sample spectra, black traces are the fit spectra, and red traces are the squared difference. The inset plots to the right show the correlation between the sample and its fit spectrum.

Table 5.1: Summary of selected Suzuki Harunobu prints in the collection of the Portland Art Museum (PAM). Results of each analysis performed are included in the table.

PAM Acc. No.	Title	Date	Location	Visible Light Appearance	UV Light appearance[1]	IRR Absorbance[3]	Unique XRF Results[4]	Particle Size	Raman Results	SERS Results
32.68	The Faithful Wife, from the Kawachigoe Episode of The Tales of Ise: Calendar Print for 1765	1765	red stamp	dark red	UV-Abs	None.	Hg			
			outer kimono	dark red	FL	pattern	N.I.E.			
			solid kimono	medium red	FL	None.	N.I.E.			
			area behind	pink	Min-FL	None.	N.I.E.			
			pink wall tile	pink	Non-FL	V Refl.	N.I.E.			
32.69	Koshikibu no Naishi (The Koshikibu Handmaid), from an untitled series of Hyakunin isshu (One Hundred Poets, One Poem Each)	1767/1768	Door & railings	red-orange	Non-FL	discoloration: IR Abs	Pb	7.11 (8.30); 6.37 (5.05)	red lead	safflower + madder
			orange hakama	red-orange	FL	None.	N.I.E.	11.59 (12.03)	NR	safflower
			pink floor	pink	Non-FL	discoloration: IR Abs	Pb	33.89 (N/A); 5.10 (4.91)	red lead	safflower
32.70	Tokei no banshō (Evening Bell of the Clock), from the series Zashiki hakkei (Eight Views of the Parlor)	1766/1768	brown deck	dark red	UV-Abs	IR Abs	Fe			
			LF kimono, plaid	medium red	FL	weak	Mn			
			floor	pink	Min-FL	None.	Ni			
32.71	Renshi, from the series Fūryū goshiki-zumi (A Stylish Version of Five Colors of Ink)	ca. 1768	deck	red-orange	Non-FL	discoloration weak	Pb	14.87 (14.61); 2.60 (1.36)	red lead	safflower + madder
			inner kimono	medium red	FL	None	N.I.E.	7.77 (5.68)	NR	no ID
			bolster pillow end	medium red	FL	None.	N.I.E			
			wall tile	pink	Min-FL	None.	N.I.E.			

PAM Acc. No.	Title	Date	Location	Visible Light Appearance	UV Light appearance[1]	IRR Absorbance[3]	Unique XRF	Particle Size	Raman Results	SERS Results
32.73	Motoura of the Minami Yamazakiya: Yaezakura (Double-petaled Cherry Blossom), from the series Ukiyo bijin hana ni yosu (Flowers of Beauty from the Floating World)	1769/ 1770	LF outer kimono	dark red	FL	None.	N.I.E.			
			window ledge	pink	Non-FL	None.	Ca			
			RF inner kimono	pink	FL	None.	Ar*			
32.75	Ono no Komachi, from the series Fūryū rokkasen (The Fashionable Six Poetic Immortals)	ca. 1768	red post	red-orange	Non-FL	very weak	Pb	7.03 (5.28); 7.58 (5.20)	red lead	safflower + madder
			futon	medium red	FL	None.	Mn	4.62 (2.27)	NR	safflower
			LF inner kimono	medium red	FL	None.	N.I.E.	4.28 (1.29)	NR	safflower + madder
32.77	Sanseki (The Three Evening Poems): Teika, Jakuren, and Saigyō	ca. 1770	table	red-orange, discolored	Non-FL	discoloration weak	Pb			
			CF inner kimono	medium red	FL	None.	N.I.E.			
32.78	Hibun (A Secret Missive)	1767/ 1768	pink floor	pink	Non-FL	None.	Ca			
			sky	pink	FL	None.	Ni			
			wood panel	dark red	UV-Abs	Abs	Fe			
			railing	red-orange	Non-FL	discoloration: weak	Pb			
			maple leaves	medium red	Non-FL	None.	Ca, Pb			
32.79	Fukurokuji no atama o soru yūjo (Courtesan Shaving the Head of Fukurokuju)	ca. 1769	decking	red-orange	Non-FL	None.	Pb			
			RF outer kimono	medium red	FL	None.	N.I.E.			
			god's head	pale pink	Non-FL	None.	Ca			

PAM Acc. No.	Title	Date	Location	Visible Light Appearance	UV Light appearance[1]	IRR Absorbance[3]	Unique XRF Results[4]	Particle Size	Raman Results	SERS Results
32.81	*Kaminari (Thunder)*	1766/1770	red lantern base	dark red	UV-Abs	weak	Fe			
			flags	pink	Min-FL	None.	N.I.E.			
32.82	*Yayoi (The Third Month), from the series Fūzoku shiki kasen (Contemporary Versions of the*	ca. 1769	Red ground	dark red	FL	weak	Ni			
			LF outer kimono	brown-pink	Min-FL	weak	N.I.E.			
32.83	*Ishiyama no shūgetsu (Autumn Moon at Ishiyama), from an untitled series of Ōmi hakkei (Eight Views of Ōmi)*	ca. 1768/1769	red table	dark red	UV-Abs	weak	Fe			madder
			inner kimono	medium red	FL	None.	N.I.E.	9.29 (2.54)	NR	
			light wall	pink	Non-FL	None.	Pb	3.10 (3.17)	NR	no colorant
			baseboard	orange-pink	Non-FL	None.	Pb	3.31 (0.89)	NR	safflower + madder
32.84	*Kyōdai no shūgetsu (Autumn Moon of the Mirror), from the series Zashiki hakkei (Eight Views of the Parlor)*	ca. 1766/1768	lion's mane	dark red	UV-Abs	weak	Fe			
			frond	medium red	FL	very weak	N.I.E.	7.26 (5.77)	NR	safflower
			RF inner kimono	medium red	FL	None.	N.I.E.			
32.87	*Jakuren, from the series Sanseki (Three Evening Poems)*	ca. 1765/1766	outer kimono	medium red	FL	None.	N.I.E.			
32.88	*Ōgi no seiran (Clearing Weather of the Fan), from the series Zashiki hakkei (Eight Views of the Parlor)*	ca. 1766/1768	red wall panel	dark red	UV-Abs	weak	Fe			
			LF kimono	pink	FL	None.	N.I.E.			
32.89	*Sugoroku no kenka (Children Quarreling over a Sugoroku Game)*	1768-1770	front figure kimono	medium red	FL	None.	N.I.E.			

PAM Acc. No.	Title	Date	Location	Visible Light Appearance	UV Light appearance[1]	IRR Absorbance[3]	Unique XRF Results[4]	Particle Size	Raman Results	SERS Results
32.90	Yamabe no Akahito, from an untitled series of Hyakunin (One Hundred Poets, One Poem Each)	1767/1768	bucket	orangey-pink	Min-FL	None.	N.I.E.			
32.93	Little peachling: calendar print for 1765	1765	Inner kimono	brown-pink	Non-FL	None.	Cu			
			peach blossom	brown-pink	Non-FL	None.	N.I.E.			
32.96	Admiring the Reflection in a Water Basin	1768/1769	Woman's inner kimono	pink	Min-FL	None.	Ca			
			RF kimono	medium red	FL	None.	N.I.E.			
35.39	Gi (Righteousness), from the series Gojō (The Five Confucian Virtues)	1767	brazier box	dark red	Non-FL	very weak	N.I.E.	12.13 (14.61)	NR	safflower + madder
			brazier inner cup	medium red	FL	None.	N.I.E.	4.52 (3.14)	NR	safflower + madder
			pink screen	pink	Min-FL	None.	N.I.E.	14.07 (16.39)	NR	safflower
82.2	Ide no Tamagawa: Yamashiro no meisho (The Ide Jewel River: A Famous Place in Yamashiro Province), from the series Fūzoku Mu Tamagawa (The Six Jewel Rivers in...	ca. 1769/1770	RF inner kimono	medium red	FL	very weak	N.I.E.			
1995.60.4	Fumi yomu danjo (Couple Reading a Letter)	1765/1770	blanket edge	dark red	UV-Abs	None.	Mn, Fe, Zn, Hg			
			red signature	dark red	UV-Abs	None.	Fe, Hg			
			LF kimono	red-orange	Non-FL	None.	Ni, Pb			
2016.18.1	The Departure	1768/1769	futon	medium red	FL	None.	N.I.E.	7.29 (3.54); 14.07 (16.39)	NR	safflower + madder

5.3 Discussion

5.3.1 Substrate

From the FTIR analysis, it was confirmed that the substrate consists of bast fiber paper, consistent with *kōzo*. Signals from Amide I and II stretches suggest the prints were made with colorants bound in animal hide glue and/or the paper was sized with *dōsa* (though evidence of alum was not found.) These findings are consistent with the literature regarding woodblock printmaking[1].

5.3.2 Opaque Reds

Opaque red colorants were definitively identified by non-invasive methods and no further analysis was necessary. These color fields aligned with two colorants based on their elemental analysis—vermilion (Hg) and red ochre (Fe). Vermilion was only present in three areas on two prints in the PAM's collection of 32—twice in seals on the print and only once as part of the image.

Ochre appeared on six prints. This colorant was observed only on periphery features of the image—never on a central figure. In all instances, ochre was used to color the image of a hard surface (e.g tables, cabinets, railings, rocks, mirrors).

5.3.3 Red-Orange

Three areas were micro-sampled and analyzed by Raman and SERS. In all three cases, red lead was identified in the colorant mixture by Raman analysis. The results of SERS analysis suggest that red lead was consistently mixed with madder and safflower, likely in an effort to produce the red-orange shade observed in the collection. Of eight red-orange-colored areas, six are wooden structures, e.g., decks, railings, or door frames. The remaining two red-orange areas are maple leaves and a kimono.

5.3.4 Medium Reds

Medium red areas that were semi-transparent and fluorescent under UV light make up a significant portion of the areas of interest in this collection. The majority of these 22 areas were located on textiles, such as kimono, pillows, and futons. Only four medium-red areas represent non-fabric elements.

Nine of these areas were micro-sampled and analyzed by Raman and SERS. Of those nine areas, four were depictions of a kimono, and another area, depicting a plant frond, was printed in the exact same shade of medium-red as the kimono on the same print, *Kyōdai no shūgetsu (Autumn Moon of the Mirror)* (32.84). Two areas were determined to be colored with safflower dye, one with madder, one with a mixture of safflower and madder, and one was not identified in this study. One of the areas identified as safflower, the orange *hakama* on *Koshikibu no Naishi* (32.69), is visually more brightly orange than other areas. Additional XRF analysis of this area suggests a small amount of arsenic and sulfur, which may be evidence of overprinting an orpiment base layer. Use of orpiment and overprinting has previously been identified in works by Harunobu[2].

5.3.5 Pinks

Light pink areas appear primarily in depictions of hard surfaces, e.g., flooring, walls, or screens. Pale pinks were not commonly used on central figures, perhaps because this would dilute the focus on the primary subject. These color fields represent a range from pale pink-tan to more opaque true pinks. In only one case was an inorganic colorant (red lead) identified. The other two areas that showed evidence of lead (*Ishiyama no*
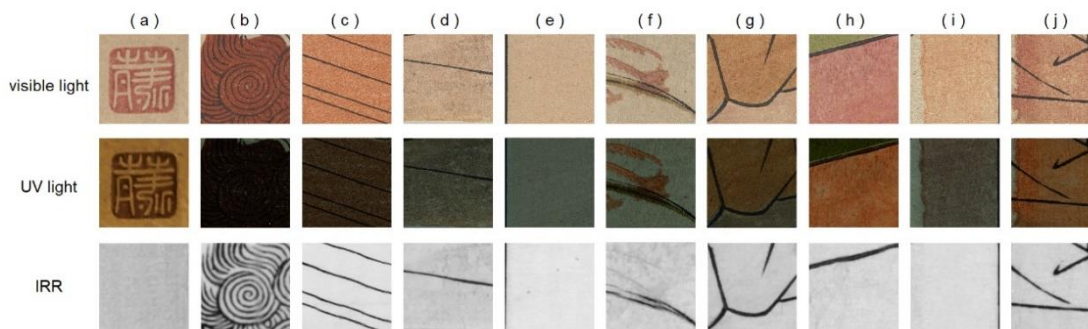
Figure 5.9: Examples of different red colorants across the collection (top-to-bottom: image under visible light illumination, UV light illumination and infrared reflectography). (a) vermilion, (b) iron oxide, (c) red lead, madder, and safflower, (d) red lead and safflower, (e) and (f) safflower with differing intensities, (g) safflower possibly printed over a yellow colorant, (h) and (i) madder and safflower, and (j) madder. The variety of color in the collection demonstrates the range of color production and aging of inks. Full Image citations are provided in the experimental section.

shūgetsu (Autumn Moon at Ishiyama) (32.83)*,* light wall and baseboard) may contain small amounts of red lead or lead white, but these could not be identified in this study. The lack of inorganic elements in the XRF and in some cases, prevalence of calcium, confirms the common practice of mixing organic reds with *gofun*, a calcium carbonate pigment from seashells, to produce these light shades.

5.3.6 Summary and Comparison to a Published Study

Figure 5.9 shows the color fields of the identified inks under different lighting conditions. Figure 5.10 provides example prints with colorant identifications. This work complements the results of a study performed on other works attributed to Harunobu.[2] Like the published study, the data in this study show that red lead and ochre were used regularly, however our data suggests red lead was mixed with organic colorants (as opposed to other inorganics) and that iron oxide was printed alone. Additionally, the use of these colorants

also seems to have been reserved for peripheral objects and architectural details within the image.
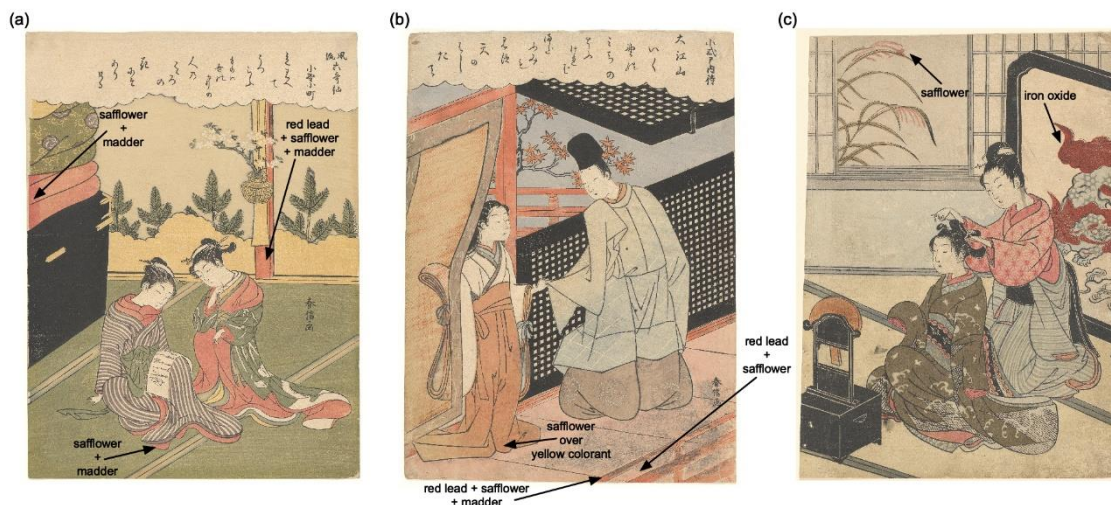
Figure 5.10: Examples of red palettes across the collection. (a) Suzuki Harunobu (Japanese, 1725?- 1770), *Ono no Komachi, from the series Fūryū rokkasen (The Fashionable Six Poetic Immortals)*, ca. 1768, color woodblock print with light embossing on paper; *chūban nishiki-e* image: 11 7/16 in x 8 7/16 in; sheet: 11 7/16 in x 8 1/2 in, The Mary Andrews Ladd Collection. Portland Art Museum, Portland, Oregon, 32.75. (b) Suzuki Harunobu (Japanese, 1725?- 1770), *Koshikibu no Naishi (The Koshikibu Handmaid), from an untitled series of Hyakunin isshu (One Hundred Poets, One Poem Each),* 1767/1768, color woodblock print with embossing on paper; *chūban nishiki-e*, image/sheet: 10 7/8 in x 8 in, The Mary Andrews Ladd Collection. Portland Art Museum, Portland, Oregon, 32.69. (c) Suzuki Harunobu (Japanese, 1725?- 1770), *Kyōdai no shūgetsu (Autumn Moon of the Mirror), from the series Zashiki hakkei (Eight Views of the Parlor)*, ca. 1766/1768, color woodblock print with embossing on paper; *chūban nishiki-e*, image/sheet: 10 1/2 in x 7 9/16 in, The Mary Andrews Ladd Collection. Portland Art Museum, Portland, Oregon, 32.84. (a) includes two unique red colorants. (b) has three unique red colorants—two mixtures of chromophores and one single-chromophore colorant, likely printed over a yellow colorant. (c) includes two unique red colorants, both comprised of a single chromophore in hide glue.

The previous study identified the prevalent use of madder, alone and in mixtures with safflower or sappan. The suggested practice of color-mixing was likewise confirmed in our study. Prevalence of madder colorant (especially madder mixed with safflower) was also observed in the Portland Art Museum's Harunobu collection. In contrast to previous

106

studies, the evidence presented herein suggests that sappan colorant was not widely used. Given the extreme pH and photosensitivity of brazilein[32, 33], the primary color contributing compound in sappan, its color production may have been less reliable than safflower and madder.

In one case, this study encountered an orange area identified as safflower, which we propose to be a red layer overprinted on yellow (perhaps orpiment). Yellow colorants overprinted with red have been previously noted, with examples of primarily inorganic mixtures (e.g., red lead, orpiment, and iron oxide), primarily organic (e.g., safflower over turmeric), and inorganic-organic overprinting (e.g., madder and sappan over orpiment)[2].The results of these analyses align with the red palettes previously defined in the literature[3-5, 10], except for the (lack) of sappan.

5.4 Conclusions

In this work, red colorants on a collection of eighteenth-century woodblock prints by the artist Suzuki Harunobu were evaluated through a multi-analytical methodology. The results of this survey suggest that in the discrete period of five years in which Harunobu was designing full-color prints, a wide range of red colorants were in use. These analyses revealed the use of ochre, vermilion, red lead, safflower, and madder colorants; these colorants were used as a single colorant, as well as two- and three-colorant mixtures. Surprisingly, no evidence of sappan was identified. The results of this work provide definitive molecular identifications of colorants and agree with the results of a previous study on the work of Suzuki Harunobu.

5.5 Experimental

5.5.1 Materials

Glycerol, polyacrylic acid (PAA), 2-acrylamido-2-methyl-1-propanesulfonic acid (AMPS, sodium salt, 50% w/v), N,N'-methylenebis(acrylamide) (MBA), silver nitrate, and hydroxylamine hydrochloride were purchased from Millipore-Sigma (St. Louis, MO). Potassium persulfate (KPS), potassium metabisulfite (KMBS), lead (II,IV) oxide, and sodium hydroxide were purchased from Thermo-Fisher (Waltham, MA). Dow SYLGARD™ 184 Silicone Encapsulant (PDMS) was purchased from Ellsworth Adhesives (Germantown, WI). All chemicals were used as received. All aqueous solutions were prepared using water filtered through an ion-exchange column (measured resistance greater than 18 MΩ).

5.5.2 Hydrogel synthesis

AMPS-co-PAA hydrogels were synthesized previously reported in the literature.[34] Final weight ratios of components were 18.3% AMPS, 11.2% PAA, 8.1% glycerol, 0.3% MBA, and 0.02% each KPS and KMBS. The gels were allowed to rest in the mold overnight to ensure polymerization was complete, and then removed and equilibrated in deionized water to remove excess reactants. Gels underwent a second equilibration in deionized water before use.

5.5.3 Silver nanoparticle syntheses

Silver nanoparticles (AgNPs) were synthesized according to optimized methods.[26] $AgNO_3$ (1.00×10^{-4} M) and NH_3OH (1.50×10^{-4} M in 3.33×10^{-4} M NaOH) solutions were freshly prepared before beginning synthesis. To synthesize nanoparticles, 90 mL of $NH_3OH \cdot HCl$ and 10 mL of $AgNO_3$ were mixed under N_2 sparging. After mixing, the

solutions were allowed to react for 5 minutes. Aliquots of 1 mL were then centrifuged at 5000 rpm for 5 minute to concentrate the AgNPs. 950 µL of supernatant were removed and 50 µL of fresh deionized water was added to the remaining pellet. Concentrated AgNP solutions were stored in the dark at 4 °C until ready for use.

5.5.4 Harunobu Prints analyzed

A total of 23 prints attributed to Suzuki Harunobu were examined. All 23 prints were imaged and analyzed by XRF. Seven prints were selected for micro-sampling and Raman/SERS analysis; a total of 21 samples were collected, accounting for 16 color fields. Full visible light and UV light illuminated images of sampled prints are provided in the supplementary information. One fiber was collected and analyzed by FTIR, Raman, and SERS. A complete list of the prints examined is provided in Table 1.

Images included in this research article have been reproduced with permission from the Portland Art Museum and full citations include:

Figure 5.1: Suzuki Harunobu (Japanese, 1725?- 1770), *Renshi, from the series Fūryū goshiki-zumi (A Stylish Version of Five Colors of Ink),* ca. 1768, color woodblock print with embossing on paper; *chūban nishiki-e,* image: 11 5/16 in x 8 5/16 in; sheet 11 3/8 in x 8 9/16 in, The Mary Andrews Ladd Collection. Portland Art Museum, Portland, Oregon, 32.71.

Figure 5.10a: Suzuki Harunobu (Japanese, 1725?- 1770), *Ono no Komachi, from the series Fūryū rokkasen (The Fashionable Six Poetic Immortals)*, ca. 1768, color woodblock print with light embossing on paper; *chūban nishiki-e* image: 11 7/16 in x 8 7/16 in; sheet: 11 7/16 in x 8 1/2 in, The Mary Andrews Ladd Collection. Portland Art Museum, Portland, Oregon, 32.75

Figure 5.10b: Suzuki Harunobu (Japanese, 1725?- 1770), *Koshikibu no Naishi (The Koshikibu Handmaid), from an untitled series of Hyakunin isshu (One Hundred Poets, One Poem Each),* 1767/1768, color woodblock print with embossing on paper; chu *chūban nishiki-e*, image/sheet: 10 7/8 in x 8 in, The Mary Andrews Ladd Collection. Portland Art Museum, Portland, Oregon, 32.69

Figure 5.10c: Suzuki Harunobu (Japanese, 1725?- 1770), *Kyōdai no shūgetsu (Autumn Moon of the Mirror), from the series Zashiki hakkei (Eight Views of the Parlor),* ca. 1766/1768, color woodblock print with embossing on paper; *chūban nishiki-e*, image/sheet: 10 1/2 in x 7 9/16 in, The Mary Andrews Ladd Collection. Portland Art Museum, Portland, Oregon, 32.84

Figure 5.9a: (DETAIL) Suzuki Harunobu (Japanese, 1725?- 1770), *Fumi yomu danjo (Couple Reading a Letter)*, 1765/1770, color woodblock print on paper; *chūban nishiki-e*, image/sheet: 10 3/8 in x 7 3/4 in, Gift of Judith P. Benson. Portland Art Museum, Portland, Oregon, 1995.60.4

Figure 5.9b and f: (DETAIL) Suzuki Harunobu (Japanese, 1725?- 1770), *Kyōdai no shūgetsu (Autumn Moon of the Mirror), from the series Zashiki hakkei (Eight Views of the Parlor)*, ca. 1766/1768, color woodblock print with embossing on paper; *chūban nishiki-e*, image/sheet: 10 1/2 in x 7 9/16 in, The Mary Andrews Ladd Collection. Portland Art Museum, Portland, Oregon, 32.84

Figure 5.1b and Figure 5.9c: (DETAIL) Suzuki Harunobu (Japanese, 1725?- 1770) *Renshi, from the series Fūryū goshiki-zumi (A Stylish Version of Five Colors of Ink),* ca. 1768, color woodblock print with embossing on paper; *chūban nishiki-e,* image: 11 5/16 in x 8

5/16 in; sheet 11 3/8 in x 8 9/16 in, The Mary Andrews Ladd Collection. Portland Art Museum, Portland, Oregon, 32.71.

Figure 5.9d and g: (DETAIL) Suzuki Harunobu (Japanese, 1725?- 1770), *Koshikibu no Naishi (The Koshikibu Handmaid), from an untitled series of Hyakunin isshu (One Hundred Poets, One Poem Each)*, 1767/1768, color woodblock print with embossing on paper; chu *chūban nishiki-e*, image/sheet: 10 7/8 in x 8 in, The Mary Andrews Ladd Collection. Portland Art Museum, Portland, Oregon, 32.69

Figure 5.9e: (DETAIL) Suzuki Harunobu (Japanese, 1725?- 1770), *Gi (Righteousness), from the series Gojō (The Five Confucian Virtues)*, 1767, color woodblock print with embossing on paper; *chūban nishiki-e,* image: 10 7/8 in x 8 1/16 in; sheet: 11 3/8 in x 8 1/16 in, Bequest of Winslow B. Ayer. Portland Art Museum, Portland, Oregon, 35.39

Figure 5.9h: (DETAIL) Suzuki Harunobu (Japanese, 1725?- 1770), *The Departure*, 1768/1769, color woodblock print with embossing on paper; nishiki-e, image: 11 1/4 in x 8 1/8 in; sheet: 11 5/16 in x 8 9/16 in, Museum Purchase: Funds provided by the Asian Art Council and Asian Art auction proceeds. Portland Art Museum, Portland, Oregon, 2016.18.1

Figure 5.9i and j: (DETAIL) attributed to Suzuki Harunobu (Japanese, 1725?- 1770), *Ishiyama no shūgetsu (Autumn Moon at Ishiyama), from an untitled series of Ōmi hakkei (Eight Views of Ōmi)*, ca. 1768/1769, color woodblock print on paper; chūban nishiki-e, image/sheet: 10 1/4 in x 7 3/4 in, The Mary Andrews Ladd Collection. Portland Art Museum, Portland, Oregon, 32.83

5.5.5 Methods

5.5.5.1 Micro-sampling process

Micro-sampling was performed using a hydrogel-assisted micro-sampling device.[25] This handheld assembly uses a small (1 cm^2) piece of hydrogel loaded into an open-ended plastic cup. Before assembly, the hydrogel was equilibrated in the museum environment (50% RH, 21°C) and excess moisture was wicked away using a KimWipe. The open end of the cup was covered with low density plastic film, which has an approximately 1mm^2 pinhole. The other side of the cup was sealed using custom molded PDMS stoppers, providing a clear line of sight down the center of the cup, through the hydrogel, and to the pinhole. The apparatus was placed on the surface of the print for 70 seconds, then lifted vertically before inverting and storing in a sealed container for analysis.

5.5.5.2 Imaging

White light and UV illuminated images were collected with a Canon 7dmkII camera with an EF 50mm F/2.5 lens, MaxMax XNiteCC1 and Kodak Wratten 2E filters. VioStorm WildFire VS-60 lights were used for UV illumination with GoldenThread OLT 0.50x and UV Innovations Target UV and UV gray cars for color balancing. RAW images were color balanced using CaptueOne software (v10.2.1).

All additional Image processing was performed using FIJI (ImageJ 1.53c)[35].

5.5.5.3 XRF spectroscopy

XRF spectra were collected from unique red, orange and pink-colored areas, as well as from a blank area of paper, when possible. Prints were raised from their mats by placing

low-density foam under the print. The spectra were collected using a 0.025 mm Ti filter, 15 kV excitation, 25.8 μA, and 60 s data accumulation.

Sixteen paper spectra were averaged and a threshold for elemental presence was established according to 1) a signal-to-noise ratio (SNR) greater than 10 and 2) signal greater than two and a half standard deviations above the blank paper average.

5.5.5.4 FTIR

FTIR analysis was performed using a Nicolet Continuμm FTIR microscope with a Nicolet iS10 infrared spectrometer (Thermo Fisher Scientific, Waltham, MA) and 50 um nitrogen cooled MCT/A detector The sample was prepared for analysis by pressing onto a diamond window. All data were collected using Omnic software (v8.3.103) and spectra were collected in transmission mode from 650 to 4000 cm^{-1} at 4 cm^{-1} spectral resolution and 128 scans averaged. Data were mateched to reference spectra from the IRUG database[28, 29]

5.5.5.5 Raman spectroscopy

Raman spectroscopy was performed directly on the hydrogel surface where particles had been collected. Spectra were collected on a LabRAM HR Evolution spectrometer with 100×100 cm motorized stage and motorized z-axis control(Horiba, Kyoto, Japan). Parameters for all spectra were 633 nm laser, 600 lines/mm grating, 300 μm confocal hole, and 50× objective. Laser power, acquisition time, and accumulations were optimized for each sample. Raman spectra were collected over the range of 18-2000 cm^{-1} and SERS spectra were collected from 400-2000 cm^{-1}.

5.5.5.6 SERS

After collecting Raman spectra, AgNPs were drop cast over the pinhole in the micro-sampling assembly. Excess water was allowed to absorb into the hydrogel, forming a thin film of Ag on the surface of the sample particulate. Measurements were then collected *in situ* with the parameters previously described. Baseline correction was performed using an AutoAdaptive Baseline Subtraction algorithm. SERS spectra were analyzed by fitting with a self-built genetic algorithm (GA). Development of both the baseline subtraction and GA for these applications have been fully described elsewhere.[25]

5.5.5.7 Particle Size Analysis

Images of the hydrogel surfaces were collected using the 3MP iDS camera with CMOS sensor connected to the Raman microscope. The images were then color processed, converted to binary and particles were measured using the Analyze Particles function in Fiji. The minimum particle diameter for measurement was defined as 3 pixels wide, corresponding to 0.3 μm^2 at 50× magnification, and 1.5 μm^2 at 10× magnification.

5.6 References

1.   Mihara, S., Ukiyoe. Some Aspects of Japanese Classical Picture Prints. *Monumenta Nipponica* **1943,** *6* (1/2), 245-261.

2.   Wright, J.; Derrick, M.; Adachi, M., The colors of desire: Beauties of the Yoshiwara observed. *Harunobu from the Museum of Fine Arts, Boston. Tokyo: Nikkei* **2017**, 259-63.

3.   Derrick, M.; Newman, R.; Wright, J., Characterization of Yellow and Red Natural Organic Colorants on Japanese Woodblock Prints by EEM Fluorescence Spectroscopy. *J. Am. Inst. Conserv.* **2017,** *56* (3-4), 171-193.

4.   Keyes, R. S.; Feller, R. L., *Japanese woodblock prints: a catalogue of the Mary A. Ainsworth Collection*. Allen Memorial Art Museum: 1984.

5.   Takamatsu, T., *On Japanese pigments*. Department of Science in Tokio Daigaku Tokyo: 1878.

6.   Yamasaki, K.; Yoshimichi, E., Pigments Used on Japanese Paintings from the Protohistoric Period through the 17th Century. *Ars Orientalis* **1979,** *11*, 1-14.

7.   Whitmore, P. M.; Cass, G. R., The ozone fading of traditional Japanese colorants. *Studies in Conservation* **1988,** *33* (1), 29-40.

8.   Whitmore, P. M.; Pan, X.; Bailie, C., Predicting The Fading of Objects: Identification of Fugitive Colorants Through Direct Nondestructive Lightfastness Measurements. *J. Am. Inst. Conserv.* **1999,** *38* (3), 395-409.

9.   Fiske, B. J., Conservation of Japanese Woodblock Prints: Display, Storage and Treatment. *Impressions* **2006,** (28), 60-75.

10.   Biron, C.; Mounier, A.; Arantegui, J. P.; Bourdon, G. L.; Servant, L.; Chapoulie, R.; Roldán, C.; Almazán, D.; Díez-de-Pinos, N.; Daniel, F., Colours of the « images of the floating world ». non-invasive analyses of Japanese ukiyo-e woodblock prints (18th and 19th centuries) and new contributions to the insight of oriental materials. *Microchem. J.* **2020,** *152*, 104374.

11.   Villafana, T.; Edwards, G., Creation and reference characterization of Edo period Japanese woodblock printing ink colorant samples using multimodal imaging and reflectance spectroscopy. *Heritage Sci.* **2019,** *7* (1).

12.   Cesaratto, A.; Luo, Y.-B.; Smith, H. D.; Leona, M., A timeline for the introduction of synthetic dyestuffs in Japan during the late Edo and Meiji periods. *Heritage Sci.* **2018,** *6* (1), 22.

13.   Mounier, A.; Le Bourdon, G.; Aupetit, C.; Lazare, S.; Biron, C.; Pérez-Arantegui, J.; Almazán, D.; Aramendia, J.; Prieto-Taboada, N.; Fdez-Ortiz de Vallejuelo, S.; Daniel, F., Red and blue colours on 18th–19th century Japanese woodblock prints: In situ analyses by spectrofluorimetry and complementary non-invasive spectroscopic methods. *Microchem. J.* **2018,** *140*, 129-141.

14.   Fonseca, B.; Schmidt Patterson, C.; Ganio, M.; Maclennan, D.; Trentelman, K., Seeing red: towards an improved protocol for the identification of madder- and cochineal-based pigments by fiber optics reflectance spectroscopy (FORS). *Heritage Sci.* **2019,** *7* (1).

15.   Tamburini, D., Investigating Asian colourants in Chinese textiles from Dunhuang (7th-10th century AD) by high performance liquid chromatography tandem mass

spectrometry – Towards the creation of a mass spectra database. *Dyes Pigm.* **2019,** *163*, 454-474.

16.	Maynez-Rojas, M. A.; Casanova-González, E.; Ruvalcaba-Sil, J. L., Identification of natural red and purple dyes on textiles by Fiber-optics Reflectance Spectroscopy. *Spectrochim. Acta Part A* **2017,** *178*, 239-250.

17.	Vermeulen, M.; Leona, M., Evidence of early amorphous arsenic sulfide production and use in Edo period Japanese woodblock prints by Hokusai and Kunisada. *Heritage Sci.* **2019,** *7* (1), 73.

18.	Amato, F.; Micciche', C.; Cannas, M.; Gelardi, F. M.; Pignataro, B.; Li Vigni, M.; Agnello, S., Ag nanoparticles agargel nanocomposites for SERS detection of cultural heritage interest pigments. *The European Physical Journal Plus* **2018,** *133* (2), 74.

19.	Bruni, S.; Guglielmi, V.; Pozzi, F., Historical organic dyes: a surface-enhanced Raman scattering (SERS) spectral database on Ag Lee–Meisel colloids aggregated by NaClO4. *J. Raman Spectrosc.* **2011,** *42* (6), 1267-1281.

20.	Bruni, S.; Guglielmi, V.; Pozzi, F., Surface-enhanced Raman spectroscopy (SERS) on silver colloids for the identification of ancient textile dyes: Tyrian purple and madder. *J. Raman Spectrosc.* **2009,** *41* (2), 175-180.

21.	Cañamares, M. V.; Mieites-Alonso, M. G.; Leona, M., Fourier transform-Raman and surface-enhanced Raman spectroscopy analysis of safflower red-dyed washi paper: pH study and bands assignment. *J. Raman Spectrosc.* **2020,** *51* (6), 903-909.

22.	Chen, K.; Leona, M.; Vo-Dinh, K.-C.; Yan, F.; Wabuyele, M. B.; Vo-Dinh, T., Application of surface-enhanced Raman scattering (SERS) for the identification of anthraquinone dyes used in works of art. *J. Raman Spectrosc.* **2006,** *37* (4), 520-527.

23.	Leona, M.; Stenger, J.; Ferloni, E., Application of surface-enhanced Raman scattering techniques to the ultrasensitive identification of natural dyes in works of art. *J. Raman Spectrosc.* **2006,** *37* (10), 981-992.

24.	Conservation, A. I. f. Code of Ethics. https://www.culturalheritage.org/about-conservation/code-of-ethics (accessed June 17, 2020).

25.	Kissell, L. N.; Quady, T. K.; Clare, T. L., Optimized micro-sampling and computational analysis for SERS identification of red organic colorants. *Spectrochim. Acta Part A* (Submitted).

26.	Kissell, L. N.; Quady, T. K.; Clare, T. L., Reference data set and characterization of Japanese print materials by Surface-Enhanced Raman Spectroscopy and documentation of non-damage. *Data in Brief* (Submitted).

27.	Kenmotsu, J., Prints for Portland: The Mary Andrews Ladd Collection. In *Great Waves and Mountains: Collecting the Arts of Japan*, O'yobe, N.; Peyton, A. B.; Cofrin, D. A., Eds. University Press of Florida: forthcoming 2022.

28.	Cargille Chemistry Microscopy Set, P. M. o. A., ICB00056 Ramie fiber. Price, B. A.; Pretzel, B.; Picollo, M., Eds. Infrared and Raman Users Group Spectral Database.

29.	Scheidemandel, H.; Center, W. A. C., IPR00016 Glue, hide. Price, B. A.; Pretzel, B.; Picollo, M., Eds. Infrared and Raman Users Group Spectral Database.

30.	BPG Fiber Identification. https://www.conservation-wiki.com/wiki/BPG_Fiber_Identification (accessed August 6, 2021).

31.	Camacho, N. P.; West, P.; Torzilli, P. A.; Mendelsohn, R., FTIR microscopic imaging of collagen and proteoglycan in bovine cartilage. *Biopolymers* **2001,** *62* (1), 1-8.

32.   Ngamwonglumlert, L.; Devahastin, S.; Chiewchan, N.; Raghavan, G. S. V., Color and molecular structure alterations of brazilein extracted from Caesalpinia sappan L. under different pH and heating conditions. *Sci Rep* **2020,** *10* (1), 12386.

33.   Rondão, R.; Seixas de Melo, J. S.; Pina, J.; Melo, M. J.; Vitorino, T.; Parola, A. J., Brazilwood Reds: The (Photo)Chemistry of Brazilin and Brazilein. *J. Phys. Chem. A* **2013,** *117* (41), 10650-10660.

34.   England, A. H.; Clare, T. L., Synthesis and Characterization of Flexible Hydrogel Electrodes for Electrochemical Impedance Measurements of Protective Coatings on Metal Sculptures. *Electroanalysis* **2014,** *26* (5), 1059-1067.

35.   Schindelin, J.; Arganda-Carreras, I.; Frise, E.; Kaynig, V.; Longair, M.; Pietzsch, T.; Preibisch, S.; Rueden, C.; Saalfeld, S.; Schmid, B.; Tinevez, J. Y.; White, D. J.; Hartenstein, V.; Eliceiri, K.; Tomancak, P.; Cardona, A., Fiji: an open-source platform for biological-image analysis. *Nat Methods* **2012,** *9* (7), 676-82.

5.7 Appendix A: Supplementary images of micro-sampled prints
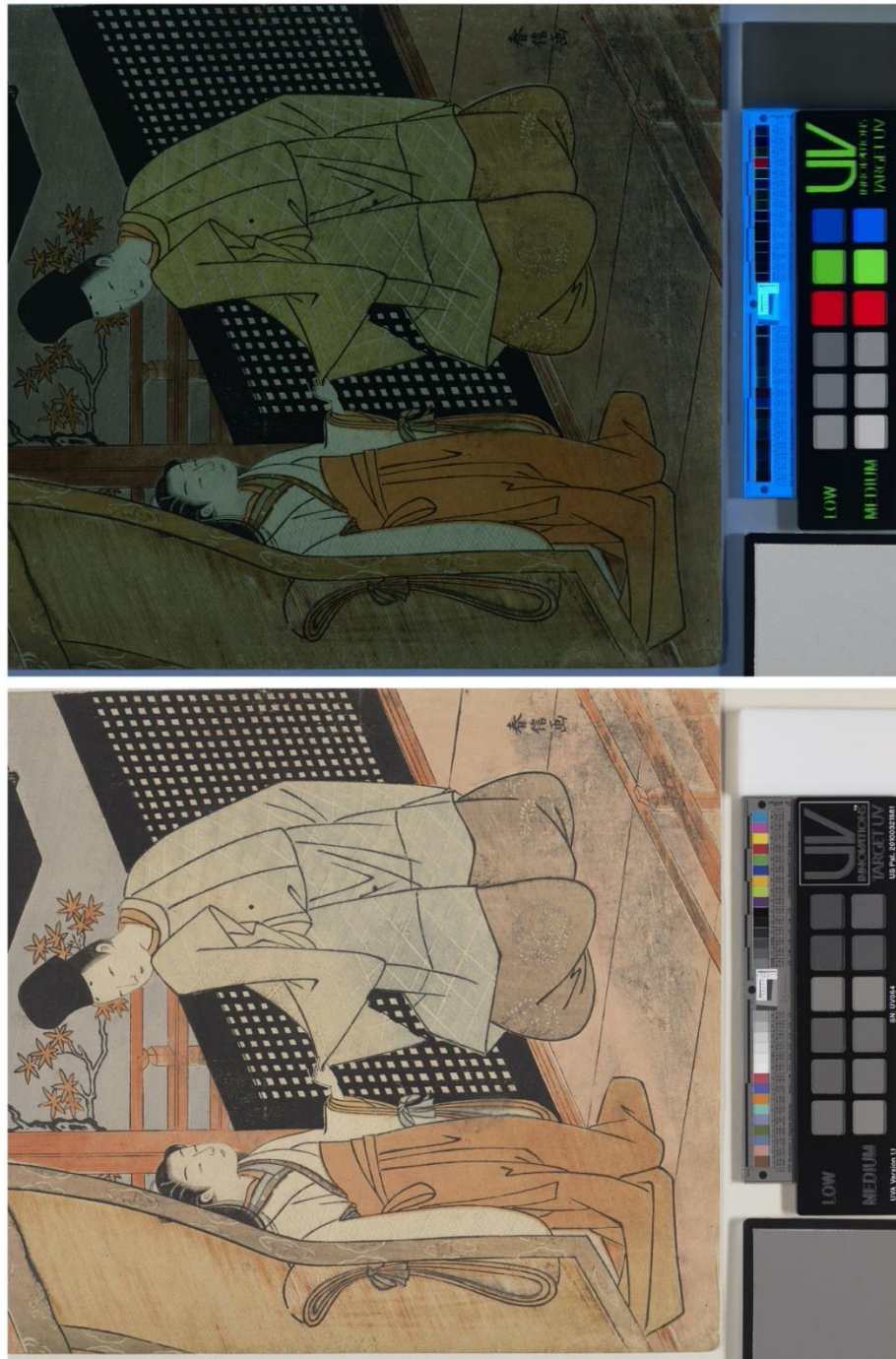
Figure 5.11: (DETAIL) Suzuki Harunobu (Japanese, 1725?-1770), *Koshikibu no Naishi (The Koshikibu Handmaid),from an untitled series of Hyakunin isshu (One Hundred Poets, One Poem Each)*, 1767/1768, color woodblock print with embossing on paper; *chūban nishiki-e*, image/sheet: 10 7/8 in x 8 in, The Mary Andrews Ladd Collection. Portland Art Museum, Portland, Oregon, 32.69. (bottom) Visible light and (top) UV light illuminated images before micro-sampling.

Figure 5.12: Suzuki Harunobu (Japanese, 1725?-1770),*Renshi, from the series Fūryū goshiki-zumi (A Stylish Version of Five Colors of Ink)*, ca. 1768, color woodblock print with embossing on paper; *chūban nishiki-e*, image: 11 5/16 in x 8 5/16 in; sheet: 11 3/8 in x 8 9/16 in, The Mary Andrews Ladd Collection. Portland Art Museum, Portland, Oregon, 32.71. (bottom) Visible light and (top) UV light illuminated images before micro-sampling.
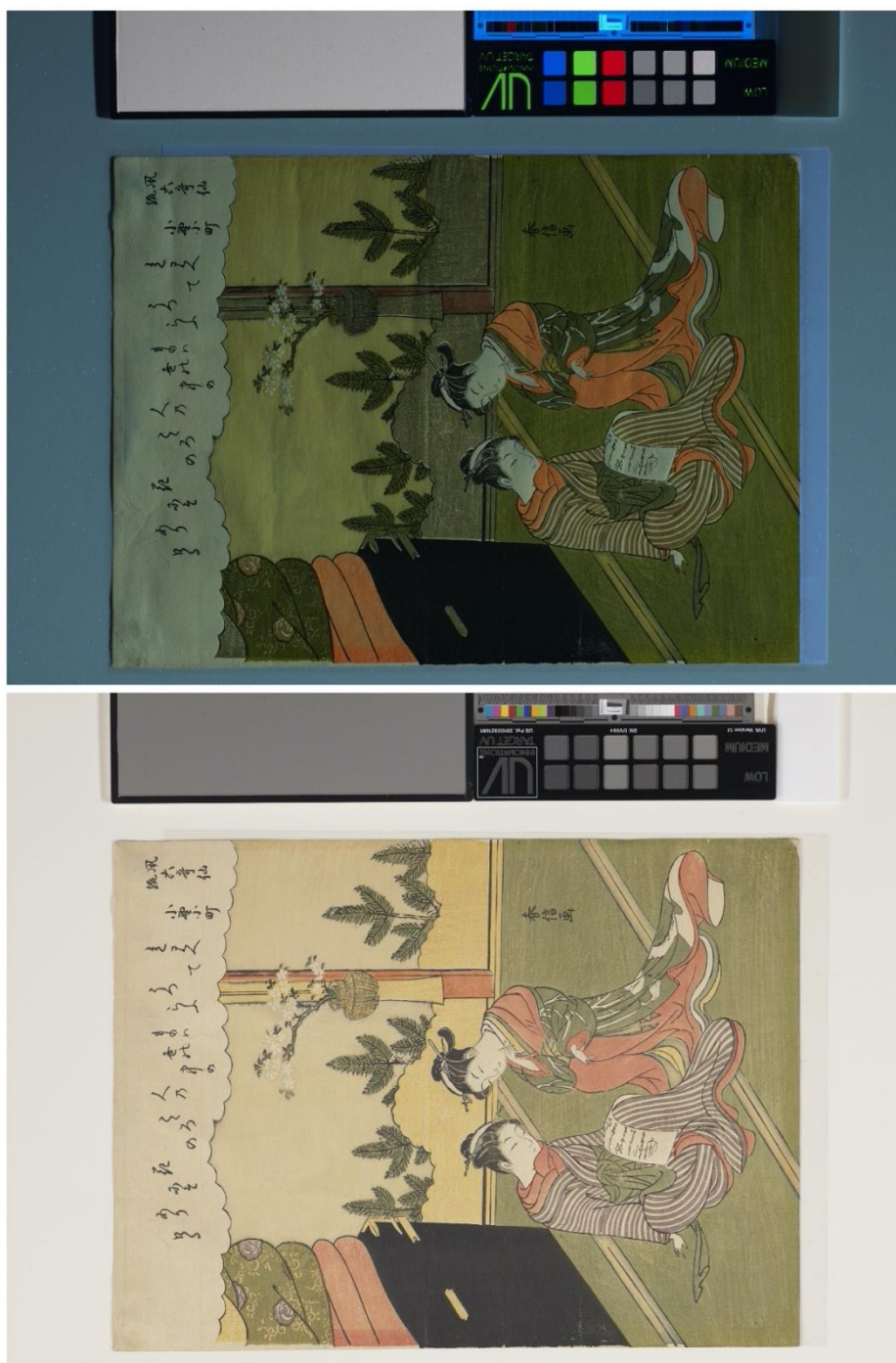
Figure 5.13: Suzuki Harunobu (Japanese, 1725?-1770), *Ono no Komachi, from the series Fūryū rokkasen (The Fashionable Six Poetic Immortals)*, ca.1768, color woodblock print with light embossing on paper; *chūban nishiki-e*, image: 11 7/16 in x 8 7/16 in; sheet: 11 7/16 in x 8 1/2 in, The Mary Andrews Ladd Collection. Portland Art Museum, Portland, Oregon, 32.75. (bottom) Visible light and (top) UV light illuminated images before micro-sampling.

Figure 5.14: (DETAIL) Attributed to Suzuki Harunobu (Japanese, 1725?-1770), *Ishiyama no shūgetsu (Autumn Moon at Ishiyama), from an untitled series of Ōmi hakkei (Eight Views of Ōmi)*, ca. 1768/1769, color woodblock print on paper; chūban nishiki-e, image/sheet: 10 1/4 in x 7 3/4 in, The Mary Andrews Ladd Collection. Portland Art Museum, Portland, Oregon, 32.83. (bottom) Visible light and (top) UV light illuminated images before micro-sampling.

Figure 5.15: (DETAIL) Suzuki Harunobu (Japanese, 1725?-1770),*Kyōdai no shūgetsu (Autumn Moon of the Mirror), from the series Zashiki hakkei (Eight Views of the Parlor)*, ca. 1766/1768, color woodblock print with embossing on paper; *chūban nishiki-e*, image/sheet: 10 1/2 in x 7 9/16in, The Mary Andrews Ladd Collection. Portland Art Museum, Portland, Oregon, 32.84. (top) Visible light and (bottom) UV light illuminated images before micro-sampling.

Figure 5.16: (DETAIL) Suzuki Harunobu (Japanese, 1725?-1770), *Gi (Righteousness), from the series Gojō (The Five Confucian Virtues)*, 1767, color woodblock print with embossing on paper; *chūban nishiki-e*, image: 10 7/8 in x 8 1/16 in; sheet: 11 3/8 in x 8 1/16 in, Bequest of Winslow B. Ayer. Portland Art Museum, Portland, Oregon, 35.39. (bottom) Visible light and (top) UV light illuminated images before micro-sampling.

Figure 5.17: (DETAIL) Suzuki Harunobu (Japanese, 1725?-1770), The Departure, 1768/1769, color woodblock print with embossing on paper; nishiki-e, image: 11 1/4 in x 8 1/8 in; sheet: 11 5/16 in x 8 9/16 in, Museum Purchase: Funds provided by the Asian Art Council and Asian Art auction proceeds. Portland Art Museum, Portland, Oregon, 2016.18.1. (top) Visible light and (bottom) UV light illuminated images before micro-sampling.

Chapter 6: Metal Corrosion—processes, prevention, and detection

The corrosion of cultural heritage materials, such as bronze sculpture, presents unique challenges, as the loss of material translates to loss of definition and fine detail— forever changing the object. Corrosion processes are thermodynamically favored and, thus, virtually irreversible. Often the purpose of a metal object (e.g., tools, jewelry, sculpture) is for it to be used or enjoyed as it was produced and any changes to the object result an alteration of the intended aesthetic of the piece. To preserve metal objects for generations to come, an *in situ* method for corrosion monitoring is needed.

6.1 Corrosion processes

Metal reactions with the environment, collectively known as corrosion, vary widely depending on exact environmental conditions, but result in a compound with metals in a non-zero oxidation state. These reaction pathways can be affected by atmospheric conditions (particulate, gas content), weather (rainfall, wind, sun exposure), and proximity to accelerating factors (industrial byproducts, sea spray)[1].
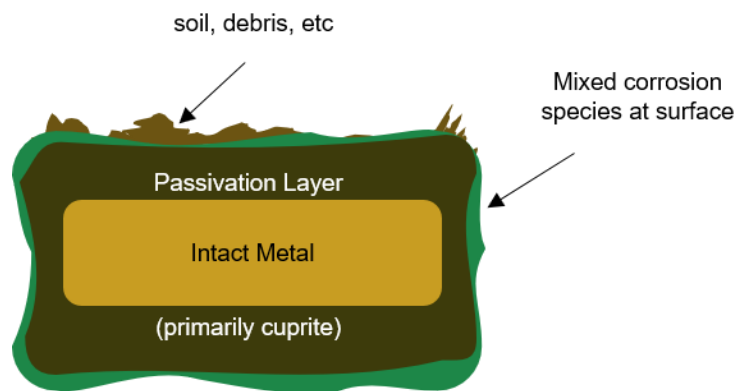
Figure 6.1: Cross-sectional view of copper-based metal with passivation layer and mixed corrosion species on the surface. The ability of ions to migrate through passivation layers means corrosion can proceed, despite passivation, in certain environmental conditions.

Corrosion of copper-based substrates (i.e., brass, bronze) typically results in a thin layer of cuprite Cu_2O, which is stable and considered passivating. Despite this passivating layer, ion migration is possible in both directions—copper ions can migrate from the intact metal and reactive anions can migrate to the intact metal surface. These ion migrations can result in detrimental corrosion, such as "bronze disease" (formation of copper chlorides under the passivated surface). A diagram of a corroded copper substrate is shown in Figure 6.1.

Steel substrates, on the other hand, primarily react with water and dissolved oxygen. Iron's d-electron configuration makes trivalent iron ions the most common charge state in corrosion species[2-5]. These trivalent ions interact with oxygen and water to form oxides and hydroxides, and with environmental contaminates (e.g., H_2S, Cl^-) to form other ionic species.

In all cases, the earliest indicators of corrosion are soluble metal ions—Cu^{2+} for brass/bronze and Fe^{3+} for steel and wrought iron. Corrosion often occurs in microscopic pits, where the microenvironment is much different than the macroenvironment. Thus, it is reasonable to anticipate local ion concentrations in real corrosion measurements may be on the order of parts-per-million. Because the reactivities of different metal alloys vary and are heavily influenced by the environment, rates of corrosion are typically calculated after decades of data collection, a timescale that is not conducive to proactive treatment options. Therefore, techniques for identifying *active corrosion* are needed.

6.2 Current Protective and Detection Methods

Mitigating corrosion relies on advancing both protective methods and detection methods. Protective methods include corrosion inhibitors, protective coatings, and use of

126

sacrificial electrodes. Each of these methods has their strengths, yet, inhibitors and coatings fail, and sacrificial electrodes are bulky and temporary. Because of these limitations, corrosion prevention is temporary; active corrosion detection methods are essential to identify changes at the earliest stage possible.

Corrosion detection methods fall into two categories: indirect and direct. Indirect methods simulate corrosion processes, are destructive, and cannot be used on objects *in situ*. Examples include acoustic emission[6], electrochemical frequency modulation[7], scanning Kelvin probe force microscopy[8, 9], and others[10-16]. Such methods aim to simulate the effects of environment on metal objects and understand how those objects respond. These methods aid in better understanding the behavior of metal objects, but do not allow scientists to draw conclusions about the condition of existing objects.

Direct detection methods measure real corrosion products, are non-destructive to the metal object, and/or may be applied *in situ*. The most broadly used direct detection method is visual assessment, which is only effective once corrosion products are abundant enough to be seen; visual inspection is further complicated when paints or other coatings obscure view of the bare metal. Recently fiber optic reflectance spectroscopy (FORS) has been applied to analyzing the corrosion products on bronze[17] and automated image processing has been introduced for steel[18]. These methods, like visual assessment, rely on corrosion having progressed far enough to be optically detectable. Other examples of direct detection methods include reactive coatings, electrochemical sensors for coating porosity, and sensors for corrosion products. These methods commonly measure peripheral effects of corrosion (e.g., coating damage *via* ion migration[19-21], increased alkalinity due to metal

ion formation [22], counterions of metal salts[-23]) rather than the active corrosion products (i.e., soluble metal ions[24, 25]).

6.3 Fluorescence emission spectroscopy

Methods for metal ion detection in aqueous systems are abundant. One popular method is fluorescence emission spectroscopy[26-32]. Fluorescence spectroscopy benefits from having low limits of detection, providing the potential for detection limits in the parts-per-million (ppm) concentration range. Effective fluorescence probes have been developed for many transition and heavy metal ions in solution, such as Fe^{3+}, Cu^{2+}, Ag^+, Cd^{2+}, and Hg^{2+}[citations]. The implementation of a metal-ion sensitive fluorescence probe in a solid-state application may lead to rapid, *in situ* optical analysis of corrosion on metal substrates.
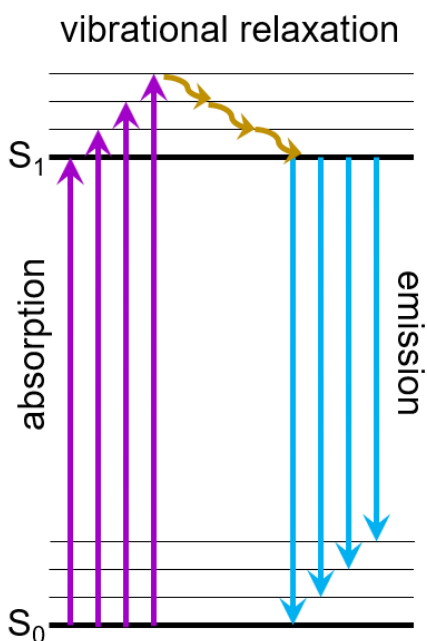
Figure 6.2: Jablonski diagram showing the absorption (purple) of light, exciting electrons into the S_1 state. Vibrational relaxation (yellow) occurs in a non-radiative manner, bringing the excited electron to the lowest energy excited state. The electron then relaxes in a radiative manner, which is observed as emission (blue).

A general fluorescence mechanism is depicted in the simplified Jablonski diagram

in Figure 6.2. Fluorescence occurs through the absorption of a photon by a fluorophore, typically a highly conjugated molecule or a nanoparticle (e.g., CdSe or carbon quantum dots). The absorbed photon provides the energy needed to excite an electron from the ground state to an excited singlet state. Non-radiative transitions bring the electron to the lowest energy excited state, where it then transitions back to the ground state. This final transition emits a photon, which is measurable by a spectrometer. Fluorescence lifetimes, the time an electron spends in the excited state, are on the order of nano- to micro-seconds, fast enough to be observed by the human eye as "instantaneous."

Analytical uses of fluorescence spectroscopy include "turn on" (emission activation) and "turn off" (emission quenching) sensing methods, where the analyte either activates or deactivates the fluorescence emission, respectively. These responses are governed by the Stern-Volmer relationship[33]

Equation 6.1 $$\frac{F_0}{F} = 1 + K_{SV}[Q]$$

Where F_0 is the intensity of fluorescence without analyte, F is the intensity of fluorescence with analyte, K_{SV} is the Stern-Volmer constant, and $[Q]$ is the concentration of analyte. This equation represents the "turn-off" relationship; for a "turn-on" system the dependent variable would be represented as $\frac{F}{F_0}$.

6.4 Electrochemical Impedance spectroscopy

Another method with precedent for monitoring ion concentrations is electrochemical impedance spectroscopy (EIS). EIS is an analytical technique that probes the electrochemical response of a material across a range of applied potential. An AC potential (with fixed magnitude, but changing frequency) is applied to the cell, and two

129
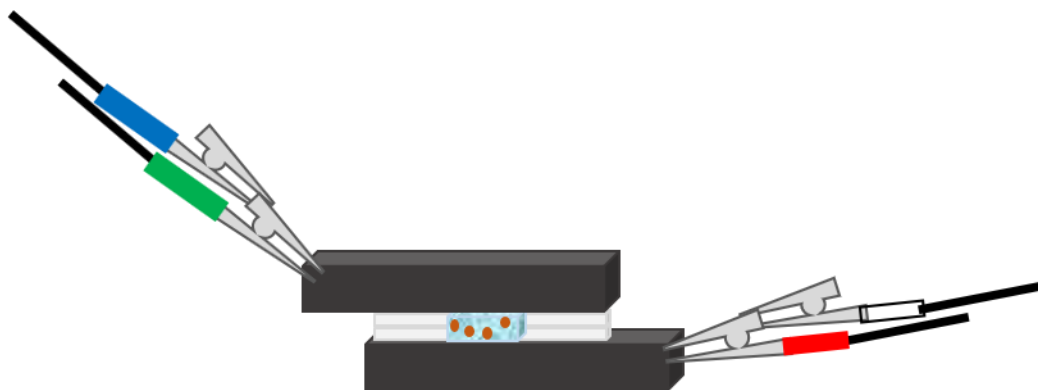
Figure 6.3: Example of hydrogel EIS cell. The hydrogel is sandwiched between graphite plates with spacers to ensure the hydrogel is not crushed. The four electrodes (blue—working sense, green—working, white—reference , red—counter) are connected and the impedance of the hydrogel is measured. The orange circles in the hydrogel represent charge carriers (i.e., analyte) within the gel network.

response outputs are measured—impedance, Z, and phase angle, θ. EIS has been applied

to systems using polymeric hydrogels as solid electrolytes[34]. A hydrogel-based EIS cell is

shown in Figure 6.3.

Any component of the electrochemical cell will affect the flow of the applied

potential, and these effects can be modeled by fitting EIS data to an equivalent electrical
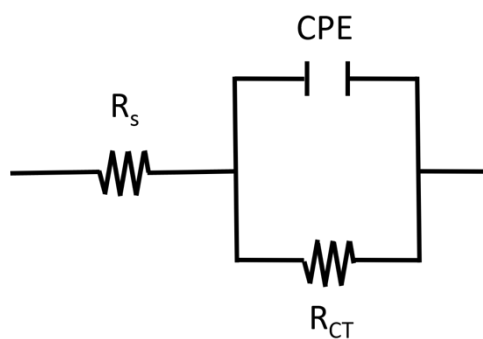
Figure 6.4: Randles equivalent circuit model. R_s models the resistance of the electrolyte, CPE models the double layer capacitance (for a "leaky" capacitor) at the electrolyte/electrode interface, and R_{CT} models the charge transfer resistance at the electrode surface.

circuit (EEC). The Randles cell[35] (shown in Figure 6.4) describes a system where a single resistor functions in series with a constant phase element (CPE) and a second resistor, which are in parallel. The first resistor models the resistive properties of the bulk material in the cell (in a hydrogel cell, the liquid phase within the hydrogel network). The CPE models the capacitive (i.e., double-layer charge alignment) properties at the electrolyte/electrode interface, while the parallel resistor models the charge transfer resistance of the analyte at the electrode surface. A CPE is often used in place of the capacitor to account for the imperfect or "leaky" capacitive properties of most materials. Changes in these properties can be used to measure the content of an analyte, such as metal ion concentration, in the bulk electrolyte (i.e., hydrogel). The most apparent changes often are in the R_s element of the circuit, as the analyte concentration changes within the bulk solution (or hydrogel network).

Thus, an active corrosion sensor is envisioned that uses the sensing capabilities of fluorescence probes, coupled with electrochemical ion detection methods. The ideal multi-analytical material would be simple, rapid, and sensitive to multiple analytes of interest.

6.5 References

1.   Scott, D. A., *Copper and Bronze in Art: Corrosion, Colorants, Conservation*. Getty Publications: 2002.

2.   Thibeau, R. J.; Brown, C. W.; Heidersbach, R. H., Raman Spectra of Possible Corrosion Products of Iron. *Appl. Spectrosc.* **1978,** *32* (6), 532-535.

3.   Oh, S. J.; Cook, D. C.; Townsend, H. E., Characterization of Iron Oxides Commonly Formed as Corrosion Products on Steel. *Hyperfine Interact.* **1998,** *112* (1), 59-66.

4.   Ma, H.; Cheng, X.; Li, G.; Chen, S.; Quan, Z.; Zhao, S.; Niu, L., The influence of hydrogen sulfide on corrosion of iron under different conditions. *Corros. Sci.* **2000,** *42* (10), 1669-1683.

5.   Lv, W.; Pan, C.; Su, W.; Wang, Z.; Liu, S.; Wang, C., Atmospheric corrosion mechanism of 316 stainless steel in simulated marine atmosphere. *Corrosion Engineering, Science and Technology* **2016,** *51* (3), 155-162.

6.   Culpan, E. A.; Foley, A. G., The detection of selective phase corrosion in cast nickel aluminium bronze by acoustic emission techniques. *Journal of Materials Science* **1982,** *17* (4), 953-964.

7.   Lenard, D. R.; Bayley, C.; Noren, B. In *Detection of selective phase corrosion of Nickel Aluminum Bronze in sea water by electrochemical frequency modulation*, Proceedings of the 2009 DOD Corrosion Conference, Washington, DC, 2009.

8.   Pan, T., Delamination of organic coating on carbon steel studied by scanning Kelvin probe force microscopy. *Surface and Interface Analysis* **2013,** *45* (6), 978-984.

9.   Williams, G.; McMurray, H. N., Inhibition of corrosion driven delamination on iron by smart-release bentonite cation-exchange pigments studied using a scanning Kelvin probe technique. *Prog. Org. Coat.* **2017,** *102, Part A*, 18-28.

10.   Atha, D. J.; Jahanshahi, M. R., Evaluation of deep learning approaches based on convolutional neural networks for corrosion detection. *Structural Health Monitoring* **2017,** *17* (5), 1110-1128.

11.   Bellezze, T.; Giuliani, G.; Viceré, A.; Roventi, G., Study of stainless steels corrosion in a strong acid mixture. Part 2: anodic selective dissolution, weight loss and electrochemical impedance spectroscopy tests. *Corros. Sci.* **2018,** *130*, 12-21.

12.   Clair, A.; Foucault, M.; Calonne, O.; Finot, E., Early-stage detection of surface stress corrosion cracking at the subgranular level. *Scripta Materialia* **2014,** *82*, 21-24.

13.   Constantinides, I.; Adriaens, A.; Adams, F., Surface characterization of artificial corrosion layers on copper alloy reference materials. *Appl. Surf. Sci.* **2002,** *189* (1–2), 90-101.

14.   Hoog, N. A.; Mayer, M. J. J.; Miedema, H.; Wagterveld, R. M.; Saakes, M.; Tuinstra, J.; Olthuis, W.; van den Berg, A., Stub resonators for online monitoring early stages of corrosion. *Sens. Actuators B* **2014,** *202*, 1117-1136.

15.   Kiosidou, E. D.; Karantonis, A.; Sakalis, G. N.; Pantelis, D. I., Electrochemical impedance spectroscopy of scribed coated steel after salt spray testing. *Corros. Sci.* **2018,** *137*, 127-150.

16.   Tan, C. H.; Shee, Y. G.; Yap, B. K.; Adikan, F. R. M., Fiber Bragg grating based sensing system: Early corrosion detection for structural health monitoring. *Sens. Actuators A* **2016,** *246*, 123-128.

17.   Liu, W.; Li, M.; Wu, N.; Liu, S.; Chen, J., A new application of Fiber optics reflection spectroscopy (FORS): Identification of "bronze disease" induced corrosion products on ancient bronzes. *Journal of Cultural Heritage* **2021,** *49*, 19-27.

18.   Khayatazad, M.; De Pue, L.; De Waele, W., Detection of corrosion on steel structures using automated image processing. *Developments in the Built Environment* **2020,** *3*, 100022.

19.   Vega, J.; Scheerer, H.; Andersohn, G.; Oechsner, M., Evaluation of the open porosity of PVD coatings through electrochemical iron detection. *Surface and Coatings Technology* **2018,** *350*, 453-461.

20.   England, A. H.; Hosbein, K. N.; Price, C. A.; Wylder, M. K.; Miller, K. S.; Clare, T. L., Assessing the Protective Quality of Wax Coatings on Bronze Sculptures Using Hydrogel Patches in Impedance Measurements. *Coatings* **2016,** *6* (4), 45.

21.   Hosbein, K. N.; England, A. H.; Price, C. A.; Clare, T. L., Measuring Sheet Resistances of Dielectrics Using Co-Planar Hydrogel Electrochemical Cells with Practical Applications to Characterize the Protective Quality of Paints on Sculptures. *Electroanalysis* **2017**, n/a-n/a.

22.   Maia, F.; Tedim, J.; Bastos, A. C.; Ferreira, M. G. S.; Zheludkevich, M. L., Active sensing coating for early detection of corrosion processes. *RCS Adv.* **2014,** *4* (34), 17780-17786.

23.   Yakoh, A.; Rattanarat, P.; Siangproh, W.; Chailapakul, O., Simple and selective paper-based colorimetric sensor for determination of chloride ion in environmental samples using label-free silver nanoprisms. *Talanta* **2018,** *178*, 134-140.

24.   Price, C. A.; Clare, T. L., Rapid quantitative spectroelectrochemical responses of hydrogel-based sensors for the in situ evaluation of corrosion inhibitors on steel. *Sens. Actuators B* **2019,** *289*, 175-181.

25.   Augustyniak, A.; Tsavalas, J.; Ming, W., Early Detection of Steel Corrosion via "Turn-On" Fluorescence in Smart Epoxy Coatings. *ACS Appl. Mater. Interfaces* **2009,** *1* (11), 2618-2623.

26.   Bozkurt, E.; Arık, M.; Onganer, Y., A novel system for Fe3+ ion detection based on fluorescence resonance energy transfer. *Sens. Actuators B* **2015,** *221*, 136-147.

27.   Cayuela, A.; Soriano, M. L.; Kennedy, S. R.; Steed, J. W.; Valcárcel, M., Fluorescent carbon quantum dot hydrogels for direct determination of silver ions. *Talanta* **2016,** *151*, 100-105.

28.   Fang, B.; Liang, Y.; Chen, F., Highly sensitive and selective determination of cupric ions by using N,N′-bis(salicylidene)-o-phenylenediamine as fluorescent chemosensor and related applications. *Talanta* **2014,** *119*, 601-605.

29.   Formica, M.; Fusi, V.; Giorgi, L.; Micheloni, M., New fluorescent chemosensors for metal ions in solution. *Coord. Chem. Rev.* **2012,** *256* (1–2), 170-192.

30.   Gu, Y.-Q.; Shen, W.-Y.; Zhou, Y.; Chen, S.-F.; Mi, Y.; Long, B.-F.; Young, D. J.; Hu, F.-L., A pyrazolopyrimidine based fluorescent probe for the detection of Cu2+ and Ni2+ and its application in living cells. *Spectrochim. Acta Part A* **2019,** *209*, 141-149.

31.   Hien, N. K.; Bao, N. C.; Ai Nhung, N. T.; Trung, N. T.; Nam, P. C.; Duong, T.; Kim, J. S.; Quang, D. T., A highly sensitive fluorescent chemosensor for simultaneous determination of Ag(I), Hg(II), and Cu(II) ions: Design, synthesis, characterization and application. *Dyes Pigm.* **2015,** *116*, 89-96.
32.   Pincher, D. W. M.; Bader, C. A.; Hayball, J. D.; Plush, S. E.; Sweetman, M. J., Graphene Quantum Dot Embedded Hydrogel for Dissolved Iron Sensing. *ChemistrySelect* **2019,** *4* (33), 9640-9646.
33.   Stern, O.; Volmer, M., Decay of Fluorescence. *Journal of the Röntgen Society* **1919,** *15* (61), 133-133.
34.   England, A. H.; Clare, T. L., Synthesis and Characterization of Flexible Hydrogel Electrodes for Electrochemical Impedance Measurements of Protective Coatings on Metal Sculptures. *Electroanalysis* **2014,** *26* (5), 1059-1067.
35.   Randles, J. E. B., Kinetics of rapid electrode reactions. *Discussions of the faraday society* **1947,** *1*, 11-19.

Chapter 7: Development of a bCQD-co-AMPS-co-PAA hydrogel towards optical and electrochemical sensing of active metal corrosion

Abstract

In situ corrosion sensing on metal objects is a challenge. Common methods require direct access to metal, are destructive, or can only detect corrosion after significant damage is done. In this work, a new corrosion sensing material is introduced. An AMPS-co-PAA hydrogel network was combined with branched polyethylenimine-functionalized carbon quantum dots to produce a flexible, non-invasive material for surface detection of metal ions, indicators of active metal corrosion. The hydrogel materials were characterized by analysis of swelling, electrochemical, and fluorescence properties. The best formulation was then used to produce calibrations against cupric and ferric ions. Finally, proof-of-concept experiments were conducted on wax-coated metal plates, demonstrating the effective ion detection for Cu^{2+}. This novel hydrogel material provides a multi-analytical tool for wide range detection of active corrosion species in the parts-per-million concentration range, allowing detection before corrosion products are visible on the metal surface.

7.1 Introduction

Given that large metal objects such as built structures and outdoor sculptures cannot be easily sampled or transported to laboratories for testing, there is a need for technology that can detect active corrosion *in situ.* This new technology should be non-destructive and measure the earliest corrosion markers directly. Active metal corrosion generates many chemical species, most notably soluble metal ions, primarily Cu^{2+} for brass and bronze and Fe^{3+} for steel and wrought iron. These ions precede the formation of stable, insoluble

species and are the earliest detectable indicators of metal corrosion. Early detection is essential to avoid devastating structural and aesthetic damage.

Direct corrosion detection methods include visual assessment, reactive coatings[1, 2], electrochemical sensors for coating porosity[3, 4], and sensors for corrosion products such as metal ions[5, 6] or counterions[7]. Metal ion sensing has been studied in solution with applications in food and water contamination. One popular direct method is the use of carbon quantum dots (CQDs) for detection of metal ions in solution *via* fluorescence quenching. Various types of CQDs have been shown to effectively sense Fe^{3+}[6, 8-11], Cu^{2+}[12-14], Ag^+[15], and Hg^{2+}[14], but these applications have only been demonstrated in solution. One interesting application is the use of carbon quantum dots (CQDs) capped with branched polyethylenimine (bPEI) as a fluorescence sensor for Cu^{2+}[13]. Literature has also shown that bPEI forms an intensely blue-colored cuprammonium complex with Cu^{2+}[16]. Harnessing the sensitivities (fluorometric and, perhaps, colorimetric) of bCQDs to metal ions for surface applications would enable detection of ionic species at the surface before visible damage has occurred.

Hydrogels are flexible polymers with a high capacity for water and ion uptake. These materials are non-reactive once polymerized and can be cleanly removed from surfaces, making them ideal for applications to metal works of art. Hydrogels are often described in terms of strength and brittleness. Strength is directly related to the entanglement of polymer strands to form a disordered but interconnected network. Brittleness is related to the number of crosslinks—a high ratio of chemical crosslinks results in a gel that is rigid but brittle. These two factors manifest as the ability of a hydrogel to uptake water. The relationships between hardness and swelling suggest that swelling

136

ratio can function as an approximation for gel rigidity. AMPS-co-PAA hydrogels, a mixed polymer of 2-acrylamido-2-methylpropane sulfonic acid (AMPS) and polyacrylic acid (PAA), were designed to balance strength and brittleness so that they can be handled easily and are pliable enough to mold to a non-planar surface, such as the surface of a sculpture[3]. These hydrogels have been used for electrochemical sensing applications[3, 4, 17] and for ion sensing on steel surfaces[5].

Polymeric hydrogel materials provide a substrate for adapting CQDs to solid-state applications. Recent studies have reported the incorporation of CQDs into various hydrogel matrices for use in Ag^+ and Fe^{3+} detection[6, 9, 15, 18]. Major drawbacks of these studies are that they were only demonstrated for analysis of solutions and the hydrogel materials are opaque or yellow to orange in color. Currently, no studies have shown Cu^{2+} sensing within a hydrogel material. These limitations leave a need for a hydrogel sensing material that is colorless and sensitive to metal ions, especially Cu^{2+}, released from solid metal alloys.

In this work, AMPS-co-PAA hydrogels were modified by adding bPEI-functionalized carbon quantum dots (bCQDs) to produce a polyampholytic hydrogel network. The hydrogels consisted of positively charged amine groups (from bCQDs) and a mixture of negatively charged sulfonate and carboxylic acid groups from AMPS and PAA, respectively. These hydrogel compositions were tailored in an effort to 1) maintain strength of the polymer network when equilibrated in neutral solvent (H_2O), 2) produce materials with high resistivity, which would enable sensitive electrochemical response to analytes of interest (Cu^{2+}, Fe^{3+}), 3) maximize bCQD fluorescence emission, and 4) optimize affinity for metal ions through metal-polymer interactions.

137

These new materials were designed to be used as *active corrosion sensors* with multiple responses to analytes of interest (Cu^{2+}, Fe^{3+}). The colorimetric, fluorometric, and electrochemical impedance properties of the bCQD-hydrogels were characterized, and their response to metal ions in solution and from metal alloy plates were evaluated to demonstrate proof-of-concept for applications to metal objects.

7.2 Experimental

7.2.1 Chemicals

Citric acid was purchased from TCI America (Hillsboro, OR). Branched-polyethylenimine, sodium chloride, potassium persulfate (KPS) and potassium (KMBS) metabisulfite were purchased from Thermo Fisher Scientific (Waltham, MA). Anhydrous iron(III) chloride, glycerol, 2-acrylamido-2-methylpropanesulfonic acid (AMPS: 50 wt% solution, sodium salt), poly(acrylic acid) (PAA: 50 wt% solution; MW 5100, sodium salt), *and* N,N'-methylenebis(acrylamide) (MBA; 1 wt%) were purchased from Sigma-Aldrich and used without further purification. Copper (II) chloride (98% purity) was purchased from Acros Organics (Morris Plains, NJ). Ethanol (200 proof) was purchased from Decon Labs (King of Prussia, PA). A mixed element standard for ICP-OES calibrations (100 μg/mL in 5% HNO_3/tr. Tartaric acid/ tr. HF) was purchased from Antylia Scientific (Vernon Hills, IL). 1-H benzotriazole (BTA) was purchased from Alfa Aesar (Haverhill, MA).

7.2.2 Synthesis of bCQDs

Branched polyethylenimine-carbon quantum dots (bCQDs) were prepared by a modification of previously reported synthesis.[19] Citric acid and branched polyethylenimine were added to a small beaker in a 3:1 mass ratio. Deionized water was added to dissolve both components (10 mL per total 2 g reagents), and the beaker was placed in an oven

preheated to 180°C. The mixture was allowed to react for 90 minutes until a viscous yellow-orange solution remained. During the reaction, the flask was checked every 15-20 minutes and warm water added as needed to prevent scorching. After 90 minutes in the oven, the product was removed and diluted in warm water. Aliquots of the solution were mixed in a 1:1 ratio with ethanol in 50 mL centrifuge tubes and centrifuged at 7500 rpm for 15 min on a Sorvall ST centrifuge (Thermo Scientific, Waltham, MA). The supernatant was removed and mixed again with ethanol, and centrifugation was repeated until a pellet no longer formed. The pellets generated from centrifugation were dissolved in deionized water and lyophilized to isolate the bCQD solid. The final product was stored in a desiccator for later use.

7.2.3 Characterization of bCQDs

As-synthesized bCQDs were analyzed to verify similarities to literature products. Absorbance spectra of bCQD solutions were collected on an Agilent 8453 UV-vis spectrophotometer with tungsten-deuterium lamp and 1024 diode array detector. Fluorescence spectra of bCQD solutions were collected on a PTI Quantamaster 800 spectrophotometer with 75W Xe-arc lamp (LPS-220B) and Model 814 photomultiplier tube detector (Horiba, Kyoto, Japan). Spectra were collected with a slit width of 1 nm using 1 s integration and 1 nm step size.

FTIR spectra were collected on a Nicolet Continuμm FTIR microscope with a Nicolet iS10 infrared spectrometer and 50 μm nitrogen cooled MCT/A detector (Thermo Fisher Scientific, Waltham, MA). Dried bCQDs were prepared for analysis by pressing the solid onto a diamond window. Data were collected in transmission mode for 128 scans

from 650 to 4000 cm^{-1} at 4 cm^{-1} spectral resolution. Omnic software (v8.3.103) was used for collection of spectra.

7.2.4 Synthesis of bCQD-hydrogels

AMPS-co-PAA hydrogels were synthesized according to a previously published method[17]. MBA was used as crosslinker with KPS and KMBS as the initiator system. Glycerol was included in the mixture as a humectant. The previously published formulation is referred to as AMPS-co-PAA in Table 7.1 and throughout the discussion.

Table 7.1: Total compositions of as synthesized bCQD-hydrogel formulations. Remainder is deionized water.

bCQD-hydrogel Formulation	% composition (m/v)					
	bCQDs	AMPS	PAA	MBA	Glycerol	KPS/KMBS
AMPS-co-PAA	0.00	18.6	11.2	0.269	11.3	0.0224
bCQD-5	5.15	18.0	7.36	0.258	11.0	0.0233
bCQD-10	10.2	10.2	5.11	0.511	2.34	0.0701
bCQD-12	11.8	11.8	5.88	0.588	1.57	0.0422
bCQD-15	15.3	13.6	6.79	0.453	2.71	0.0577

bCQD-hydrogels were prepared similarly to AMPS-co-PAA hydrogels, with varying wt% of bCQDs added to the monomer mixture before nitrogen bubbling. MBA solution was prepared at 2 wt% for the synthesis. The final weight percentages of components in each gel formula are recorded in Table 7.1. It should be noted that balancing the model copolymers with increasing bCQDs lead to challenges in synthesizing fully polymerized hydrogels. In fact, despite increases to crosslinker and initiator

concentrations, no attempted formulation greater than 15.3% bCQDs was successfully polymerized.

7.2.5 Swelling ratios were measured to assess the hydrophilicity and uptake capacities of each hydrogel formulation. As-synthesized hydrogels were rinsed for 30 minutes in deionized water to remove excess reactants, then equilibrated for 24 hours in deionized water. These fully swollen gels were cut into approximately 2×2 cm pieces, excess moisture was wicked away using a KimWipe, and the mass was recorded. These gels were then allowed to dehydrate for 24 hours in an oven set to 50 °C. Each gel sample was weighed in triplicate. The swelling was measured over five cycles. Mass swelling ratios (q_{eq}) were calculated using Equation 7.1

Equation 7.1 $$q_{eq} = \frac{(mass_{eq} - mass_{dry})}{mass_{dry}} \times 100$$

where $mass_{eq}$ is the mass of the fully hydrated gel and $mass_{dry}$ is the mass of the fully dehydrated gel.

7.2.5 Metal Solution Studies

Samples of best performing hydrogel formula, bCQD-15, were soaked for at least 14 hours in solutions of metal chloride salt (i.e., either $FeCl_3$ or $CuCl_2$). The gels were analyzed for changes in visible appearance, fluorescence spectra and resistivity measurements.

7.2.6 Metal Plate Studies

Fully water-hydrated hydrogel samples were placed on the surface of brass and steel plates coated with Renaissance Wax (Picreator Enterprises Ltd., London, UK) to

observe the metal ion uptake from a protected metal surface. These hydrogels were imaged

in situ upon placement over the metal plates, then a small volume of water (enough to cover

the surface of the gel without spilling over) was added and the gels were covered with a

layer of plastic film to ensure maintained hydration. After 15 hours, the films were

removed, and the hydrogels were imaged again. After imaging, fluorescence and EIS

measurements were collected.

7.2.7 Fluorescence Spectroscopy

A block diagram of the fluorescence measurement system is shown in Figure 7.1.

Spectra were collected using an Ocean Insight HDX spectrometer with CCD detector

coupled to a three-legged fiber optic cable with 19 randomly arranged fibers. One leg (9

fibers) was connected to a 365 nm LED light source and the other leg (10 fibers) was
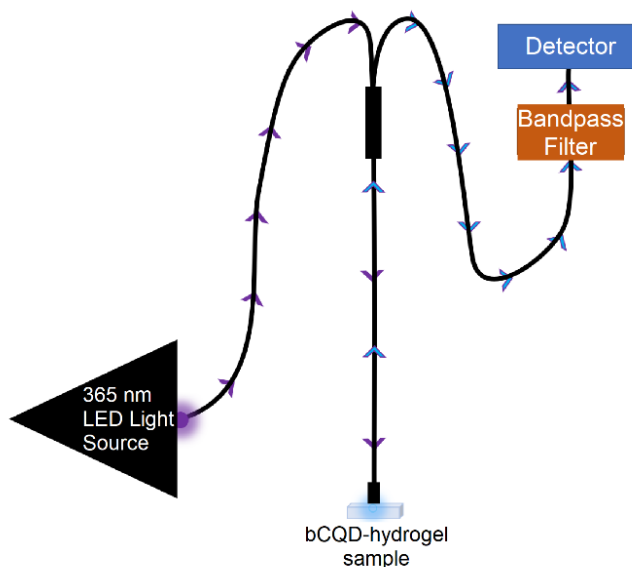
Figure 7.1: Block diagram of fluorescence spectroscopy instrument equipped with three-legged fiber optic cable, LED light source, and CCD detector. Purple arrows indicate excitation light going to the sample, blue arrows with purple outline represent emission light and excitation backscatter going to the detector.

connected to a linear variable filter with bandpass of 300-500 nm. The sample was illuminated with the joined fiber and measurements were collected in line with the excitation backscatter. All data were normalized to the excitation backscattered light. Data were processed by integrating the emission peak.

7.2.8 Electrochemical Impedance Spectroscopy (EIS)

Electrochemical impedance spectra were collected with a Gamry REF600 potentiostat over a frequency range of 1MHz to 100 mHz. The applied AC potential was 20 mV$_{rms}$ versus the open circuit potential. Measurements were performed by sandwiching hydrogels between graphite plates. A PDMS spacer was used to ensure hydrogels made full contact with the electrode while preventing breakage of the gel. Hydrogel dimensions were measured in triplicate by sandwiching between glass plates with the same spacer used for EIS measurement. Resistivity, ρ, values were calculated from Equation 7.2

Equation 7.2 $$\rho = R \times \frac{A}{l}$$

where R is the measured impedance at high frequency, A is the area and l is the thickness of the hydrogel; typical units are ohm·centimeter. The conductivity, σ, is the inverse of resistivity,

Equation 7.3 $$\sigma = \frac{1}{\rho}$$

and has units of Siemens per centimeter. Circuit fitting was performed using ZView software v3.4b (Scribner Associates, Inc, Southern Pines, NC).

7.2.9 Imaging

Images of hydrogels were collected with a Nikon D40 DSLR camera in autotimer mode with aperture of 1.6", f-stop of 4.5, ISO 200. All images were collected with matrix

143

metering, automatic white balance, and autofocus on. Two Sunlit 365 nm LED lamps and a Bulborama A85600 fluorescent black light (Las Vegas, NV) were used to achieve even UV illumination of the samples. Immediately before samples were placed for imaging, an image of the background (e.g., grid or metal plates) was collected. Images were imported into Adobe Photoshop CS4 (version11.0) and corrected by setting a common black point.

The background image was subtracted from hydrogel images and the RGB values of the subtracted images were measured in Fiji (ImageJ v1.53) software[20]. Measurements were collected as the average for the entire imaged area of the gels, in all cases greater than 10,000 individual pixels. Normalized blue values (b) were calculated by dividing the raw blue value (B) from the sum of the red, green, and blue channels (R+G+B). Raw images are provided in Appendix A: Supplementary Information.

White light images were collected on an iPhone 12 mini with automatic white balance and an Xrite color card in the image. The images were then color balanced in Photoshop by setting a white point and a black point.

7.2.11 ICP-OES

After hydrogels were soaked for solution studies, soaking solutions were analyzed by ICP-OES to determine the total metal uptake. Measurements were collected on a Perkin Elmer Optima 3000 DV equipped with an Echelle polychromator with a segmented array CCD. Iron was measured on the 239.959 nm line and copper was measured on the 213.597 nm. Both elements were calibrated from 0.01 to 1 ppm.

7.3 Results and Discussion

7.3.1 Characterization of bCQD solutions
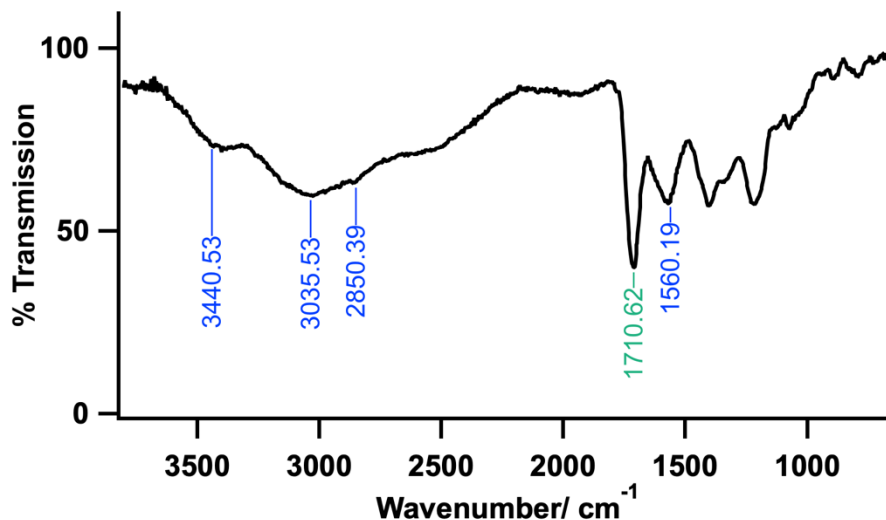
Figure 7.2: FTIR spectrum of as-synthesized bCQDs. Peaks identified in blue have been attributed to bPEI, and the peak in green indicates the Amide linkage between bPEI and the CQD core.

bCQDs were analyzed by FTIR, UV-visible absorbance, and fluorescence spectroscopies and the results compared to previously published syntheses[19, 21]. The collected FTIR spectrum is shown in Figure 7.2. The observed spectrum agreed with previously published results and showed that there was no spectral evidence of citric acid, indicating full carbonization into the graphitic CQD core. Peaks attributed to bPEI located at 3441, 3036, 2850, and 1560 cm^{-1} confirm the presence of bPEI functionalization on the surface of the CQD cores. The peak at 1711 cm^{-1} has been attributed to the amide linkage formed between bPEI and the surface of the CQD[19].

The absorbance, excitation, and emission spectra can be seen in Figure 7.3. Similar to the literature, the absorbance maximum was 362 nm, and the excitation maximum was 363 nm. The largest deviation from the literature was observed in the emission maximum,

which was 436 nm, a 44 nm blue-shift from the literature value of 460 nm[19]; the Stokes
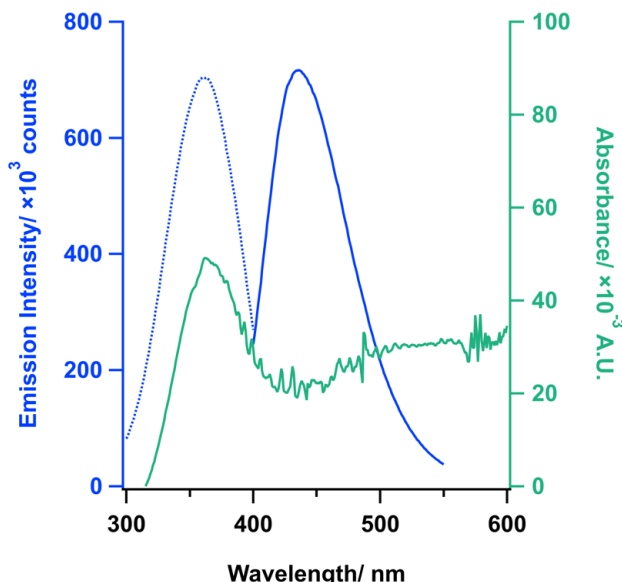
Figure 7.3: (right axis, green) Absorbance, (left axis, blue) Excitation, and Emission spectra for bCQD solution. Peak absorbance was at 362 nm, peak excitiaton was at 363 nm, and peak emission was at 436 nm.

shift was 73 nm. It has been proposed that the emission of bCQDs is largely affected by the degree of surface functionalization[19], and other amine-functionalized CQDs have reported emission at 440 nm[21]. The mole ratio of amine functional groups to citric acid in this work is 3.81:1, which falls between the two previous studies mentioned (5.71:1[19] and 1.81:1[21] mole ratios). The product reported here is comparable to previously reported synthetic products, and was expected to perform similarly in fluorescence quenching studies.

7.3.2 Characterization of bCQD-hydrogel formulations

7.3.2.1 Swelling and Resistivity

The four hydrogel formulations (bCQD-5, bCQD-10, bCQD-12, and bCQD-15) and AMPS-co-PAA underwent five cycles of swelling (i.e., fully hydrated) and deswelling

146
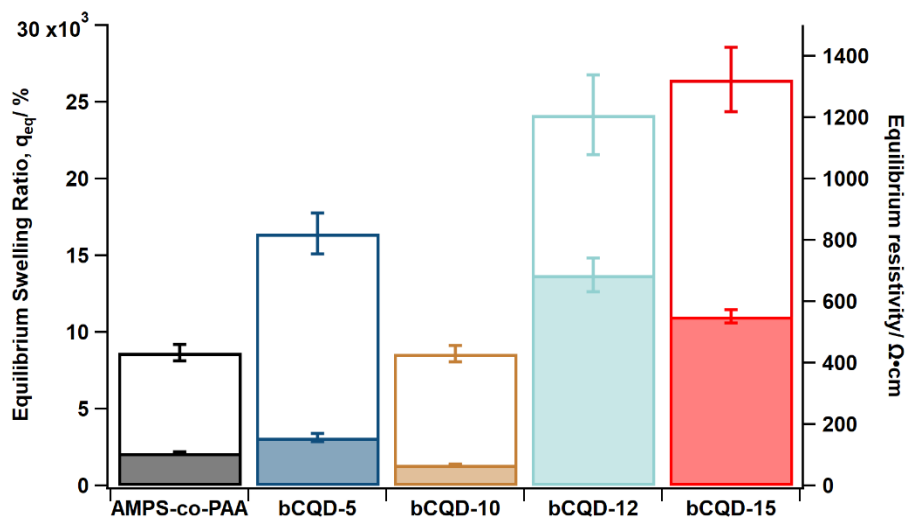
Figure 7.4: Equilibrium (white bars) swelling and (colored bars) resistivity of AMPS-co-PAA and bCQD-hydrogel formulations. Error bars represent ± one standard deviation.

(i.e., fully dehydrated) to characterize the longevity of the bCQD interactions and understand the physical properties of the gels relative to the model hydrogel.

7.3.2.2 Swelling Ratios and Resistivity

Figure 7.4 shows the q_{eq} and resistivity for each hydrogel formulation. Resistivity and q_{eq}, relative to AMPS-co-PAA, followed similar trends, generally increasing as the concentration of bCQDs increased. The AMPS-co-PAA q_{eq} was 8657 ± 529%. For bCQD-hydrogels, the q_{eq} generally increased, with the exception of bCQD-10 (8597 ± 527%), which was not significantly different from the AMPS-co-PAA gel. bCQD-5 had a q_{eq} of 16418 ± 1327%. The highest q_{eq} observed were 24164 ± 2602% and 26451 ± 2106% in bCQD-12 and bCQD-15, respectively. Significant swelling, however, affects the overall concentration of functional groups in the polymer as the network is distributed across a larger volume. The swollen compositions (wt%) are presented in Table 7.2 and

147

these values will be used hereafter as the "swollen wt%" when discussing hydrogel properties.

Table 7.2: Total compositions of bCQD-hydrogel formulations when fully swollen. Remainder is deionized water. Initiators were less than 0.001% of total mass and are not included.

bCQD-hydrogel Formulation	wt% composition				
	bCQDs	AMPS	PAA	MBA	Glycerol
AMPS-co-PAA	0.000	0.213	0.128	0.003	0.129
bCQD-5	0.031	0.109	0.045	0.002	0.067
bCQD-10	0.117	0.118	0.059	0.006	0.027
bCQD-12	0.076	0.076	0.038	0.004	0.010
bCQD-15	0.058	0.051	0.026	0.002	0.010

In early attempts at incorporating bCQDs into the hydrogel network, polymerization was inefficient. To combat this, the amount of initiator herein was scaled up in order to form more radicals and initiate more covalent crosslinks. In bCQD-10, however, the initiator was overcorrected, and a very high degree of crosslinking occurred; this produced a hydrogel that was brittle from an abundance of chemical crosslinks. When comparing the q_{eq} of bCQD-hydrogels with $\frac{wt\% \, bCQDs}{wt\% \, KPS}$, there is a linear response with a correlation constant of 0.9432 (Figure 7.5). This indicates that crosslinking is closely related to the bCQD-to-initiator ratio, rather than the initiator-to-total monomer ratio.
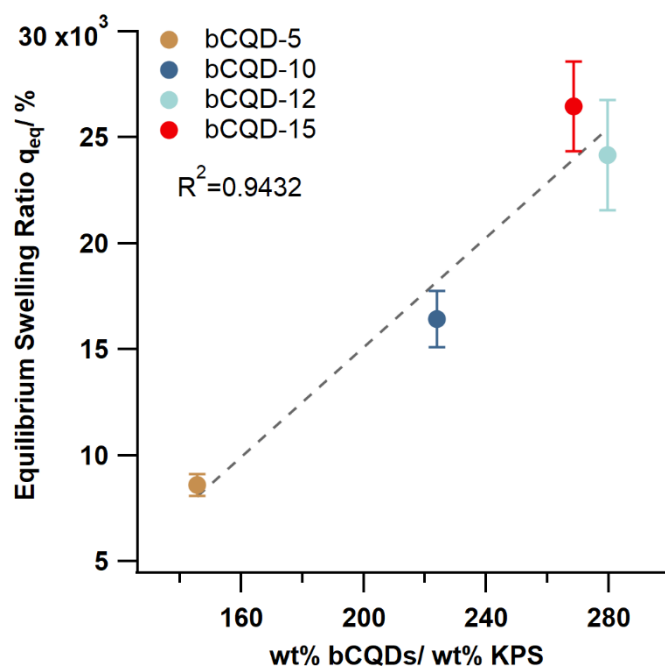
Figure 7.5: Equilibrium swelling ratio versus bCQD-to-initiator ratio. For bCQD hydrogels, a positive linear relationship is observed.

The resistivity of bCQD-10 (68.3 $\Omega\cdot$cm) was much lower than even the AMPS-co-PAA hydrogel (106.4 $\Omega\cdot$cm); this can be attributed to the low degree of swelling, and therefore higher concentration of charge carriers within the network. The resistivities of bCQD-5, bCQD-12, and bCQD-15 increased with swollen wt% of bCQDs, suggesting that charge balance from added cationic headgroups, effectively decreased the charge flow through the material.

7.3.2.2 Fluorescence Emission

bCQDs are highly water soluble, and expected to stay with the solution phase (i.e., rinse water during swelling and deswelling) unless they are covalently bound to the polymer network. After multiple cycles of swelling and deswelling, fluorescence emission remained visible in each of the hydrogels; the water baths used to swell the hydrogels
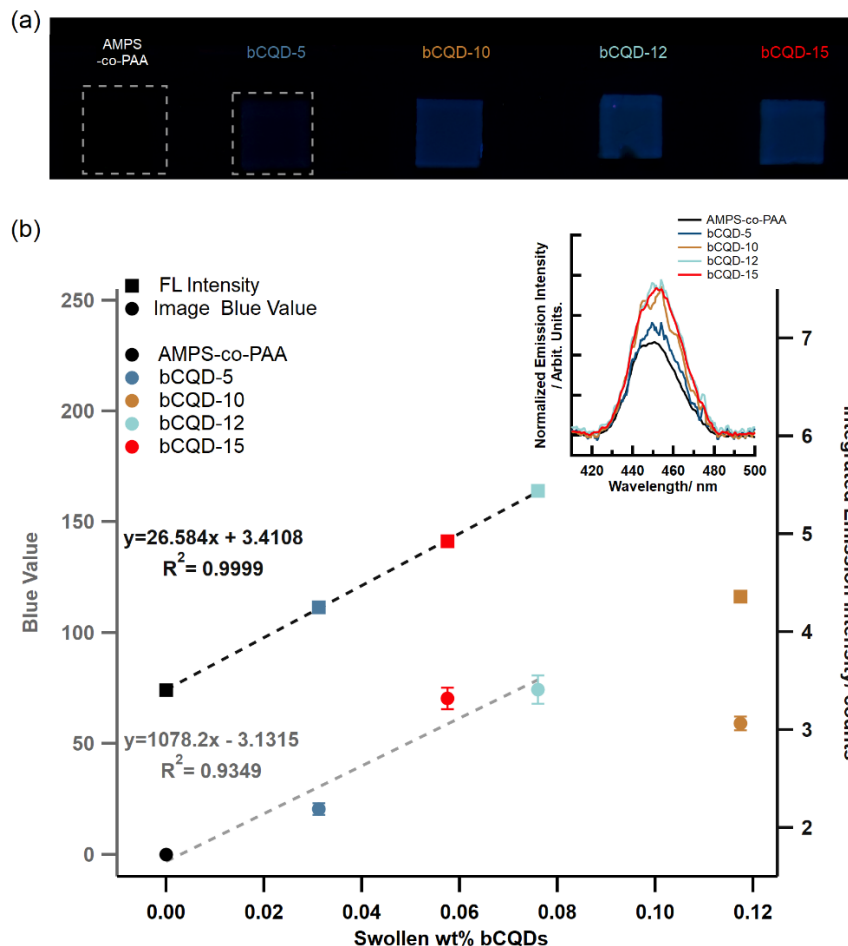
Figure 7.6: (a) Images of bCQD-hydrogels under UV illumination. Dashed boxes indicate the approximate size and location of gels not visible due to low or no fluorescence. (b) Calibrations of the blue values from the image in (a) and the integrated fluorescence intensity against the swollen wt% bCQDs. (inset) Fluorescence emission spectra of gels in (a). The color of the points in (c) correspond to the color of the labels in (a) and the spectra in the inset. The color of the dashed fit lines in (c) correlate to the appropriate vertical axis.

showed no evidence of fluorescence—indicating minimal escape from the polymer network. These observations indicate that the incorporation of bCQDs was robust enough to bind the bCQDs to the polymer network without disrupting their inherent fluorescent properties. Therefore, it is postulated that the bCQDs were successfully bound to the polymer backbone through primarily covalent linkages.

For these materials to be suitable for *in situ* measurements, the fluorescence emission must be strong—at minimum, visible to the human eye. Figure 7.6a shows an image of the hydrogel materials under UV irradiation in a dark room, normalized fluorescence spectra of each gel, and calibration of both methods against the swollen wt% of bCQDs. The image shows that the AMPS-co-PAA exhibited no visible blue fluorescence; the small peak in the inset of Figure 7.6 was an artifact of the instrumental geometry and was observed in the blank spectra.

The fluorescence intensity of the bCQD-hydrogel formulations was directly related to the swollen wt% of bCQDs in the hydrogel mixture. As shown Figure 7.6b, the intensity of fluorescence increased with bCQD concentration up to 0.08%. The most concentrated hydrogel, bCQD-10 (with 0.117 wt% bCQDs), exhibited decreased fluorescence relative to the others, suggesting that when the bCQDs are not sufficiently physically distanced through swelling, self-quenching can occur. The calibration of the imaged blue values versus bCQD concentration shows a similar trend. The sensitivity of response with small changes in bCQD concentration in Figure 7.6 shows that fiber optic fluorescence spectroscopy and imaging provide promising modes of *in situ* fluorescence measurement.

7.3.2.3 Metal Ion Uptake

After hydrogel equilibration, the residual salt solutions were measured by ICP-OES to determine to mass of metal ions taken up into the polymer networks. The results of the metal uptake measurements are shown in Figure 7.7. The results of the study show that the addition of bCQDs to the hydrogel network generally improved the metal ion uptake.
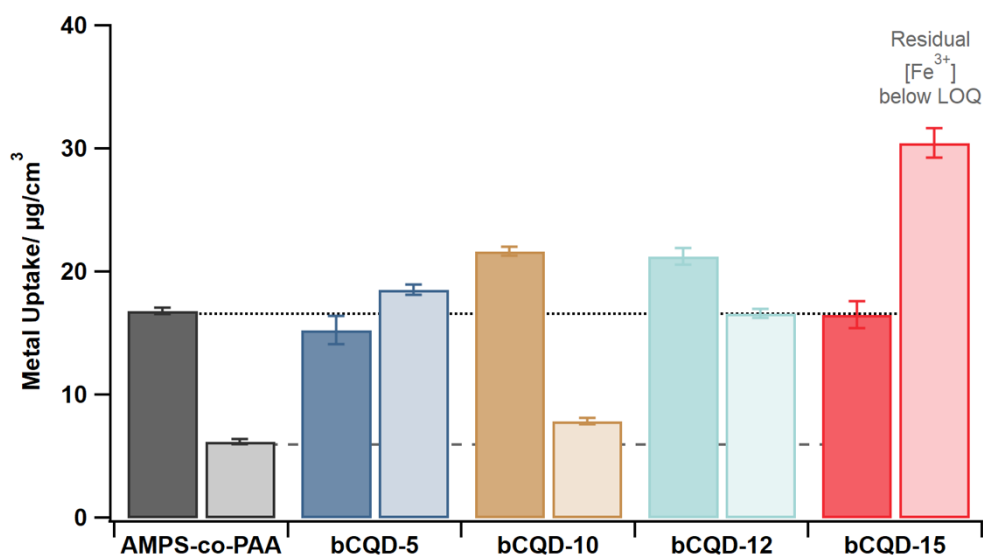
Figure 7.7: Bar plot showing metal ion uptake (dark bars-Cu2+; light bars-Fe3+) of AMPS-co-PAA and bCQD-hydrogel formulations. The dotted line indicates the level of Cu2+ uptake for the AMPS-co-PAA gel, and the dashed line indicates the Fe3+ uptake for the AMPS-co-PAA gel. Error bars represent the error propagated from triplicate measurements.

Both bCQD-10 and bCQD-12 exhibited higher Cu^{2+} uptake than AMPS-co-PAA. However, bCQD-5 took up less ion mass per gel volume than the AMPS-co-PAA gel; the uptake of bCQD-15 was not statistically different from AMPS-co-PAA. The data shown here indicate a positive correlation between the swollen wt% of bCQDs and the mass of copper taken up per volume of hydrogel. Cu^{2+} has been shown to form complexes with PEI in a 4:1 ligand-to-metal ratio[22]. The increased concentration of bCQDs provides more amine functional groups, increasing the capacity of the hydrogel to form cuprammonium complexes.

All bCQD hydrogels outperformed AMPS-co-PAA for Fe^{3+} uptake; the residual solution from bCQD-15 was below the detection limit of 12 ppb, indicating greater than

98% uptake. The improved uptake of Fe^{3+} is positively correlated with the swelling capacity of the hydrogel, but does not have a clear relationship to the bCQD content. These results suggest that the bCQDs improve the affinity of the polymer matrix to Cu^{2+} and Fe^{3+}, though these improvements likely arise from different mechanisms.

The characterization shows that swelling ratios, resistivity, and fluorescence all increased as the proportion of bCQDs was increased, except when crosslinking is extensive (i.e., bCQD-10). bCQD-12 hydrogels displayed the highest resistivity and most intense fluorescence; however, the crosslinking of this formulation was poor, rendering the gel network insufficient for handling and manipulation on a solid surface. Therefore, bCQD-15 (with the second highest resistivity and fluorescence intensity, but strong enough for handling) was determined to be the best candidate for metal response studies.

7.3.3 Response to Metal Ions

bCQD-15 hydrogels were calibrated against parts-per-million concentrations of cupric and ferric ions from salt solutions and the responses were evaluated. Subsequently, bCQD-15 hydrogels were exposed to wax-coated brass and steel plates.

7.3.3.1 Cu^{2+}

7.3.3.1.1 ICP-OES

Figure 7.8 shows the percent deswelling and percent Cu^{2+} uptake as a function of the available mass of Cu^{2+} (per volume of water-equilibrated hydrogel). The data shows that the hydrogels reached saturation when the available mass exceeded 600 μg/cm^3. At these available masses, the hydrogels deswelled by approximately 80%, limiting the physical volume for metal uptake (as evidenced by the low % ion uptake). This is likely the product of the polymer network contracting as multiple amine groups chelate the copper ions.
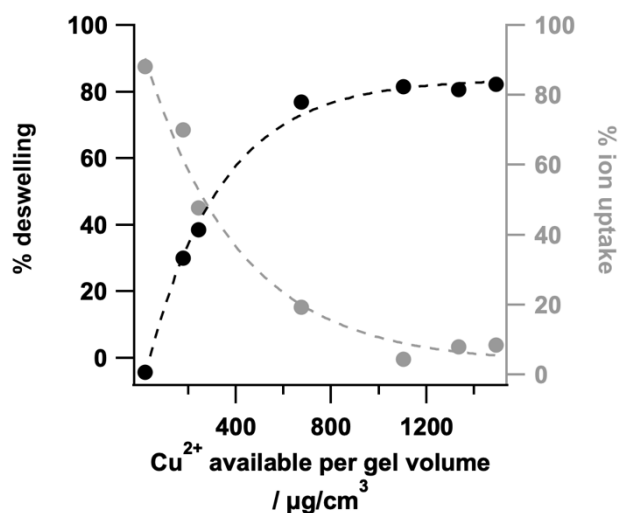
Figure 7.8: Plot of (black) percent deswelling and (gray) % ion uptake for bCQD-15 soaked in increasing amounts of Cu^{2+}. The x-axis represented the mass of copper available in the soak solution divided by the initial volume of the hydrogel piece.

7.3.3.1.2 Colorimetric response

Figure 7.9 shows images of hydrogels after soaking in metal salt solutions with concentrations of 0, 15, and 60 ppm Cu^{2+}. For the hydrogel soaked in 15 ppm Cu^{2+}, blue color formation is visible around the cut edges of the hydrogel. The hydrogel was also

observed to deswell (as indicated by the dashed box in Figure 7.9). The color formation and deswelling increased with increasing concentrations of Cu^{2+}, as evidenced by the image of a hydrogel soaked in 60 ppm Cu^{2+}. This color formation is the result of the previously mentioned cuprammonium complex[16]. Figure 7.9b shows a hydrogel after exposure to a wax-coated brass plate. The enhanced contrast shows a band of blue color formation across the middle of the hydrogel, indicating that ions were absorbed from the surface of the metal. This shows that *in situ* metal uptake into the hydrogel network is successful.
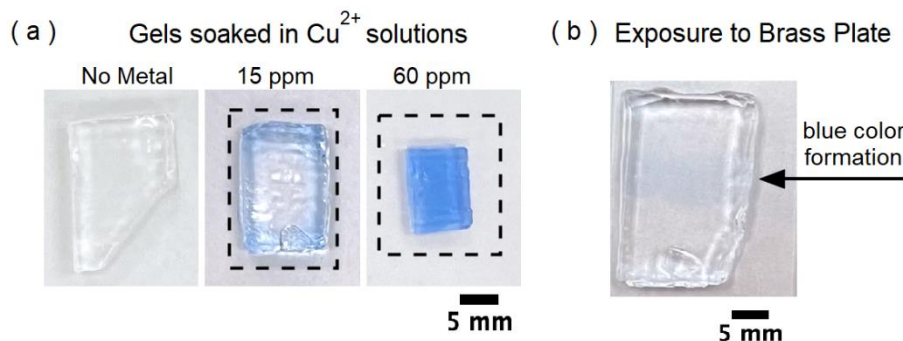
Figure 7.9: (a) Images of hydrogels soaked in increasing concentrations of Cu^{2+} solutions. Dashed boxes indicate the hydrogel size before soaking in Cu^{2+} solution.(b) Images of hydrogel after exposure to a wax-coated brass plate. The center of the hydrogel has a band of blue color formation indicating ion uptake.

7.3.3.1.3 Fluorescence response

The composite photograph in Figure 7.10a shows the fluorescence of the hydrogel pieces after soaking in the metal salt solutions. The hydrogels soaked in 1, 10, and 15 ppm Cu^{2+} solutions were still fluorescent in the center, but a visible ring of quenched fluorescence was observed around the cut edges of the gels. Despite the incomplete diffusion into the hydrogel network, the fluorescence spectroscopic measurements and
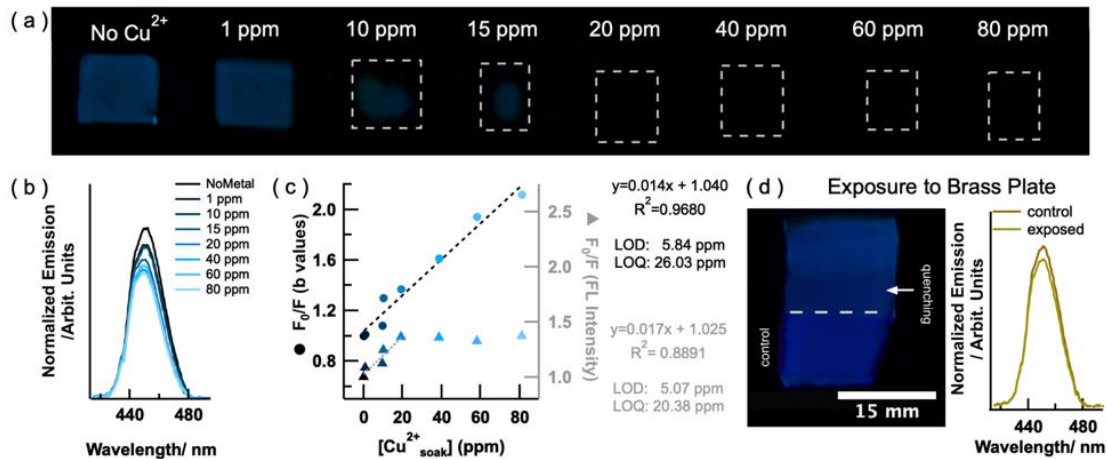
Figure 7.10: (a) Composite UV images of hydrogels soaked in increasing Cu^{2+} concentrations. (b) Fluorescence spectra for the hydrogels in (a), blue, and the gels shown in (d) brown and green. The control and exposed spectra are included, as the relevant F0/F value must be calculated using the control area of the gel as F$_0$.(c) Stern-Volmer plots for (black, circles) the normalized blue, b, values and (gray, triangles) the fluorescence spectra. (d) UV images of a hydrogel before and after exposure to a wax-coated brass plate.

image RGB analysis of the entire hydrogel area (averaging quenched and unquenched regions) showed evidence of decreased fluorescence, even at 1 ppm (Figure 7.10b). At concentrations of 20 ppm and higher, the hydrogel became fully saturated with Cu^{2+}, as evidenced by blue color formation and fully quenched fluorescence. Figure 7.10c shows the Stern-Volmer calibrations from the normalized blue values of the images (left axis) and the fluorescence spectra (right axis) Figure 7.10a. The two calibrations had similar sensitivity (0.014 and 0.017 units/ppm, respectively) and limits of detection and quantification. Notably different is the behavior of the quenching measurements beyond 20 ppm Cu^{2+}. For the normalized blue values, the trend remains linear, however the associated errors are large (greater than 100% of the average value for all points, not shown in figure for clarity). These errors were derived from the standard deviation of the R+G+B values across all measured pixels (>10,000 pixels per measurement) and the standard

deviation in the B values; in all measurements the deviation in the R+G+B values were large (because the average R and G values were much smaller than the average B values), and when the signal was low, the standard deviation in the B values was >100% of the average. For the spectroscopic measurements, the upper limit of linearity is reached at 20 ppm. Thus, each fluorescence calibration has its limitations; they do, however, provide semi-quantitative means of ion detection.

The image in Figure 7.10d shows the hydrogel from Figure 7.9b under UV illumination while still on the brass plate. The regions below the dashed line indicate an area of hydrogel placed over black vinyl tape as a control. Fluorescence spectra of the control region and the exposed region are shown Figure 7.10d. The image and the spectroscopic measurements show that the hydrogel fluorescence is quenched upon exposure to metal ions from a solid object. In this example, the quenching was detectable but not quantifiable. Nevertheless, along with the previously demonstrated color formation, bCQD-15 was demonstrated to be an effective *in situ* cupric ion sensor.

7.3.3.1.4 Conductivity

Characterization of bCQD-15 showed that the gel resistivity is high; thus, the conductivity of the gel network is low. Fitting the full impedance spectrum models the R_s value of the measurement; for clarity of the discussion, measurements are discussed in terms of conductivity. Conductivity measurements were collected for each of the hydrogel samples and are shown in Figure 7.11a. By increasing the analyte concentration, and thus the number of charge carriers within the hydrogel, the conductivity of the gel network should increase. The expected behavior was observed across the full range of Cu^{2+} soaking
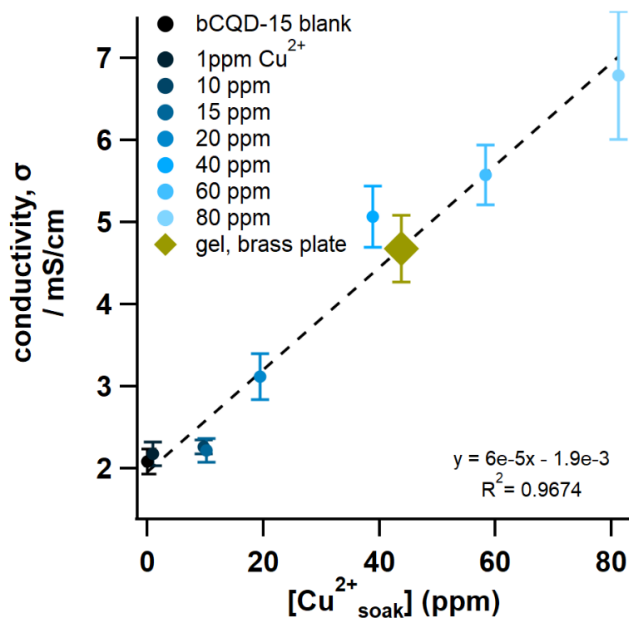
Figure 7.11: Calibration of conductivity of hydrogels versus [Cu^{2+}] *in the soaking solution*. A positive correlation is observed in the solution-soaked data. The diamond point on the fit line represents the conductivity of the hydrogel after exposure to a wax-coated brass plate. This conductivity measurement is higher than expected, given the colorimetric and fluorometric responses.

concentrations. The mechanism of this response is likely a combination of increased charge carriers (which is a well-documented response) within the hydrogel network and the observed deswelling of the hydrogels (which was shown in Section 7.3.2 to decrease resistivity). These physical and compositional responses to analyte suggest quantification of metal ions is possible from electrochemical measurements, though fully disentangling the two sources of impedance changes may be difficult, if not impossible. Despite the synergistic nature of the multiple stimuli responses, the overall impedance changes are predictable. The data herein, show an LOD of 11 ppm and LOQ of 31 ppm. The difference in dynamic range between fluorescence (up to 20 ppm) and electrochemical (31- ~80 ppm) provides an extended quantitation range for analysis of metal uptake.

The conductivity of the hydrogel after exposure to a brass plate is shown in Figure 7.11 (green diamond). The conductivity is high, indicating a significant Cu^{2+} uptake, however the blue color formation and fluorescence quenching were less sensitive to this change. This suggests further exploration is needed to confirm the quantitative nature of these analyses when applied to solid-state measurements.

7.3.3.2 Fe^{3+}

7.3.3.2.1 ICP-OES

Figure 7.12 shows the deswelling and ion uptake of hydrogels soaked in Fe^{3+} solutions. As with Cu^{2+}, bCQD-15 deswelled as the available concentration of Fe^{3+} increased. The deswelling reached saturation at approximately 800 $\mu g/cm^3$, with the maximum observed deswelling exceeding 80%. The percent uptake showed a relationship to the concentration of Fe^{3+} available, though the relationship was not as strong as observed
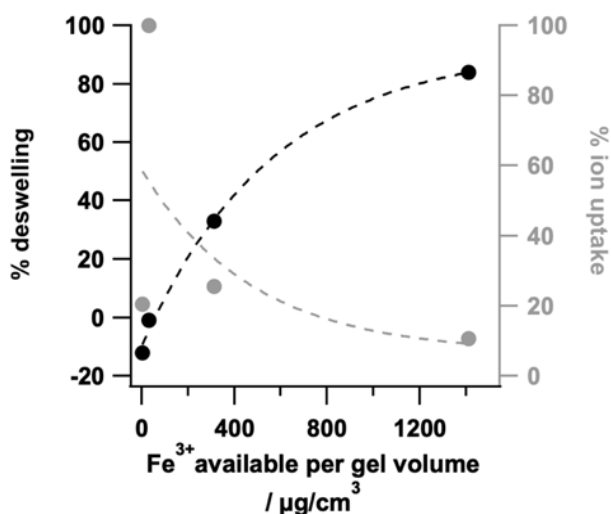

Figure 7.12: Plot of (black) percent deswelling and (gray) % ion uptake for bCQD-15 soaked in increasing amounts of Fe^{3+}. The x-axis represents the mass of iron available in the soak solution divided by the initial volume of the hydrogel.

with Cu^{2+}. The hydrogel mixture is slightly acidic before polymerization (approximately pH 5); this pH is high enough, however, for Fe^{3+} to be unstable (see Pourbaix diagram in Appendix A, Figure 7.20).

7.3.3.2.2 Colorimetric response

Figure 7.13a shows images of hydrogels after soaking in Fe^{3+} solutions. In 10 ppm Fe^{3+}, a slight yellow color developed. In 50 ppm Fe^{3+}, the hydrogel significantly deswelled and became orange throughout. Figure 7.13 also shows that the deswelling was less uniform than the analogous copper hydrogel, as the center of the hydrogel is bulging. Because of the conditions of the hydrogel, the color formation is possibly the result precipiation, rather than complex formation. Figure 7.13b shows an image of a hydrogel after exposure to a steel plate. No color formation is visible, indicating minimal ion uptake.
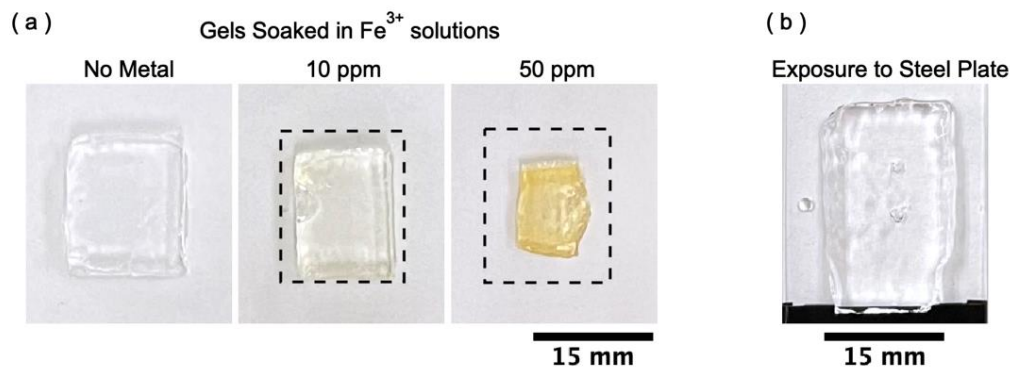

Figure 7.13: (a) Visible light images of hydrogels soaked in Fe^{3+} solutions of increasing concentration. Dashed boxes indicate the size of hydrogels before soaking in salt solution. (b) Image of a hydrogel after exposure to a wax-coated steel plate.
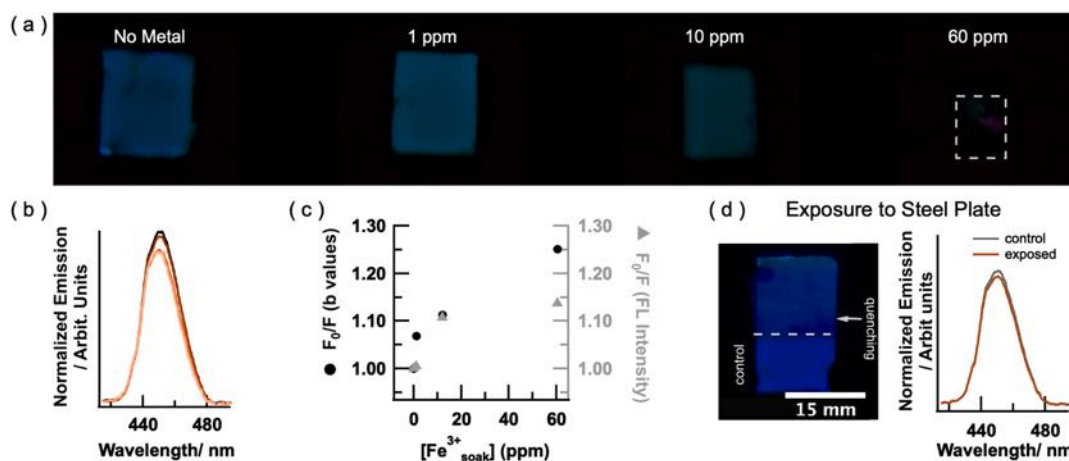
Figure 7.14: (a) Composite UV images of hydrogels soaked in increasing Fe^{3+} concentrations. (b) Fluorescence spectra for the hydrogels in (a), orange, and the gels shown in (d) gray and brown. The control and exposed spectra are included, as the relevant F_0/F value must be calculated using the control area of the gel as F_0.(c) Stern-Volmer plots for (black, circles) the normalized blue, b, values and (gray, triangles) the fluorescence spectra. (d) UV images of the hydrogel after exposure to a wax-coated steel plate.

7.3.3.2.3 Fluorescence response

Figure 7.14a shows UV-illuminated images of hydrogels soaked in increasing concentrations of Fe^{3+}. While the fluorescence is visibly decreased in the 10 and 60 ppm gels, the quenching is not as distinct as in the hydrogels soaked in equivalent concentrations of Cu^{2+}. Figure 7.14b shows the fluorescence spectra of the four hydrogels in Figure 7.14a. The spectra indicate some decrease in fluorescence, though like the visible quenching, it is not as significant as with Cu^{2+}. Calibration of both the UV images and the fluorescence spectra are shown Figure 7.14c. From these calibrations, it is apparent that Fe^{3+} does induce quenching in the hydrogels, however this effect is less sensitive and has a narrower dynamic range than Cu^{2+}.

161

The image and fluorescence spectra in Figure 7.14d reveal that after exposure to a wax-coated steel plate, hydrogels can be quenched. The calibration results combined with the steel plate study indicate that the uptake and/or quenching mechanism of Fe^{3+} is less effective than that of Cu^{2+}. This could be the result of instability of Fe^{3+} at environmental pH (i.e., 5-8). Additionally, Fe^{3+} uptake is likely dominated by the presence of available sulfonate groups in the hydrogel network, rather than complex formation with the bCQD amine moieties. The addition of bCQDs required a decrease in both AMPS and PAA, relative to the AMPS-co-PAA model polymer. Thus, fewer functional groups are present, decreasing the polymer's affinity to Fe^{3+}.

7.3.3.2.4 Conductivity

Figure 7.15a shows the calibration of conductivity measurements for hydrogels soaked in Fe^{3+} solutions. The electrochemical response for Fe^{3+} was more sensitive than for Cu^{2+}, as indicated by the slope of the best fit line. The LOD (7 ppm) and LOQ (29 ppm) were comparable to the copper calibration. Complexes formed between metal ions and the amine moieties on the bCQDs would immobilize the ions within the polymer matrix, lessening the effect of increasing charge carrier concentration. Thus, the contrast in electrochemical response of bCQD-15 to Cu^{2+} and Fe^{3+} provides evidence that the hydrogel-ion interactions; while Cu^{2+} forms a well-documented metal-bCQD complex, Fe^{3+} likely participates in primarily collisional interactions with bCQDs.

The conductivity of the hydrogel exposed to a wax-coated steel plate is not shown in Figure 7.15a, as the conductivity measurement was below the LOD of the calibration.

The results of Fe^{3+} response studies suggest that while some iron ions migrate into the hydrogel, the overall fluorometric response is low compared to Cu^{2+}. The conductivity measurements, however, suggest that with precise sample preparation, the hydrogels could be calibrated against $[Fe^{3+}]$.
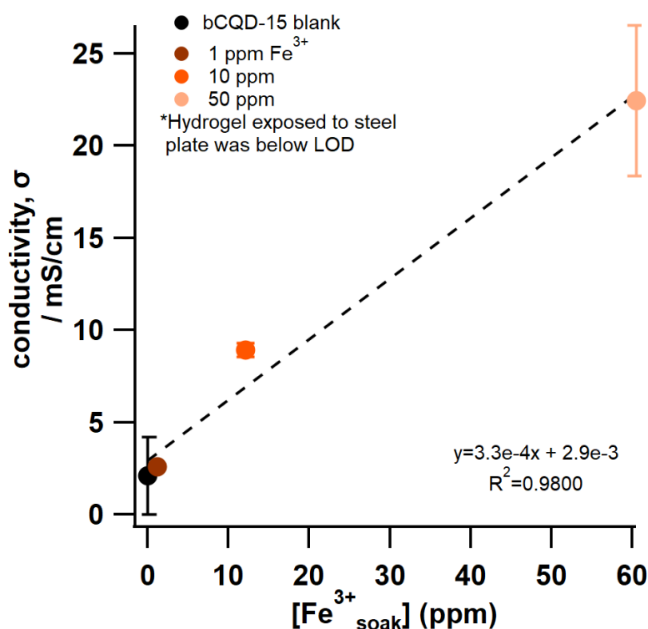
Figure 7.15: Calibration of conductivity of hydrogels versus $[Fe^{3+}]$ *in the soaking solution*. A positive correlation is observed in the solution-soaked data. The conductivity of the hydrogel after exposure to a wax-coated steel plate fell below the calculated LOD for the calibration and is not shown.

7.4 Conclusions

The work presented herein introduces a new sensing material for the detection of corrosion products on metal objects. This is the first report of a bCQD-equipped flexible hydrogel sensor used for solid-state applications. This material was designed as a multi-analytical sensor, showing both fluorescence and electrochemical response to stimuli, presenting advantages over other studies. Additionally, the fluorescence quenching is significant enough to be detectable by UV-illuminated imaging.

163

These results show sensitivity to both Cu^{2+} and Fe^{3+}, the active corrosion species generated in brass/bronze and steel corrosion, respectively. Imaging can provide a rapid identification of active corrosion, although associated errors may be large due to limited dynamic range. Spectroscopic measurements can provide more quantitative results when the fluorescence is not fully quenched. The multi-analytical response and sensitivity to multiple relevant ion species suggest the applications of this material to *in situ* corrosion monitoring would be an inexpensive, robust solution to a longstanding problem. Alternatively, the same material can be used in multiple contexts, allowing for applications when only one or two of the three presented techniques is available.

Future directions of this work may include examining the selectivity for other ubiquitous and metallic ionic species, both cations (e.g., Na^+, K^+, Ca^{+2}, Mg^{+2}, Zn^{+2}, Sn^{+2}, Al^{+3}) and anions (e.g., Cl^-, SO_4^{-2}, PO_4^{-2}). All measurements and calibrations presented herein are compared against the concentration of the solution the hydrogels were soaked in, not the actual concentration of the metal ions in the hydrogel. The ICP-OES data presented in Section 5.3.2.5 provides some instrumental validation of the metal ion uptake, however more replicate data is needed to validate the calibration of the fluorescence and EIS responses against the concentration of metals taken up by the hydrogels. These further experiments would provide necessary expansions of this work to a fully quantitative detection method. With accurate quantitation, case studies testing the material *in situ* on outdoor metal structures would be possible.

7.5 References

1.   Augustyniak, A.; Tsavalas, J.; Ming, W., Early Detection of Steel Corrosion via "Turn-On" Fluorescence in Smart Epoxy Coatings. *ACS Appl. Mater. Interfaces* **2009,** *1* (11), 2618-2623.

2.   Maia, F.; Tedim, J.; Bastos, A. C.; Ferreira, M. G. S.; Zheludkevich, M. L., Active sensing coating for early detection of corrosion processes. *RCS Adv.* **2014,** *4* (34), 17780-17786.

3.   England, A. H.; Hosbein, K. N.; Price, C. A.; Wylder, M. K.; Miller, K. S.; Clare, T. L., Assessing the Protective Quality of Wax Coatings on Bronze Sculptures Using Hydrogel Patches in Impedance Measurements. *Coatings* **2016,** *6* (4), 45.

4.   Hosbein, K. N.; England, A. H.; Price, C. A.; Clare, T. L., Measuring Sheet Resistances of Dielectrics Using Co-Planar Hydrogel Electrochemical Cells with Practical Applications to Characterize the Protective Quality of Paints on Sculptures. *Electroanalysis* **2017**, n/a-n/a.

5.   Price, C. A.; Clare, T. L., Rapid quantitative spectroelectrochemical responses of hydrogel-based sensors for the in situ evaluation of corrosion inhibitors on steel. *Sens. Actuators B* **2019,** *289*, 175-181.

6.   Liu, Z.; Jia, R.; Chen, F.; Yan, G.; Tian, W.; Zhang, J.; Zhang, J., Electrochemical process of early-stage corrosion detection based on N-doped carbon dots with superior Fe3+ responsiveness. *Journal of Colloid and Interface Science* **2022,** *606*, 567-576.

7.   Yakoh, A.; Rattanarat, P.; Siangproh, W.; Chailapakul, O., Simple and selective paper-based colorimetric sensor for determination of chloride ion in environmental samples using label-free silver nanoprisms. *Talanta* **2018,** *178*, 134-140.

8.   Chandra, S.; Laha, D.; Pramanik, A.; Ray Chowdhuri, A.; Karmakar, P.; Sahu, S. K., Synthesis of highly fluorescent nitrogen and phosphorus doped carbon dots for the detection of Fe3+ ions in cancer cells. *Luminescence* **2016,** *31* (1), 81-87.

9.   Cheng, C.; Xing, M.; Wu, Q., Green synthesis of fluorescent carbon dots/hydrogel nanocomposite with stable Fe3+ sensing capability. *J. Alloys Compd.* **2019,** *790*, 221-227.

10.   Zhang, C.; Cui, Y.; Song, L.; Liu, X.; Hu, Z., Microwave assisted one-pot synthesis of graphene quantum dots as highly sensitive fluorescent probes for detection of iron ions and pH value. *Talanta* **2016,** *150*, 54-60.

11.   Zhou, M.; Guo, J.; Yang, C., Ratiometric fluorescence sensor for Fe3+ ions detection based on quantum dot-doped hydrogel optical fiber. *Sens. Actuators B* **2018,** *264*, 52-58.

12.   Baruah, U.; Chowdhury, D., Functionalized graphene oxide quantum dot–PVA hydrogel: a colorimetric sensor for Fe2+, Co2+ and Cu2+ ions. *Nanotechnology* **2016,** *27* (14), 145501.

13.   Dong, Y.; Wang, R.; Li, G.; Chen, C.; Chi, Y.; Chen, G., Polyamine-Functionalized Carbon Quantum Dots as Fluorescent Probes for Selective and Sensitive Detection of Copper Ions. *Anal. Chem.* **2012,** *84* (14), 6220-6224.

14.   Li, C.; Liu, W.; Ren, Y.; Sun, X.; Pan, W.; Wang, J., The selectivity of the carboxylate groups terminated carbon dots switched by buffer solutions for the detection of multi-metal ions. *Sens. Actuators B* **2017,** *240*, 941-948.

15.   Cayuela, A.; Soriano, M. L.; Kennedy, S. R.; Steed, J. W.; Valcárcel, M., Fluorescent carbon quantum dot hydrogels for direct determination of silver ions. *Talanta* **2016,** *151*, 100-105.

16.   Shao, H.; Ding, Y.; Hong, X.; Liu, Y., Ultra-facile and rapid colorimetric detection of Cu2+ with branched polyethylenimine in 100% aqueous solution. *Analyst* **2018,** *143* (2), 409-414.

17.   England, A. H.; Clare, T. L., Synthesis and Characterization of Flexible Hydrogel Electrodes for Electrochemical Impedance Measurements of Protective Coatings on Metal Sculptures. *Electroanalysis* **2014,** *26* (5), 1059-1067.

18.   Guo, J.; Zhou, M.; Yang, C., Fluorescent hydrogel waveguide for on-site detection of heavy metal ions. *Sci. Rep.* **2017,** *7*, 7902.

19.   Dong, Y.; Wang, R.; Li, H.; Shao, J.; Chi, Y.; Lin, X.; Chen, G., Polyamine-functionalized carbon quantum dots for chemical sensing. *Carbon* **2012,** *50* (8), 2810-2815.

20.   Schindelin, J.; Arganda-Carreras, I.; Frise, E.; Kaynig, V.; Longair, M.; Pietzsch, T.; Preibisch, S.; Rueden, C.; Saalfeld, S.; Schmid, B.; Tinevez, J. Y.; White, D. J.; Hartenstein, V.; Eliceiri, K.; Tomancak, P.; Cardona, A., Fiji: an open-source platform for biological-image analysis. *Nat Methods* **2012,** *9* (7), 676-82.

21.   Schneider, J.; Reckmeier, C. J.; Xiong, Y.; Von Seckendorff, M.; Susha, A. S.; Kasák, P.; Rogach, A. L., Molecular Fluorescence in Citric Acid-Based Carbon Dots. *J. Phys. Chem. C* **2017,** *121* (3), 2014-2022.

22.   Moreno-Villoslada, I.; González, F.; Jofré, M.; Chandía, P.; Hess, S.; Rivas, B. L., Complexation Behavior of Cu2+ in the Presence of Iminodiacetic Acid and Poly(ethyleneimine). *Macromolecular Chemistry and Physics* **2005,** *206* (15), 1541-1548.

Figure 7.16: Image of hydrogels after soaking in metal salt solutions. The grid is not moved between images, so that a complete background subtraction can be executed.

Figure 7.17: Background grid for imaging gels soaked in metal salt solutions.
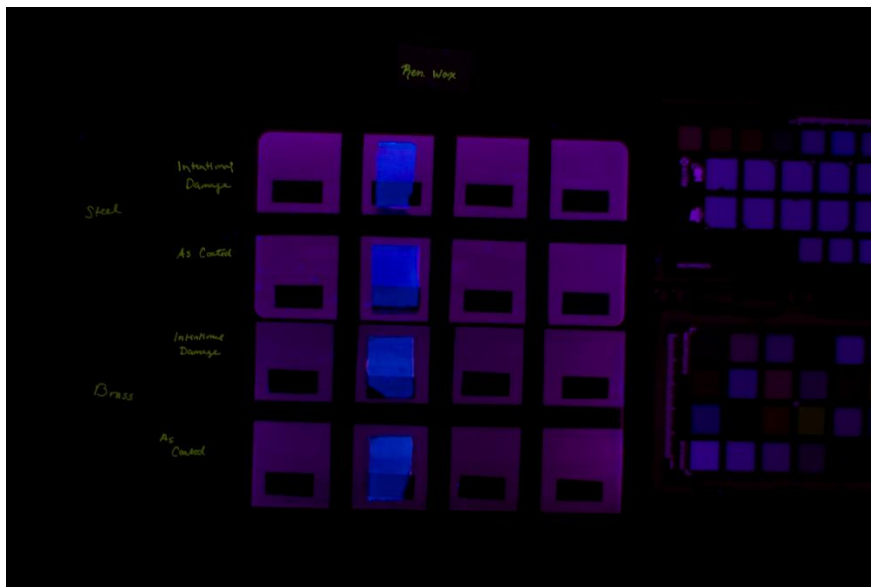
Figure 7.18: Image of (top) steel and (bottom) brass plates with hydrogel in place after 14 hours of exposure.
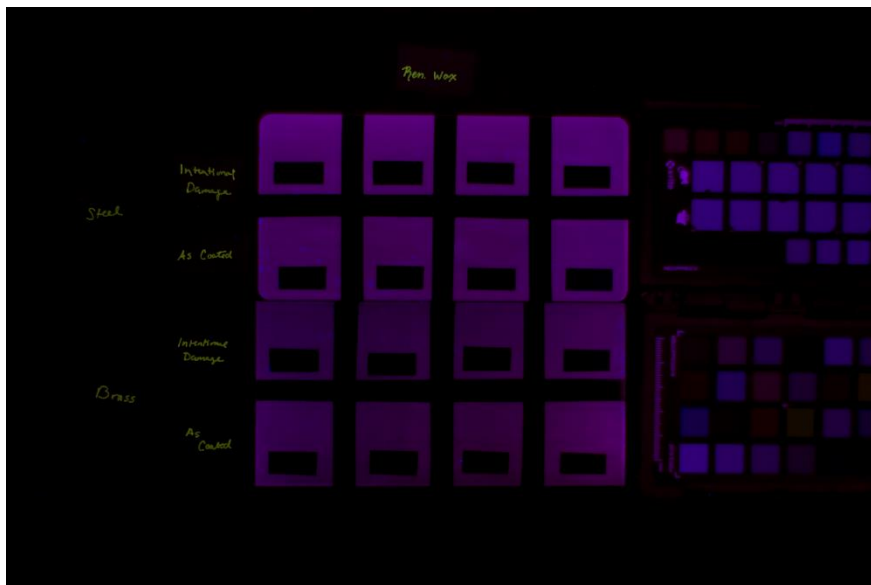

Figure 7.19: Raw image of (top) steel and (bottom) brass plates before hydrogel exposure. This image was used as background for subtraction after gel quenching.
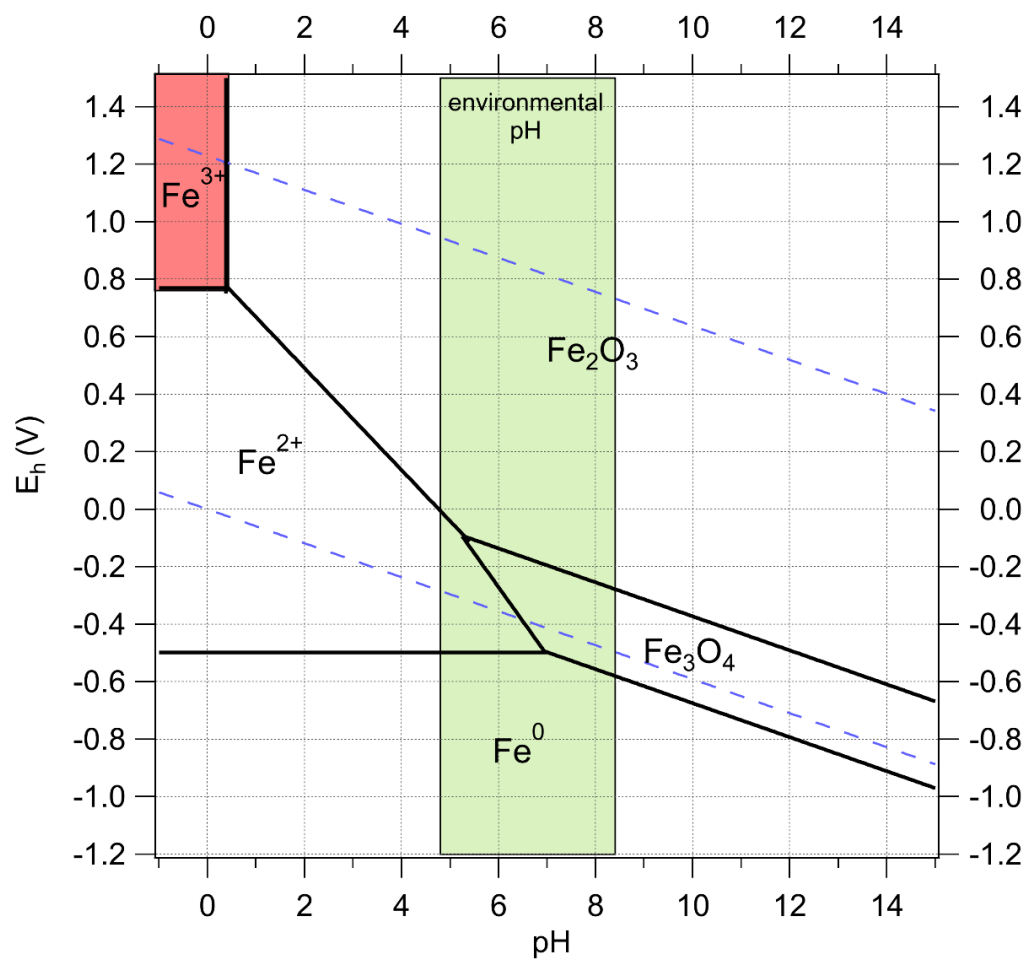
Figure 7.20: Pourbaix diagram for common iron corrosion species. The green region represents environmental pH range and the red region indicates the pH range where Fe^{3+} is the primary iron species. The area between the blue dashed lines represents the stability region of water.

Chapter 8: Conclusions and Final Remarks
The works presented herein illustrate analytical applications of chemistry in the context of cultural heritage conservation. This dissertation is a demonstration of conservation science for the improved understanding of objects and their production, as well as improved analytical techniques, materials, and methods for better conservation science.

In Chapters 3, a novel technique for micro-sampling was introduced, and the effects of the method were evaluated. This work provided a robust data analysis methodology, using chemometric methods to build a tangible spectral solution for unknown colorant mixtures. These developments will provide the conservation community with new avenues for minimally invasive analysis, an essential consideration for cultural heritage objects.

Chapter 4 presented optimization the synthetic methods for producing AgNPs for use in SERS and fully characterized reference colorants to build a robust library. These characterizations are presented in an effort to inform the conservation community and allow for greater transparency in scientific methods. I hope that the work I've detailed allows other conservation scientists to pick up projects more quickly and efficiently so that the body of knowledge may continue to grow and flourish.

In Chapter 5, the micro-sampling technique and genetic algorithm method were used, along with visual analysis, XRF, and FTIR spectroscopy to evaluate the substrate and red colorants used on a collection of 18th century woodblock prints attributed to Suzuki Harunobu. This colorant study resulted in identification of five red chromophores used in one, two, and three-component mixtures to produces a wide range of red-, pink- and orange-colored areas. These results inform the conservation community on the red palette

in use in late 18th century Edo. These data may also be combined with studies performed at other institutions to build a more comprehensive timeline of colorant usage in Japan.

Chapter 7 saw a pivot from materials analysis to materials development. The bCQD hydrogel sensors designed for detection of active corrosion show the strength of framing scientific inquiry in the context of conservation. While other quantum dot-hydrogel materials have been demonstrated for analysis of aqueous systems, the functional hydrogels presented herein are the first material of their kind designed with the intended application of analysis on solid objects. While this new material shows promise, initial experimentation showed that even with precise preparation of the polymer network, variability in the final product can result due to the random nature of radical polymerization. For this reason, a thorough calibration would be required for each analytical experiment. In addition, repeated syntheses of the same formulation should be prepared and characterized to identify the variability in material properties batch-to-batch.

Future experiments should aim to develop a quantitative workflow through close examination of the metal uptake and resultant analyte concentration *within the hydrogel network*. Additionally, determination of the metal species within the hydrogel (i.e. metal complexes vs. free ions) would better inform investigators as to the exact sensing mechanisms and would aid in translating a solution-state calibration to solid-state application for quantitative results. Demonstrative case studies using the hydrogels should be conducted to introduce this material as a corrosion sensor for the conservation community. With execution of these characterization and demonstrative experiments, a rapid and non-destructive sensing material for corrosion detection could be implemented in institutions to analyze metal objects, mitigating the long-term damage of corrosion.